

SEARCH FOR  $t\bar{t}Z' \rightarrow t\bar{t}t\bar{t}$  PRODUCTION IN THE MULTILEPTON FINAL STATE IN  
 $pp$  COLLISIONS AT  $\sqrt{s} = 13$  TEV WITH THE ATLAS DETECTOR

By

Hieu Le

A DISSERTATION

Submitted to  
Michigan State University  
in partial fulfillment of the requirements  
for the degree of

Physics — Doctor of Philosophy

2025

## ABSTRACT

This dissertation presents a search for a new beyond-the-Standard-Model (BSM) particle at the Large Hadron Collider (LHC). Many BSM models predict a new heavy vector boson ( $Z'$ ) that couples primarily to the top quark in both production and decay (top-philic). The search is performed in multilepton events consistent with four-top-quark ( $t\bar{t}t\bar{t}$ ) production, due to the distinctive signature of the multilepton final states and the its robustness against common background processes at the LHC. Analysis data was collected by the ATLAS detector from 2015 to 2018, using proton-proton collisions at the LHC at a center-of-mass energy of 13 TeV. No statistically significant deviation from Standard Model predictions is observed. Exclusion limits are set on the production cross section of the targeted top-philic particle in the mass range between 1 TeV and 3 TeV.

## ACKNOWLEDGMENTS

First and foremost, I am deeply grateful for my dissertation advisor and P.I, Professor Reinhard Schwienhorst, for his support, guidance and tolerance as part of my role in ATLAS and my doctoral program at Michigan State. Reinhard is the primary driving force in many exciting opportunities that I've had the chance to experience, and he also provides much-appreciated support both in knowledge and wisdom in times of need. I am incredibly thankful that Reinhard is one of the people that plays a part in who I am today.

I would like to express sincere gratitude to one of our postdocs in the MSU ATLAS group, Binbin Dong, who I closely worked with within ATLAS. Binbin is a massive source of support for physics, technical and ATLAS-specific knowledge that played a pivotal role during my training with ATLAS, during the analysis in this dissertation, and during my time at CERN. I would have never been able to find my way through without her help.

I am also extremely thankful for the MSU ATLAS group, in particular Professors Wade Fisher and Daniel Hayden, for their guidance and feedback on my professional and personal endeavors which helped immensely in my development both scientifically and socially. I thank Rongqian Qian and Jason Gombas, my fellow advisees that offered great ideas, knowledge and friendship. I would like to thank Julia Hinds, Stergios Kazakos and Pratik Kafle for their support and companionship during my time at CERN. I also thank former and present members of our group that I've had the pleasure to work with: Joey Huston, Jos Gabriel Reyes Rivera, Cecilia Imthurn, Xinfei Huang, Ahmed Tarek, Kyle Fielman, Robert Les and Trisha Farooque. It was a wonderful experience being part of the MSU ATLAS group and I hope our group continues to grow, even if it makes scheduling weekly meetings for everyone that much harder.

I would like to express my gratitude to my dissertation committee members, Professors Reinhard Schwienhorst, Johannes Pollanen, Wade Fisher, Remco Zegers and Yuying Xie, for their guidance, patience and commitment to my growth and success as a researcher and a person.

It has been a pleasure to work with the many outstanding people in ATLAS, especially the BSM multi-top analysis team. I would like to thank Philipp Gadow, Krisztian Peters, Frédéric Déliot and Neelam Kumari for their dedication and commitment to fostering a successful and fruitful collaboration. I also thank Meng-Ju Tsai, Hui-Chi Lin, Thomas Nommensen, Jianming Qian, Quake Qin, Tomke Schröer, Xilin Wang, Helena Gomez and Daniela Paredes for their tireless efforts in the analysis. I am truly glad to have had the chance to work with all of you.

Special thanks to my fellow graduate students that I have had the chance to befriend during my doctoral journey: Daniel Lay, Grayson Perez, Jordan Purcell, Eric Flynn, Isabella Molina, Mo Hassan, Cavan Maher and Hannah Berg. You all taught me a lot more than I could ever imagine and helped me more than I could ever asked for, and I look forward to see where we go from here.

Finally, I would like to thank my family, to whom this dissertation is dedicated: my spouse Allen Sechrist, for encouraging me tirelessly everyday and always being there for me even when I can't be there for myself; my cat Eddie, for being the best cat anyone could ask for; my brother Hien Le, my dad Bac Le, and my mom Thuy Cao, for their endless love and support. Thank you for being the reason that I am where I am today.

## TABLE OF CONTENTS

<b>List of Tables . . . . .</b>	<b>vii</b>
<b>List of Figures . . . . .</b>	<b>ix</b>
<b>KEY TO ABBREVIATIONS . . . . .</b>	<b>xii</b>
<b>Chapter 1. Introduction . . . . .</b>	<b>1</b>
<b>Chapter 2. Theoretical Overview . . . . .</b>	<b>5</b>
2.1 The Standard Model . . . . .	5
2.1.1 Elementary particles . . . . .	5
2.1.2 Mathematical formalism . . . . .	9
2.1.2.1 Quantum chromodynamics . . . . .	10
2.1.2.2 Electroweak theory . . . . .	11
2.1.2.3 Higgs mechanism . . . . .	14
2.2 Beyond the Standard Model: $t\bar{t}Z' \rightarrow t\bar{t}t\bar{t}$ . . . . .	17
2.2.1 Top-philic vector resonance . . . . .	17
2.2.2 Production channels . . . . .	19
2.2.3 Decay modes . . . . .	20
<b>Chapter 3. LHC &amp; ATLAS Experiment . . . . .</b>	<b>22</b>
3.1 The Large Hadron Collider . . . . .	22
3.1.1 Overview . . . . .	22
3.1.2 LHC operations . . . . .	24
3.1.3 Physics at the LHC . . . . .	25
3.2 The ATLAS detector . . . . .	25
3.2.1 Inner detector . . . . .	28
3.2.2 Calorimeter systems . . . . .	29
3.2.3 Muon spectrometer . . . . .	31
3.2.4 Trigger & data acquisition . . . . .	33
<b>Chapter 4. Particle Reconstruction &amp; Identification . . . . .</b>	<b>34</b>
4.1 Primary reconstruction . . . . .	34
4.1.1 Tracks . . . . .	34
4.1.2 Vertices . . . . .	35
4.1.3 Topological clusters . . . . .	36
4.2 Jets . . . . .	37
4.2.1 Jet reconstruction . . . . .	38
4.2.2 Flavor tagging . . . . .	39
4.3 Leptons . . . . .	43
4.3.1 Electrons . . . . .	43
4.3.2 Muons . . . . .	46

4.4	Missing transverse momentum . . . . .	48
4.5	Overlap removal . . . . .	49
4.6	Object definition . . . . .	50
<b>Chapter 5. Data &amp; Simulated Samples</b>	. . . . .	<b>51</b>
5.1	Data samples . . . . .	51
5.2	Monte Carlo samples . . . . .	51
5.2.1	$t\bar{t}Z'$ signal samples . . . . .	52
5.2.2	Background samples . . . . .	54
<b>Chapter 6. Analysis Strategy</b>	. . . . .	<b>59</b>
6.1	Event selection . . . . .	59
6.1.1	Event categorization . . . . .	60
6.2	Analysis regions . . . . .	61
6.2.1	Signal regions . . . . .	63
6.2.2	Control regions . . . . .	64
6.3	Background estimation . . . . .	67
6.3.1	Template fitting for fake/non-prompt estimation . . . . .	68
6.3.2	Charge misidentification data-driven estimation . . . . .	69
6.3.3	$t\bar{t}W$ background data-driven estimation . . . . .	71
<b>Chapter 7. Systematic Uncertainties</b>	. . . . .	<b>74</b>
7.1	Experimental uncertainties . . . . .	74
7.1.1	Luminosity & pile-up reweighting . . . . .	74
7.1.2	Leptons . . . . .	74
7.1.3	Jets . . . . .	75
7.1.4	Missing transverse energy . . . . .	77
7.2	Modeling uncertainties . . . . .	78
7.2.1	Signal and irreducible background uncertainties . . . . .	78
7.2.2	Reducible background uncertainties . . . . .	80
<b>Chapter 8. Results</b>	. . . . .	<b>82</b>
8.1	Statistical interpretation . . . . .	82
8.1.1	Profile likelihood fit . . . . .	82
8.1.2	Exclusion limit . . . . .	85
8.2	Fit results . . . . .	87
<b>Chapter 9. Summary</b>	. . . . .	<b>97</b>
<b>References</b>	. . . . .	<b>98</b>

# List of Tables

Table 4.1: Overlap removal process for this analysis, applied sequentially from top to bottom. . . . .	49
Table 4.2: Summary of object selection criteria used in this analysis. $\ell_0$ refers to the leading lepton in the event. . . . .	50
Table 5.1: Summary of all HLT triggers used in this analysis. Events are required to pass at least one trigger. . . . .	52
Table 5.2: Summary of all Monte-Carlo samples used in this analysis. $V$ refers to an EW ( $W^\pm/Z/\gamma^*$ ) or Higgs boson. Matrix element (ME) order refers to the order in QCD of the perturbative calculation. Tune refers to the underlying-event tune of the parton shower (PS) generator. . . . .	53
Table 6.1: Definitions of signal, control and validation regions (VR) used in this analysis. $N_{\text{jets}}$ and $N_b$ refers to the number of jets and number of $b$ -tagged jets respectively. $\ell_1$ refers to the leading lepton, $\ell_2$ refers to the subleading lepton and so on. $H_T$ refers to the $p_T$ scalar sum of all leptons and jets in the event. $m_{\ell\ell}$ refers to the dilepton invariant mass, which must not coincide with the $Z$ -boson mass range of 81-101 GeV for SS2L+3L events. . . . .	62
Table 6.2: Definitions of SR sub-regions. Events are sorted into different sub-regions based on the number of $b$ -tagged jets and leptons present. . . . .	63
Table 6.3: List of possible assigned values for DFCAA. . . . .	67
Table 8.1: Normalization factors for backgrounds with dedicated CRs, obtained from a simultaneous fit in all CRs and SR under the background-only hypothesis. The nominal pre-fit value is 1 for all NFs and 0 for the scaling factors $a_0$ and $a_1$ . Uncertainties shown include both statistical and systematic uncertainties.	89

Table 8.2: Pre-fit and post-fit background yields in the inclusive SR. The number of data events and pre-fit estimate signal yields are also shown. Background yields shown are obtained using the $t\bar{t}Z'$ signal sample with $m_{Z'} = 2$ TeV. Total yield uncertainty differs from the quadrature sum of constituent uncertainties due to (anti-)correlation effects. . . . .	94
--	----

Table 8.3: Post-fit impact of uncertainty sources on the signal strength $\mu$ , grouped by categories. Values shown are obtained from the fit using the $t\bar{t}Z'$ signal sample with $m_{Z'} = 2$ TeV. Impact on $\mu$ is evaluated for each uncertainty category by re-fitting with the corresponding set of NPs fixed to their best-fit values. Total uncertainty differs from the quadrature sum of constituent uncertainties due to correlation between NPs in the fit. . . . .	95
---	----

# List of Figures

Figure 2.1: Particles within the SM and their properties. . . . .	6
Figure 2.2: Feynman diagram for $t\bar{t}$ production and subsequent decay processes. Top quark decays into a $W$ -boson and $b$ -quarks, and $W$ -boson can decay to a $q\bar{q}$ or a $\ell\nu_\ell$ pair. . . . .	8
Figure 2.3: Illustration of a common representation of the Higgs potential. Before SSB, the ground state $\phi(0)$ is located at A which is symmetric with respect to the potential. A perturbation to this state fixes the ground state energy $ \phi(0) ^2$ to a particular value at B, "spontaneously" breaking the symmetry and degeneracy in $ \phi(0) ^2$ . . . . .	15
Figure 2.4: Feynman diagrams for tree level $Z'$ production in association with (a) $t\bar{t}$ , (b) $tj$ (light quark) and (c) $tW$ , decaying to final states containing (a) $t\bar{t}t\bar{t}$ or (b)(c) $t\bar{t}t$ . . . . .	19
Figure 2.5: Theoretical $t\bar{t}Z'$ production cross-section times $Z' \rightarrow t\bar{t}$ branching ratio as a function of the $Z'$ mass at LO in QCD coupling to top with $c_t = 1$ under a simplified top-philic model. . . . .	20
Figure 2.6: Branching ratios for $t\bar{t}t\bar{t}$ decay. The same-sign dilepton and multilepton channels together forms the SSML channel. . . . .	21
Figure 3.1: The full CERN accelerator complex as of 2022. . . . .	23
Figure 3.2: Current and future timeline of LHC operations as of 2025 with corresponding center-of-mass energies and projected integrated luminosities. . .	24
Figure 3.3: Summary of predicted and measured cross-section for SM processes at the LHC at different center-of-mass energies . . . . .	26
Figure 3.4: A cross section slice of the ATLAS detector showing different subsystems along with visualization of different types of particles traveling through the detector . . . . .	27

Figure 3.5: Cutaway illustration of the inner detector along with its subsystems. . . . .	28
Figure 3.6: Cutaway illustration of the calorimeter system including the EM, hadronic and LAr forward calorimeters . . . . .	30
Figure 4.1: Stages of topo-cluster formation corresponding to each threshold. In (a), proto-clusters are seeded from cells with adequate signal significance $\zeta_{\text{cell}}^{\text{EM}}$ . The clusters are further merged and split in (b) according to a predefined cluster growth threshold. The process stops in (c) when all sufficiently significant signal hits have been matched to a cluster. . . . .	37
Figure 4.2: Jet energy scale calibration sequence for EM-scale jets. . . . .	39
Figure 4.3: Overview of the GN2 architecture. The number of jet and track features are represented by $n_{\text{jf}}$ and $n_{\text{tf}}$ respectively. The global jet representation and track embeddings output by the Transformer encoder are used as inputs for three task-specific networks. . . . .	41
Figure 4.4: The $c$ -, light- and $\tau$ -jet rejection rate as a function of $b$ -tagging efficiency for GN2 and DL1d using (a) jets in the $t\bar{t}$ sample, and (b) jets in the $Z'$ sample. The performance ratios of GN2 to DL1d are shown in the bottom panels. . . . .	42
Figure 6.1: Post-fit background composition in each analysis region and sub-region. The fit was performed using ideal pseudo-datasets (Asimov data) in the SR. . . . .	61
Figure 6.2: Pre-fit kinematic distributions and event compositions in the inclusive SR for (a) $H_T$ i.e. scalar sum of $p_T$ of all objects in the event, (b) jet multiplicity, (c) $b$ -jet multiplicity, (d) leading lepton $p_T$ . The shaded band represents the uncertainty in the total distribution. The first and last bins of each distribution contains underflow and overflow events respectively. . . . .	65
Figure 6.3: Feynman diagram for one possible $t\bar{t}W$ decay process with similar SS2L lepton signature to the $t\bar{t}Z'$ signal. Usually only two $b$ -jets are present due to CKM suppression of $b$ -quark production from $W$ -boson decays; this is enough to allow $t\bar{t}W$ decays to enter and contaminate the SR. . . . .	66
Figure 6.4: Charge flip rate calculated for SR and CR $t\bar{t}W$ in bins of $ \eta $ and $p_T$ . . . . .	71
Figure 7.1: Combined QmisID uncertainty rate for SR in bins of $ \eta $ and $p_T$ . . . . .	81

Figure 8.1: Example of an exclusion limit graph. The solid (dotted) line represents the observed (expected) upper limits as a function of the  $Z'$  mass at 95% CL on the cross-section of  $pp \rightarrow t\bar{t}Z'$  production times the  $Z' \rightarrow t\bar{t}$  branching ratio. The solid blue line represents the theoretical signal cross-section with  $c_t = 1$  at LO in QCD [74]. The green and yellow bands represent the 68% ( $\pm 1\sigma$ ) and 95% ( $\pm 2\sigma$ ) confidence intervals for the expected upper limits. Cross section of  $t\bar{t}Z'$  within the region above the observed limit is excluded under the current model. Masses below the  $m_{Z'}$  value at which the observed limit intersect the theoretical cross section are excluded. . . . .

86

Figure 8.2: Comparison between data and post-fit prediction for the discriminant observable in each CR. Distributions shown are obtained from the fit using the  $t\bar{t}Z'$  signal sample with  $m_{Z'} = 2$  TeV. The lower panel shows the ratio between data and post-fit predictions. The shaded band represents the total uncertainty on the fit. The dashed line represents the pre-fit distribution. . . . .

90

Figure 8.4: Post-fit pull from nominal values for nuisance parameters representing systematic uncertainties. Systematics pruned during the fit are not shown. The dashed line represents the nominal pre-fit values. The green and yellow bands represent the 68% ( $\pm 1\sigma$ ) and 95% ( $\pm 2\sigma$ ) confidence intervals for the nominal fit value. . . . .

93

Figure 8.5: Observed (solid line) and expected (dotted line) upper limits as a function of the  $Z'$  mass at 95% CL on the cross-section of  $pp \rightarrow t\bar{t}Z'$  production times the  $Z' \rightarrow t\bar{t}$  branching ratio. The region above the observed limit is excluded. The solid blue line represents the theoretical signal cross-section with  $c_t = 1$  at LO in QCD. The green and yellow bands represent the 68% ( $\pm \sigma$ ) and 95% ( $\pm 2\sigma$ ) confidence intervals respectively. . . . .

96

## KEY TO ABBREVIATIONS

### Physical & Mathematical Quantities

$\chi^2$  chi-squared

$d_0$  transverse impact parameter

$\Delta R$  angular distance

$\sqrt{s}$  center-of-mass energy

$\eta$  pseudorapidity

$E_T$  transverse energy

$E_T^{\text{miss}}$  missing transverse energy

$\Gamma$  decay width

$\gamma_5$  chirality projection operator

$\gamma_\mu$  Dirac matrices

$H_0$  null hypothesis

$H_T$  scalar sum of transverse momenta  $p_T$  of all objects in an event

$\mathcal{L}$  Lagrangian

$\mathcal{L}(\theta)$  likelihood function

$L$  instantaneous luminosity

$m_{\ell\ell}$  dilepton invariant mass

$\mu$  signal strength

$\mu_F$  factorization scale

$\mu_R$  renormalization scale

$N_{\text{jets}}$  number of jets/jet multiplicity

$\mathcal{O}(n)$  on the order of  $n$

$\mathcal{P}$  Poisson probability

$p_T$  transverse momentum

$Q$  electric charge

$q_\mu$  profile likelihood ratio

$\sigma$  standard deviation

$\sigma[b]$  cross-section

$z_0$  longitudinal impact parameter

## Particles & Processes

$\gamma^*$  virtual photon

$gg$  gluon-gluon fusion

$pp$  proton-proton

PbPb lead-lead

$q$  quark

$q\bar{q}$  quark-antiquark pair

$t\bar{t}$  top/anti-top quark pair

$t\bar{t}X$  top pair in association with another particle

$t\bar{t}t\bar{t}$  four-top-quark

$V$  massive vector bosons ( $W^\pm, Z$ )

$H$  Higgs in association with a vector boson

## Acronyms

**1LOS** one lepton, or two leptons of opposite charges

**2HDM** two-Higgs doublet model

**AF3** AtlFast3 fast simulation

**ALICE** A Large Ion Collider Experiment

**ATLAS** A Toroidal LHC ApparatuS

**AWAKE** Advanced WAKEfield Experiment

**BDT** boosted decision tree

**BR** branching ratio

- BSM** Beyond the Standard Model
- CB** combined muon
- CERN** European Organization for Nuclear Research
- CKM** Cabibbo-Kobayashi-Maskawa matrix
- CL** confidence level
- CMS** Compact Muon Solenoid
- CP** charge-parity symmetry
- CR** control region
- CSC** Cathode Strip Chambers
- CTP** Central Trigger Processor
- ECIDS** Electron Charge ID Selector
- EFT** effective field theory
- EM** electromagnetic
- EW** electroweak
- FASER** ForwArd Search ExpeRiment
- FCal** forward calorimeter
- FS** full detector simulation
- GNN** graph neural network
- GRL** Good Run List
- GSC** Global Sequential Calibration
- GSF** Gaussian-sum filter
- GUT** Grand Unified Theory
- HEC** hadronic endcap calorimeter
- HF** heavy-flavor
- HL-LHC** High-Luminosity Large Hadron Collider
- HLT** High-Level Trigger
- ID** Inner Detector

**IP** interaction point

**JER** jet energy resolution

**JES** jet energy scale

**JVT** Jet Vertex Tagger

**KATRIN** Karlsruhe Tritium Neutrino Experiment

**L1** Level 1

**LAr** liquid argon

**LF** light-flavor

**LH** likelihood

**LHC** Large Hadron Collider

**LHCb** Large Hadron Collider beauty

**LINAC** linear accelerator

**LLH** log-likelihood

**LO** leading order

**MC** Monte Carlo simulation

**ME** matrix element

**ML** multilepton

**MS** Muon Spectrometer

**MDT** Monitored Drift Tubes

**MET** missing transverse energy

**NF** normalization factor

**NNJvt** Neural Network-based Jet Vertex Tagger

**NLO** next-to-leading order

**NNLO** next-to-next-to-leading order

**NP** nuisance parameter

**OP** operating point (also working point)

**OS** opposite-sign

**PCBT** pseudo-continuous  $b$ -tagging  
**PDF** parton distribution function  
**POI** parameter of interest  
**PS** parton shower  
**PV** primary vertex  
**QCD** quantum chromodynamics  
**QED** quantum electrodynamics  
**QFT** quantum field theory  
**QmisID** charge mis-identification  
**RPC** Resistive Plate Chamber  
**SCT** Semiconductor Tracker  
**SF** scale factor  
**SM** Standard Model  
**SR** signal region  
**SS** same-sign  
**SSB** spontaneous symmetry breaking  
**SS2L** same-sign dilepton  
**SSML** same-sign dilepton, or more than two leptons of any charges  
**TDAQ** Trigger and Data Acquisition  
**TGC** Thin-Gap Chamber  
**TRT** Transition Radiation Tracker  
**VEV** vacuum expectation value  
**VR** validation region  
**UE** underlying-event

# Chapter 1. Introduction

The 20<sup>th</sup> century ushered in a revolutionary period for mankind's understanding of the fundamental nature of matter and the forces that govern our universe with the development of special relativity and quantum mechanics, which redefined our understanding of space, time, energy and matter at the furthest extremes of scale from the vast reaches of the cosmos to the tiniest constituents of matter. Building on these principles, Quantum Electrodynamics (QED) [1–3] was developed as the first successful quantum field theory (QFT) describing electromagnetism. The discovery of beta decay [4] and its paradoxical behaviors within the framework of QED prompted the prediction of neutrinos and development of the theory of weak interaction.

At around the same time, a spectrum of strongly interacting particles was discovered [5] as particle accelerators probed deeper into atomic nuclei, leading to the formation of the quark model in the 1960s and with it a hypothesized new binding force, the strong force. However, the QFT framework remained incapable of describing the weak and strong interactions until advancements in gauge theory and the quantization of non-Abelian gauge via QFT resulted in the formation of Yang-Mills theory [6, 7]. This sparked a renaissance in modern physics with the unification of electromagnetism and weak force in 1967 under the framework of electroweak (EW) [8] theory, as well as the development of Quantum Chromodynamics (QCD) [9, 10] to describe the strong force binding quarks.

At this point, the prediction of massless bosons within EW formalism remained a contradiction to the predicted massive  $W^\pm$  and  $Z$  bosons that mediate the weak force. This was resolved by the introduction of EW spontaneous symmetry breaking and the Higgs mechanism in 1964 [11–13], which explained the generation of masses for both the EW bosons

and fermions. Together, these developments culminated in the Standard Model of particle physics SM [14], a comprehensive theory that described the electromagnetic, weak, and strong interactions, classified all known fundamental particles and predicted mathematically consistent but not yet observed particles. Following its inception, particles predicted by the Standard Model were gradually observed experimentally, starting with the gluon in 1979 [15], then the  $W^\pm$  and  $Z$  bosons [16, 17], and finally the top quark in 1995 [18, 19]. The final missing piece was confirmed as the Higgs boson was observed in 2012 independently by the ATLAS [20] and CMS [21] detectors at the Large Hadron Collider, completing the Standard Model after a 40-year search and cementing it as the most successful framework so far describing fundamental constituents of matter and their governing forces.

Despite its successes, the Standard Model remains incomplete. Key unanswered questions include the nature of dark matter [22], which makes up about 27% of the universe's energy content but has no explanation within the Standard Model; the origin of neutrino masses and their oscillations [23]; the observed matter-antimatter asymmetry in the universe; possible unification of the EW and strong interaction into a Grand Unified Theory (GUT); and the hierarchy problem describing the large discrepancy in scales between forces and the apparent lightness of the Higgs boson compared to values predicted from quantum corrections.

After the discovery of the Higgs boson, efforts have been underway to construct new hypotheses and models in search of beyond the Standard Model (BSM) physics via different avenues, one of which being direct searches at colliders for new resonances or particles not predicted by the SM. In particular, the top quark possesses large mass and strong coupling to the Higgs boson [24] which gives it a special role in many proposed BSM models as a possible connection with strong coupling to new particles and heavy resonances. In addition, the top quark has a clean decay signature with well-understood final states and is produced in

abundance at the LHC from  $pp$  collisions in the form of top pairs  $t\bar{t}$  [25, 26]. This dissertation presents a search for the production of a heavy resonance that couples preferentially to top quark (topophilic) in association with a top pair ( $t\bar{t}$ ) in the final state with either two leptons of the same electric charge or at least three leptons (SSML). The search is performed in proton-proton collisions at  $\sqrt{s} = 13$  TeV with the ATLAS detector [27] via the four-top ( $t\bar{t}t\bar{t}$ ) production channel.

A similar search for topophilic heavy resonances was performed using the  $t\bar{t}t\bar{t}$  final state containing either one lepton or two opposite-sign leptons (1LOS) [28] with a much larger branching ratio of 56% and larger irreducible background of SM processes. Despite the small cross-section within the SM, the  $t\bar{t}t\bar{t}$  SSML final state provides heightened sensitivity to BSM physics and higher signal-to-background ratio than inclusive resonance searches (e.g. in dijet or dilepton final states) due to the distinctive signal signature and suppression of large SM background processes present in  $t\bar{t}$ -associated production i.e. diboson ( $VV$ ),  $t\bar{t}$  production with an additional boson ( $t\bar{t}V/ttH+jets$ ) or with additional light leptons from heavy-flavor decays ( $t\bar{t} + HF$ ). The cross-section for  $t\bar{t}t\bar{t}$  production can be enhanced by many proposed BSM models including supersymmetric gluino pair-production [29, 30], scalar gluon pair-production [31, 32], top-quark-compositeness models [33, 34], effective field theory (EFT) operators [26, 35–38] and two-Higgs-doublet models (2HDM) [39–43]. Searching within this channel is particularly motivated by the recent observed excess in the measurement of four-top production in the SSML final state at the LHC by the ATLAS detector [44] with a measured cross-section of  $24^{+7}_{-6}$  fb, almost double the SM prediction of  $13.4^{+1.0}_{-1.8}$  fb.

A simplified color-singlet vector boson model [45] is employed for the search to minimize parameter dependency on model choice. Data-driven background estimation methods are implemented for  $t\bar{t}W$ - one of the dominant irreducible backgrounds in the analysis - and

the charge misidentification background to rectify mismodeling related to jet multiplicity in simulated background that were not covered in the previous 1LOS  $t\bar{t}Z'$  search [28] and SSML  $t\bar{t}H/A \rightarrow t\bar{t}t\bar{t}$  search [46]. These methods are employed similarly to that in previous SM  $t\bar{t}t\bar{t}$  analyses [44, 47].

This dissertation is organized as follows. Chapter 2 presents the formalism of the SM and relevant BSM concepts. Chapter 3 provides an introduction to the LHC and ATLAS detector. Chapter 4 describes the reconstruction and identification of physics object from detector signals. Chapter 5 defines the data and simulated samples used in the analysis. Chapter 6 describes the analysis strategy, including object definition, analysis region description and background estimation methods. Chapter 7 summarizes the uncertainties involved in the analysis. Chapter 8 presents the statistical interpretation and analysis results. Finally, Chapter 9 discusses a summary of the analysis and future outlook.

# Chapter 2. Theoretical Overview

## 2.1 The Standard Model

The Standard Model of Physics (SM) [48] is currently the most successful formalism to describe the physical world at a microscopic scale by providing descriptions for all currently known elementary particles, along with three out of four fundamental forces (electromagnetism, weak force, strong force) with the exception of gravity. The SM is however not perfect, and there remain unanswered questions that require development and discovery of new physics beyond the Standard Model (BSM). This chapter describes an overview of important components within the SM and relevant BSM aspects for this analysis.

### 2.1.1 Elementary particles

Elementary particles in the SM can be classified into two groups: bosons consisting of particles following Bose-Einstein statistics with integer spin, and fermions consisting of particles following Fermi-Dirac statistics with half-integer spin. Fermions are the building blocks of composite particles and consequently all known matter, and can be further classified into quarks & leptons. Bosons act as force mediators for all fundamental forces described by the SM, and can either be a scalar boson with spin 0 or vector gauge bosons with spin 1. For each elementary particle, there also exists a corresponding antiparticle with identical mass and opposite charge (electric or color). Figure 2.1 shows all known elementary particles in the SM.

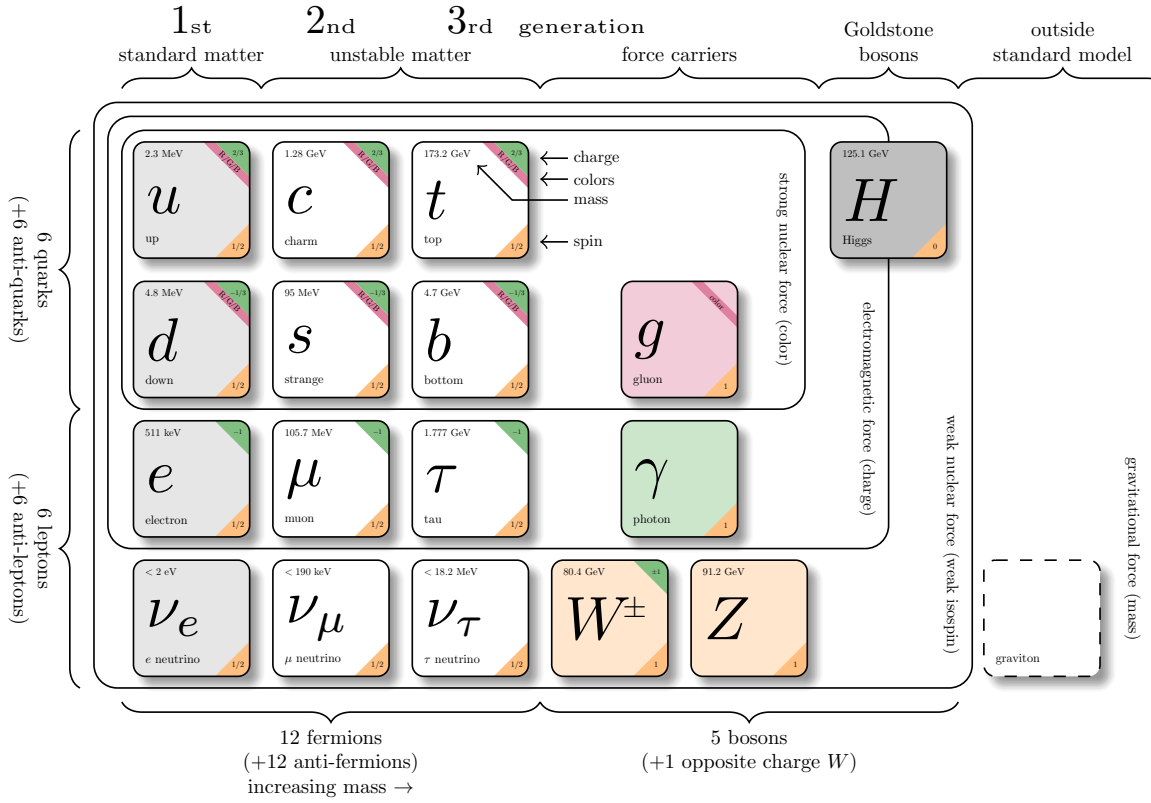


Figure 2.1: Particles within the SM and their properties [49].

## Fermions

Fermions consist of quarks and leptons with six flavors each, grouped into three generations of doublets. The six quark flavors are up ( $u$ ), down ( $d$ ), charm ( $c$ ), strange ( $s$ ), bottom ( $b$ ) and top ( $t$ ), arranged in increasing order of mass. The quark flavors form three doublets ( $u, d$ ), ( $c, s$ ) and ( $t, b$ ), with each doublet containing one quark with electric charge of  $+2/3$  ( $u, s, t$ ), and the other with charge of  $-1/3$  ( $d, c, b$ ). Each quark also possesses a property known as color charge, with possible values of red ( $R$ ), green ( $G$ ), blue ( $B$ ) or their corresponding anticolor ( $\bar{R}, \bar{G}, \bar{B}$ ). Color charge follows color confinement rules, which allows only configurations of quarks with total neutral color charge to exist in isolation. Neutral

charge configurations can be formed from either a set of three colors ( $R, G, B$ ), a set of a color and its anticolor, or any combination of the two. Consequently, quarks can only exist in bound states called hadrons and no isolated quark can be found in a vacuum. Quarks are the only elementary particles in the SM that can interact with all four fundamental forces.

The three leptons doublets consist of three charged leptons: electron ( $e$ ), muon ( $\mu$ ), tau ( $\tau$ ), and their respective neutrino flavors: electron neutrino ( $\nu_e$ ), muon neutrino ( $\nu_\mu$ ), tau neutrino ( $\nu_\tau$ ). Charged leptons carry an electric charge of  $-1$ , while their antiparticles carry the opposite charge ( $+1$ ) and their corresponding neutrino flavors carry no charge. Charged leptons interact with all fundamental forces except the strong force, while neutrinos only interact with the weak force and gravity.

## Bosons

The SM classifies bosons into two types: one scalar boson with spin 0 known as the Higgs ( $H$ ) boson, and vector gauge bosons with spin 1 known as gluons ( $g$ ), photon ( $\gamma$ ),  $W^\pm$  and  $Z$  bosons [22]. Gluons and photon are massless, while the  $W^\pm$ ,  $Z$  and  $H$  bosons are massive. Each vector gauge boson serves as the mediator for a fundamental force described by the SM. Gluons are massless particles mediating the strong interaction by carrying color charges between quarks following quantum chromodynamics (QCD). Each gluon carries a non-neutral color charge out of eight linearly independent color states in the gluon color octet [50]. The photon is the massless and charge-neutral mediator particle for the electromagnetic interaction following quantum electrodynamics (QED). The  $W^\pm$  and  $Z$  bosons are massive mediator particles for the weak interaction, with the  $W^\pm$  boson carrying an electric charge of  $\pm 1$  while the  $Z$  boson is charge neutral.

Other than the vector gauge boson, the only scalar boson in the SM is the massive and

charge neutral Higgs boson [22]. The Higgs boson does not mediate any fundamental force like vector bosons, but serve to provide the rest mass for all massive elementary particles in the SM through the Higgs mechanism described in section 2.1.2.3.

## Top quark

As of now, the top quark ( $t$ ) is the heaviest particle in the SM with mass of about 173 GeV [51], approaching the EW symmetry breaking scale. Its high mass gives the top quark the strongest Yukawa coupling to the Higgs boson ( $y_t \approx 1$ ) [24] and exotic resonances in many proposed BSM models [52–55], making the top quark and its processes attractive vehicles with which to probe new physics.

Due to its mass, the top quark has a very short lifetime of  $10^{-24}$  s [22] and decays before it can hadronize following color confinement. The top quark decays to a  $W$  boson and a  $b$ -quark with a branching ratio of almost 100%. The  $W$  boson can subsequently decay to a quark-antiquark pair or to a lepton-neutrino pair (Figure 2.2), with branching ratios of approximately 68% and 32% respectively. All lepton flavors have similar branching ratios during a leptonic  $W$  decay.

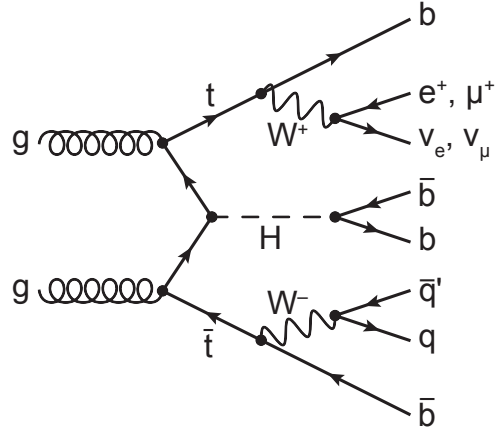


Figure 2.2: Feynman diagram for  $t\bar{t}$  production and subsequent decay processes [56]. Top quark decays into a  $W$ -boson and  $b$ -quarks, and  $W$ -boson can decay to a  $q\bar{q}$  or a  $\ell\nu_\ell$  pair.

### 2.1.2 Mathematical formalism

The SM can be described within the formalism of quantum field theory (QFT) with the Lagrangian [57]

$$\mathcal{L}_{\text{SM}} = \mathcal{L}_{\text{QCD}} + \underbrace{(\mathcal{L}_{\text{gauge}} + \mathcal{L}_{\text{fermion}} + \mathcal{L}_{\text{Higgs}} + \mathcal{L}_{\text{Yukawa}})}_{\mathcal{L}_{\text{EW}}} \quad (2.1)$$

where  $\mathcal{L}_{\text{QCD}}$  is the QCD term and  $\mathcal{L}_{\text{EW}}$  is the electroweak (EW) term of the Lagrangian. Formalism of QFT within the SM treats particles as excitations [58] of their corresponding quantum fields i.e. fermion field  $\psi$ , electroweak boson fields  $W_{1,2,3}$  &  $B$ , gluon fields  $G_\alpha$  and Higgs field  $\phi$ .

The foundation of modern QFT involves gauge theory. A quantum field has gauge symmetry if there exists a continuous gauge transformation that when applied to every point in a field (local gauge transformation) leaves the field Lagrangian unchanged. The set of gauge transformations of a gauge symmetry is the symmetry group of the field which comes with a set of generators, each with a corresponding gauge field. Under QFT, the quanta of these gauge fields are called gauge bosons.

The SM Lagrangian is gauge invariant under global Poincaré symmetry and local  $SU(3)_C \times SU(2)_L \times U(1)_Y$  gauge symmetry, with the  $SU(3)_C$  symmetry group corresponding to the strong interaction and  $SU(2)_L \times U(1)_Y$  to the EW interaction. Global Poincaré symmetry ensures that  $\mathcal{L}_{\text{SM}}$  satisfies translational symmetry, rotational symmetry and Lorentz boost frame invariance [59]. These symmetries give rise to corresponding conservation laws, which lead to conservation of momentum, angular momentum and energy in the SM as a result of Noether's theorem [60].

### 2.1.2.1 Quantum chromodynamics

Quantum chromodynamics is a non-Abelian gauge theory i.e. Yang-Mills theory [6, 7] describing the strong interaction between quarks in the SM with the gauge group  $SU(3)_C$ , where  $C$  represents conservation of color charge under  $SU(3)_C$  symmetry. According to QFT, quarks can be treated as excitations of the corresponding quark fields  $\psi$ . The free Dirac Lagrangian for the quark fields  $\mathcal{L}_0 = \bar{\psi}(i\gamma^\mu\partial_\mu - m)\psi$  is invariant under global  $SU(3)$  symmetry, but not under local  $SU(3)_C$  symmetry. To establish invariance under local  $SU(3)_C$  symmetry, the gauge covariant derivative  $D_\mu$  is defined so that

$$D_\mu\psi = (\partial_\mu - ig_s G_\mu^a T_a)\psi, \quad (2.2)$$

where  $g_s = \sqrt{4\pi\alpha_s}$  is the QCD coupling constant,  $G_\mu^a(x)$  are the eight gluon fields, and  $T_a$  are generators of  $SU(3)_C$ , represented as  $T_a = \lambda_a/2$  with  $\lambda_a$  being the eight Gell-Mann matrices [50]. Let the gluon field strength tensors  $G_{\mu\nu}^a$  be

$$G_{\mu\nu}^a \equiv \partial_\mu G_\nu^a - \partial_\nu G_\mu^a - g_s f^{abc} G_\mu^b G_\nu^c, \quad (2.3)$$

where  $f^{abc}$  are the structure constants of  $SU(3)_C$ . The gauge invariant QCD Lagrangian can then be written as

$$\begin{aligned} \mathcal{L}_{\text{QCD}} &= \bar{\psi}(i\gamma^\mu D_\mu - m)\psi - \frac{1}{4}G_{\mu\nu}^a G_a^{\mu\nu} \\ &= \underbrace{-\frac{1}{4}G_{\mu\nu}^a G_a^{\mu\nu}}_{\text{gluon kinematics}} + \underbrace{\bar{\psi}(i\gamma^\mu\partial_\mu - m)\psi}_{\text{quark kinematics \& masses}} + \underbrace{\bar{\psi}^i(g_s\gamma^\mu(T_a)_{ij}G_\mu^a)\bar{\psi}^j}_{\text{quark-gluon interaction}}, \end{aligned} \quad (2.4)$$

where  $i, j$  are color indices with integer values from 1 to 3. Gluons are forced to be massless from the lack of a gluon mass term to maintain gauge invariance for the Lagrangian.

### 2.1.2.2 Electroweak theory

The electroweak interaction is the unified description of the weak interaction and electromagnetism under the  $SU(2)_L \times U(1)_Y$  symmetry group, where  $L$  represents the left-handed chirality of the weak interaction and  $Y$  represents the weak hypercharge quantum number. Fermions can have either left-handed or right-handed chirality with the exception of neutrinos which can only have left-handed chirality within the SM framework. Fermions in the SM can be divided into left-handed doublets and right-handed singlets

$$\psi_L = \begin{pmatrix} \nu_e \\ e_L \end{pmatrix}, \begin{pmatrix} \nu_\mu \\ \mu_L \end{pmatrix}, \begin{pmatrix} \nu_\tau \\ \tau_L \end{pmatrix}, \begin{pmatrix} u_L \\ d_L \end{pmatrix}, \begin{pmatrix} c_L \\ s_L \end{pmatrix}, \begin{pmatrix} t_L \\ b_L \end{pmatrix} \quad (2.5)$$

$$\psi_R = e_R, \mu_R, \tau_R, u_R, d_R, c_R, s_R, t_R, b_R.$$

where  $g'$  is the  $B_\mu$  coupling constant and  $B_\mu(x)$  is a vector gauge field that transforms under  $U(1)_Y$  as

$$B_\mu \rightarrow B_\mu + \frac{1}{g'} \partial_\mu \theta(x). \quad (2.6)$$

Right-handed fermion singlets are not affected by  $SU(2)_L$  transformation, so the fermion fields  $\psi$  transform under  $SU(2)_L$  as

$$\psi_L \rightarrow e^{i I_3 \vec{\theta}(x) \cdot \vec{\sigma}/2} \psi_L \quad (2.7)$$

$$\psi_R \rightarrow \psi_R.$$

where  $\vec{\sigma}/2$  are generators of  $SU(2)_L$  with  $\vec{\sigma}$  being the Pauli matrices. In order to preserve local symmetry, the gauge covariant derivative for  $SU(2)_L$  and  $U(1)_Y$  can be defined [61] so

that the gauge covariant derivative for  $SU(2)_L \times U(1)_Y$  can be written as

$$\begin{aligned} D_\mu \psi_L &= \left( \partial_\mu - ig' \frac{Y_L}{2} B_\mu - ig \frac{\sigma_i}{2} W_\mu^i \right) \psi_L \\ D_\mu \psi_R &= \left( \partial_\mu - ig' \frac{Y_R}{2} B_\mu \right) \psi_R. \end{aligned} \quad (2.8)$$

where  $B_\mu(x)$  is a vector gauge field associated with  $U(1)_Y$  and  $W_\mu^i(x)$  ( $i = 1, 2, 3$ ) are three vector gauge fields associated with  $SU(2)_L$ . The  $B_\mu$  and  $W_\mu^i$  gauge fields transform under their corresponding symmetry groups  $U(1)_Y$  and  $SU(2)_L$  as

$$\begin{aligned} B_\mu &\rightarrow B_\mu + \frac{1}{g'} \partial_\mu \theta(x) \\ W_\mu^i &\rightarrow W_\mu^i + \frac{2}{g} \partial_\mu \theta_a(x) + \epsilon^{ijk} \theta_j(x) W_\mu^k, \end{aligned} \quad (2.9)$$

where  $g'$  is the  $B_\mu$  gauge coupling constant,  $g$  is the  $W_\mu^i$  gauge coupling constants and  $\epsilon^{ijk}$  is the  $SU(2)_L$  structure constant. Similar to section 2.1.2.1, the kinetic term is added by defining field strengths for the four gauge fields

$$\begin{aligned} B_{\mu\nu} &\equiv \partial_\mu B_\nu - \partial_\nu B_\mu \\ W_{\mu\nu}^i &\equiv \partial_\mu W_\nu^i - \partial_\nu W_\mu^i - g e^{ijk} W_\mu^j W_\nu^k. \end{aligned} \quad (2.10)$$

The local  $SU(2)_L \times U(1)_Y$  invariant EW Lagrangian [61] is then

$$\begin{aligned} \mathcal{L}_{\text{EW}} &= i\bar{\psi}(\gamma^\mu D_\mu)\psi - \frac{1}{4}W_{\mu\nu}^i W_i^{\mu\nu} - \frac{1}{4}B_{\mu\nu} B^{\mu\nu} \\ &= \underbrace{i\bar{\psi}(\gamma^\mu \partial_\mu)\psi}_{\text{fermion kinematics}} - \underbrace{\bar{\psi}\left(\gamma^\mu g' \frac{Y}{2} B_\mu\right)\psi}_{\text{fermion-gauge boson interaction}} - \underbrace{\bar{\psi}_L\left(\gamma^\mu g \frac{\sigma_i}{2} W_\mu^i\right)\psi_L}_{\text{boson kinematics \& self-interaction}} - \underbrace{\frac{1}{4}W_{\mu\nu}^i W_i^{\mu\nu} - \frac{1}{4}B_{\mu\nu} B^{\mu\nu}}_{\text{boson kinematics \& self-interaction}}. \end{aligned} \quad (2.11)$$

Under  $\approx 159.5$  GeV, the EW symmetry  $SU(2)_L \times U(1)_Y$  undergoes spontaneous symmetry breaking [62] into  $U(1)_{\text{QED}}$  symmetry, which corresponds to a separation of the weak and electrodynamic forces. Electroweak spontaneous symmetry breaking replaces the four massless and similarly-behaved EW gauge bosons  $B_\mu$  and  $W_\mu^i$  with the EM boson  $\gamma$  and the weak bosons  $Z/W^\pm$ , as well as giving the  $Z$  and  $W^\pm$  bosons masses via the Higgs mechanism. This is due to a specific choice of gauge for the Higgs field leading to the reparameterization of the EW bosons  $B_\mu$  and  $W_\mu^i$  to  $W^\pm/Z/\gamma$  using the relations

$$\begin{aligned} W_\mu^\pm &\equiv \frac{1}{\sqrt{2}} (W_\mu^1 \mp iW_\mu^2) \\ \begin{pmatrix} A_\mu \\ Z_\mu \end{pmatrix} &\equiv \begin{pmatrix} \cos \theta_W & \sin \theta_W \\ -\sin \theta_W & \cos \theta_W \end{pmatrix} \begin{pmatrix} B_\mu \\ W_\mu^3 \end{pmatrix} \end{aligned} \quad (2.12)$$

where  $\theta_W \equiv \cos^{-1} (g/\sqrt{g^2 + g'^2})$  is the weak mixing angle. The boson kinetic term can also be refactorized to extract cubic (three vertices) and quartic (four vertices) self-interactions among the gauge bosons [61]. The Lagrangian can then be rewritten as

$$\begin{aligned} \mathcal{L} = & \underbrace{eA_\mu \bar{\psi} (\gamma^\mu Q) \psi}_{\text{electromagnetism}} + \underbrace{\frac{e}{2 \sin \theta_W \cos \theta_W} \bar{\psi} \gamma^\mu (v_f - a_f \gamma_5) \psi Z_\mu}_{\text{neutral current interaction}} \\ & + \underbrace{\frac{g}{2\sqrt{2}} \sum_{\psi_L} [\bar{f}_2 \gamma^\mu (1 - \gamma_5) f_1 W_\mu^+ + \bar{f}_1 \gamma^\mu (1 - \gamma_5) f_2 W_\mu^-]}_{\text{charged current interaction}} \\ & + \underbrace{\mathcal{L}_{\text{kinetic}} + \mathcal{L}_{\text{cubic}} + \mathcal{L}_{\text{quartic}}}_{\text{boson self-interaction}} \end{aligned} \quad (2.13)$$

where  $\gamma_5 = i\gamma^0\gamma^1\gamma^2\gamma^3$  is the chirality projection operator,  $a_f = I_3$ ,  $v_f = I_3(1 - 4|Q| \sin^2 \theta_W)$  and  $f_1, f_2$  are up and down type fermions of a left-handed doublet.

### 2.1.2.3 Higgs mechanism

So far, the EW bosons are massless since the mass terms  $-m\bar{\psi}\psi$  for fermions and  $-mA^\mu A_\mu$  for bosons are not invariant under the EW Lagrangian symmetries. The particles must then acquire mass under another mechanism. The Brout-Engler-Higgs mechanism [11–13] was introduced in 1964 to rectify this issue and verified in 2012 with the discovery of the Higgs boson [20, 21].

The Higgs potential is expressed as

$$V(\phi^\dagger \phi) = \mu^2 \phi^\dagger \phi + \lambda (\phi^\dagger \phi)^2 \quad (2.14)$$

where  $\mu^2$  and  $\lambda > 0$  are arbitrary parameters, and the  $SU(2)_L$  doublet  $\phi = \begin{pmatrix} \phi^+ \\ \phi^0 \end{pmatrix}$  is the Higgs field with complex scalar fields  $\phi^+$  and  $\phi^0$  carrying +1 and 0 electric charge respectively.

The Lagrangian for the scalar Higgs field is

$$\mathcal{L}_H = (\partial_\mu \phi)^\dagger (\partial^\mu \phi) - V(\phi^\dagger \phi). \quad (2.15)$$

Since the potential  $V(\phi^\dagger \phi)$  is constrained by  $\lambda > 0$ , the ground state is solely controlled by  $\mu$ . If  $\mu^2 > 0$ , the ground state energy is  $\phi = 0$ , and the EW bosons would remain massless. If  $\mu^2 < 0$ , the ground state is

$$|\phi|^2 = -\frac{\mu^2}{2\lambda} \equiv \frac{v^2}{\sqrt{2}}, \quad (2.16)$$

where  $v$  is defined as the vacuum expectation value (VEV). The standard ground state for the Higgs potential without loss of generality can be chosen as  $\phi(0) = 1/\sqrt{2}(0_v)$ .

Having  $U(1)$  symmetry allows any  $-e^{i\theta} \sqrt{\mu^2/\lambda}$  to be a ground state energy for the Higgs

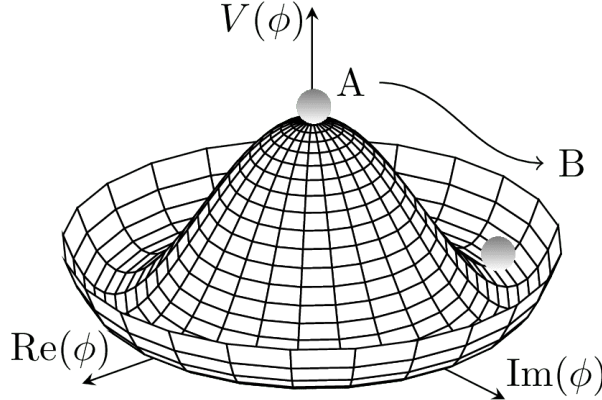


Figure 2.3: Illustration of a common representation of the Higgs potential [63]. Before SSB, the ground state  $\phi(0)$  is located at A which is symmetric with respect to the potential. A perturbation to this state fixes the ground state energy  $|\phi(0)|^2$  to a particular value at B, "spontaneously" breaking the symmetry and degeneracy in  $|\phi(0)|^2$ .

Lagrangian. This degeneracy results in spontaneous symmetry breaking of the  $SU(2)_L \times U(1)_Y$  symmetry into  $U(1)_{\text{EM}}$  symmetry when the Higgs field settles on a specific vacuum state as a result of a perturbation or excitation (Figure 2.3). The spontaneous symmetry breaking introduces three massless (Nambu-Goldstone [64]) vector gauge boson  $\xi$  and a massive scalar boson  $\eta$ , each corresponds to a generator of the gauge group. The vector field for  $\xi$  and  $\eta$  are real fields parameterized as  $\xi \equiv \phi^+ \sqrt{2}$  and  $\eta \equiv \phi^0 \sqrt{2} - v$  [65]. The Higgs field now becomes

$$\phi = \frac{v + \eta + i\xi}{\sqrt{2}} = \frac{1}{\sqrt{2}} e^{i\xi} \begin{pmatrix} 0 \\ v + \eta \end{pmatrix}. \quad (2.17)$$

Due to  $U(1)_{\text{EM}}$  invariance, a unitary gauge with the transformation  $\phi \rightarrow \exp(-i\xi \cdot) \frac{\sigma}{2v}$  can be chosen for the Higgs field to eliminate the massless bosons and incorporate them into the EM/weak bosons via Equation 2.12. This leaves the massive  $\eta$  which can now be observed as an excitation of the Higgs field from the standard ground state and must be the Higgs boson  $h$ . Using the EW covariant derivative from Equation 2.8, the Higgs Lagrangian around the

vacuum state becomes

$$\begin{aligned}\mathcal{L}_H &= (D_\mu \phi)^\dagger (D^\mu \phi) - \mu^2 \left( \frac{v+h}{\sqrt{2}} \right)^2 - \lambda \left( \frac{v+h}{\sqrt{2}} \right)^4 \\ &= (D_\mu \phi)^\dagger (D^\mu \phi) - \frac{1}{2} \mu^2 h^2 - \lambda v h^3 - \frac{\lambda}{4} h^4 - \dots\end{aligned}\tag{2.18}$$

The Higgs mass can be extracted from the quadratic term as  $m_H = \sqrt{-2\mu^2}$ . The kinetic term in the Lagrangian can be written as

$$\begin{aligned}(D_\mu \phi)^\dagger (D^\mu \phi) &= \frac{1}{2} (\partial_\mu h)^2 + \frac{g^2}{8} (v+h)^2 \left| W_\mu^1 - i W_\mu^2 \right|^2 + \frac{1}{8} (v+h)^2 (g' W_\mu - g B_\mu) \\ &= \frac{1}{2} (\partial_\mu h)^2 + (v+h)^2 \left( \frac{g^2}{4} W_\mu^+ W^{-\mu} + \frac{1}{8} (g^2 + g'^2) Z_\mu^0 Z^{0\mu} \right).\end{aligned}\tag{2.19}$$

Masses for the EW bosons can be extracted from the quadratic terms

$$m_{W^\pm} = \frac{v}{2} g, \quad m_Z = \frac{v}{2} \sqrt{g^2 + g'^2}, \quad m_\gamma = 0.\tag{2.20}$$

However, the fermion mass term  $-m\bar{\psi}\psi$  still breaks EW invariance after spontaneous symmetry breaking. Instead, fermions acquire mass by replacing the mass term with a gauge invariant Yukawa term in the EW Lagrangian representing fermions' interactions with the Higgs field [65]

$$\begin{aligned}\mathcal{L}_{\text{Yukawa}} &= -c_f \frac{v+h}{\sqrt{2}} (\bar{\psi}_R \psi_L + \bar{\psi}_L \psi_R) \\ &= -\underbrace{\frac{c_f}{\sqrt{2}} v (\bar{\psi} \psi)}_{\text{fermion mass}} - \underbrace{\frac{c_f}{\sqrt{2}} (h \bar{\psi} \psi)}_{\text{fermion-Higgs interaction}},\end{aligned}\tag{2.21}$$

where  $c_f$  is the fermion-Higgs Yukawa coupling. The fermion mass is then  $m_f = c_f v / \sqrt{2}$ .

## 2.2 Beyond the Standard Model: $t\bar{t}Z' \rightarrow t\bar{t}t\bar{t}$

This analysis uses the  $t\bar{t}t\bar{t}$  final state signal signature to search for the existence of a heavy neutral BSM resonance that couples strongly to the top quark, nominally named  $Z'$ . The cross-section for  $t\bar{t}t\bar{t}$  production at the LHC can be enhanced by many possible BSM models, in particular production of heavy scalars and pseudoscalar bosons predicted in Type-II two-Higgs-doublet models (2HDM) [39–43] or possible production of a heavy neutral resonance boson  $Z'(\rightarrow t\bar{t})$  in association with a  $t\bar{t}$  pair [66, 67]. The  $t\bar{t}Z'$  production mode and consequently  $t\bar{t}t\bar{t}$  signal signature can provide a more sensitive channel for searches by avoiding contamination from the large SM  $gg \rightarrow t\bar{t}$  background in an inclusive  $Z' \rightarrow t\bar{t}$  search.

### 2.2.1 Top-philic vector resonance

Many BSM models extend the SM by adding to the SM gauge group additional  $U(1)'$  gauge symmetries [68, 69], each with an associated vector gauge boson ( $Z'$ ). In the case of a BSM global symmetry group with rank larger than the SM gauge group, the symmetry group can spontaneously break into  $G_{\text{SM}} \times U(1)^{'n}$ , where  $G_{\text{SM}}$  is the SM gauge group  $SU(3)_C \times SU(2)_L \times U(1)_Y$  and  $U(1)^{'n}$  is any  $n \geq 1$  number of  $U(1)'$  symmetries. The existence of additional vector boson(s)  $Z'$  would open up many avenues of new physics e.g. extended Higgs sectors from  $U(1)'$  symmetry breaking [70, 71] and possible new particles as heavy  $Z'$  decay products [73].

Due to the top quark having the largest mass out of all known elementary particles in the SM, many BSM models [38–43, 74, 75] predict ‘top-philic’ vector resonances that have much stronger coupling to the top quark compared to other quarks. Previous BSM  $t\bar{t}t\bar{t}$  search at

the LHC for top-philic resonances [28] with a similar model in the single-lepton final state and similar mass ranges set upper limits on observed (expected)  $Z'$  production cross section between 21 (14) fb to 119 (86) fb depending on parameter choice. This analysis is also motivated by the recent observation of SM  $t\bar{t}t\bar{t}$  production in the same-sign multilepton (SSML) channel by ATLAS [44] and CMS [76] at  $6.1\sigma$  and  $5.6\sigma$  discovery significance respectively.

A simplified top-philic color-singlet vector particle model [45, 74] is employed in the search. The interaction Lagrangian assumes the  $Z'$  couples dominantly the top quark and has the form

$$\begin{aligned}\mathcal{L}_{Z'} &= \bar{t}\gamma_\mu (c_L P_L + c_R P_R) t Z'^\mu \\ &= c_t \bar{t}\gamma_\mu (\cos\theta P_L + \sin\theta P_R) t Z'^\mu,\end{aligned}\tag{2.22}$$

where  $c_t = \sqrt{c_L^2 + c_R^2}$  is the  $Z'$ -top coupling strength,  $P_{L/R} = (1 \mp \gamma_5)/2$  are the chirality projection operators, and  $\theta = \tan^{-1}(c_R/c_L)$  is the chirality mixing angle. Expanding the Lagrangian results in

$$\mathcal{L}_{Z'} = \frac{1}{\sqrt{2}} \bar{t}\gamma_\mu \left[ \sin\left(\theta + \frac{\pi}{4}\right) - \left( \sqrt{2} \cos\left(\theta + \frac{\pi}{4}\right) \right) \gamma_5 \right] t Z'^\mu,\tag{2.23}$$

which bears striking resemblance to the EW Lagrangian neutral current interaction term in Equation 2.13, showing the similarity between the  $Z'$  and the  $Z$  boson that acquires mass from  $SU(2)_L \times U(1)_Y$  spontaneous symmetry breaking. Assuming the  $Z'$  mass  $m_{Z'}$  is much larger than the top mass ( $m_t^2/m_{Z'}^2 \approx 0$ ), the  $Z'$  decay width at leading-order (LO) can be approximated as

$$\Gamma(Z' \rightarrow t\bar{t}) \approx \frac{c_t^2 m_{Z'}}{8\pi}.\tag{2.24}$$

It can be observed that  $\Gamma/m_{Z'} \approx c_t^2/8\pi \ll 1$  for  $c_t \approx 1$ , which suggests a very narrow and

well-defined resonance peak, validating the narrow-width approximation for the choice of  $c_t = 1$ .

### 2.2.2 Production channels

The main production channels at the LHC proton-proton collider for the aforementioned heavy topophilic color singlet  $Z'$  are at tree level and loop level, with the one-loop level being the dominant processes [45]. Loop level processes are dependent on the chirality angle  $\theta$ , where  $\theta = \pi/4$  suppresses all but gluon-initiated box sub-processes. To minimize model dependence, only the tree level production was considered for this analysis by choosing  $\theta = \pi/4$ . Figure 2.4 illustrates several tree level  $Z'$  production processes.

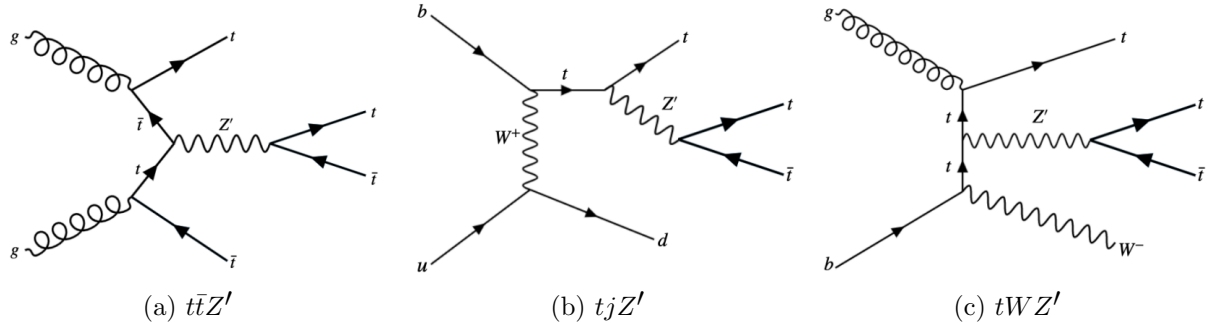


Figure 2.4: Feynman diagrams for tree level  $Z'$  production in association with (a)  $t\bar{t}$ , (b)  $tj$  (light quark) and (c)  $tW$ , decaying to final states containing (a)  $t\bar{t}t\bar{t}$  or (b)(c)  $t\bar{t}t$  [45].

The tree level  $t\bar{t}$ -associated process  $t\bar{t}Z'$  is the targeted production channel for the search in this dissertation. The  $t\bar{t}Z'$  cross-section at LO in QCD is shown in Figure 2.5. Contributions from the single-top-associated channels  $tjZ'$  and  $tWZ'$  are not considered due to a smaller cross-section by a factor of two compared to  $t\bar{t}Z'$  due to suppression in the three-body phase space [45]. Additionally,  $t\bar{t}Z' \rightarrow t\bar{t}t\bar{t}$  production is independent of  $\theta$  while  $tjZ'$  and  $tWZ'$  are minimally suppressed under pure left-handed interactions ( $\theta = 0$ ) and maximally suppressed under pure right-handed interactions ( $\theta = \pi/2$ ); both channels are

affected by the choice of  $\theta = \pi/4$  to suppress loop level production.

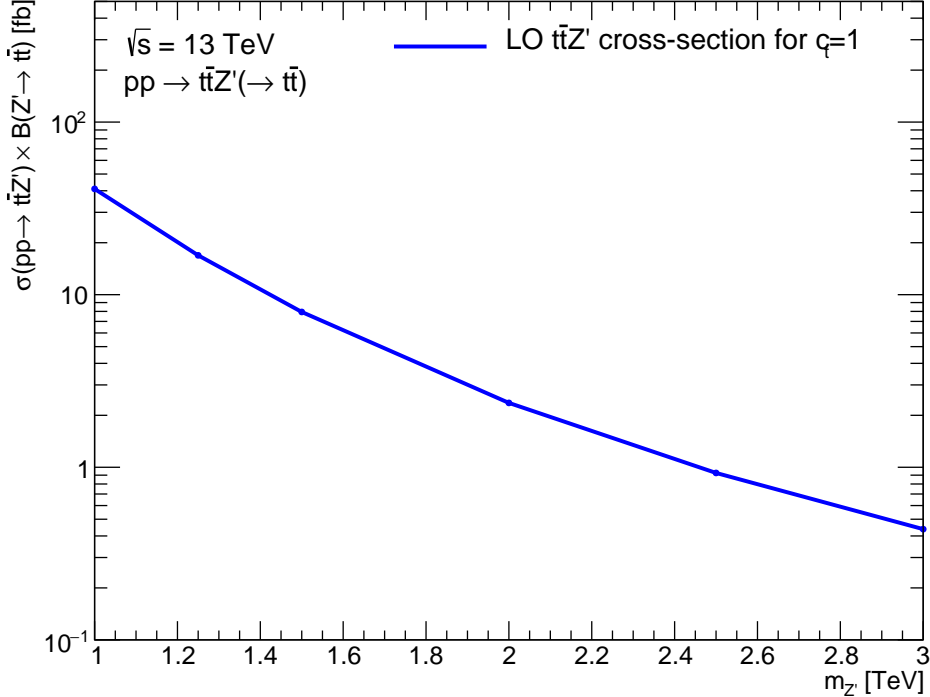


Figure 2.5: Theoretical  $t\bar{t}Z'$  production cross-section times  $Z' \rightarrow t\bar{t}$  branching ratio as a function of the  $Z'$  mass at LO in QCD coupling to top with  $c_t = 1$  under a simplified topophilic model [45, 74, 77].

### 2.2.3 Decay modes

The different  $W$  boson decay modes shown in Figure 2.2 result in many different final states for  $t\bar{t}Z'/t\bar{t}t\bar{t}$  decay, which can each be classified into one of three channels shown in Figure 2.6: all hadronic decays; exactly one lepton or two opposite-sign leptons (1LOS); exactly two same-sign leptons or three or more leptons (SSML). The branching ratio for each channel is shown in Figure 2.6. The all hadronic and 1LOS channels have much larger branching ratios compared to SSML channel but suffer heavily from  $gg \rightarrow t\bar{t}$  background contamination, giving the SSML channel better sensitivity at the cost of lower statistics.

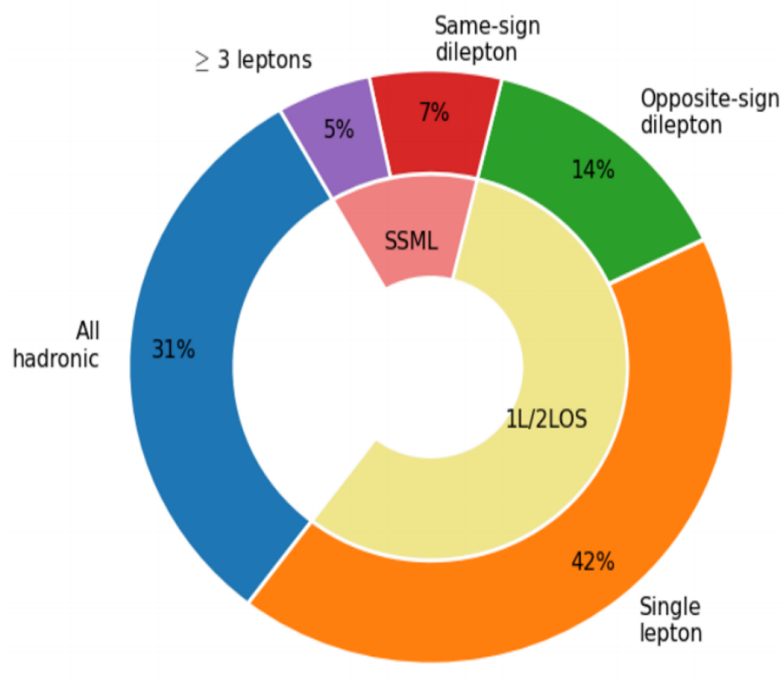


Figure 2.6: Branching ratios for  $t\bar{t}t\bar{t}$  decay [78]. The same-sign dilepton and multilepton channels together forms the SSML channel.

This is also the targeted channel for this analysis.

# Chapter 3. LHC & ATLAS Experiment

## 3.1 The Large Hadron Collider

Predictions from theoretical models are evaluated against experimental data collected from particle detectors. This chapter provides a detailed overview of the Large Hadron Collider (LHC) and the ATLAS detector, one of the key experiments designed to study high-energy collisions at the LHC.

### 3.1.1 Overview

The Large Hadron Collider [79] (LHC) is currently the world's largest particle collider with a circumference of almost 27 km. Built by CERN on the border of Switzerland and France, the LHC is designed as a particle collider for proton-proton ( $pp$ ), sometimes heavy ions i.e. lead-lead (PbPb) and proton-lead ( $pPb$ ) beams at TeV-scale energies. Two beams of particles are injected into the LHC in opposite directions and allowed to collide at the center of four major experiments:

- **A Toroidal LHC ApparatuS** (ATLAS) [27] and **Compact Muon Solenoid** (CMS) [80]: multi-purpose detectors, designed to target a variety of phenomena including SM, BSM and heavy-ion physics.
- **Large Ion Collider Experiment** (ALICE) [81]: specialized detector to record ion collisions and study heavy-ion physics.
- **Large Hadron Collider beauty** (LHCb) [82]: detector dedicated to study properties of  $b$ -quarks and  $b$ -hadrons.

Aside from the four major experiments, the LHC also houses smaller experiments e.g. AWAKE [83], FASER [84], KATRIN [85], that either share an interaction point with one of the above experiments or make use of particle beams pre-LHC injection.

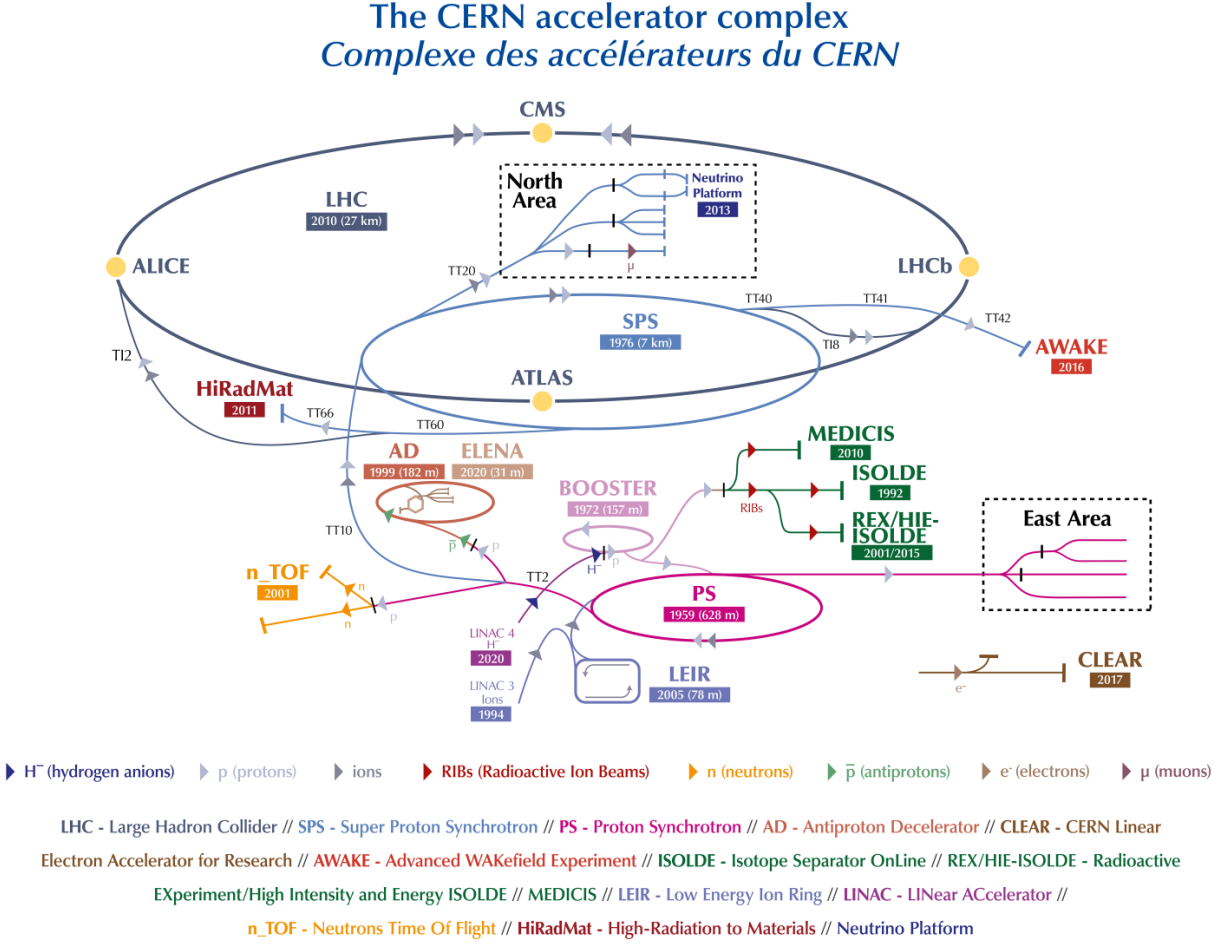


Figure 3.1: The full CERN accelerator complex as of 2022 [86].

The majority of the LHC operational time is dedicated to studying  $pp$  collisions of up to  $\sim 13$  TeV center-of-mass energy, denoted as  $\sqrt{s}$ . Reaching collision energy requires a sequence of accelerators within the CERN accelerator complex, shown in Figure 3.1. Proton production starts at LINAC 4, where hydrogen atoms are accelerated to 160 MeV then stripped of electrons. The leftover proton beams are injected into the Proton Synchrotron Booster

(PSB) and accelerated to 2 GeV before being transferred into the Proton Synchrotron (PS).

Here, the beams are ramped up to 26 GeV then injected into the Super Proton Synchrotron (SPS) to further raise the energy threshold to 450 GeV. The beams are finally injected into the LHC in opposite directions, continuously increasing in energy up to 6.5 TeV per beam, reaching the 13 TeV center-of-mass energy threshold necessary for collision during Run 2.

As of the start of Run 3 in 2022, proton beams can now be ramped up to 6.8 TeV per beam for a total of  $\sqrt{s} = 13.6$  TeV.

### 3.1.2 LHC operations

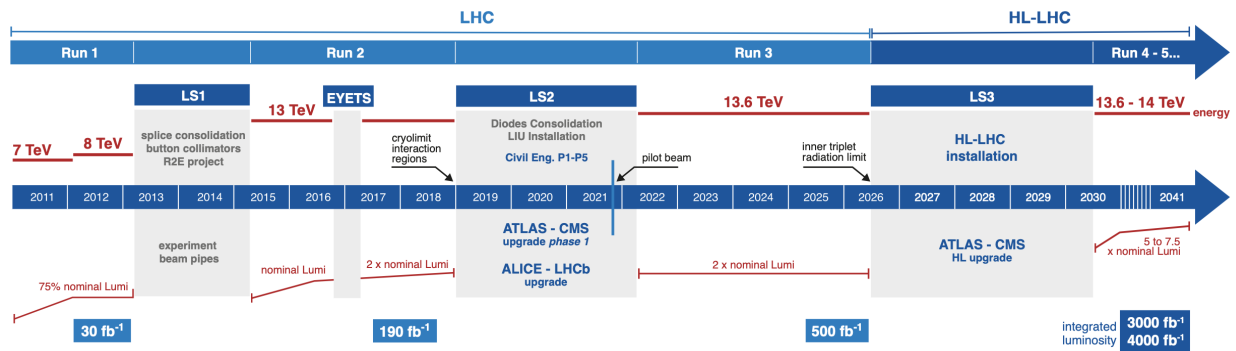


Figure 3.2: Current and future timeline of LHC operations with corresponding center-of-mass energies and projected integrated luminosities. [87].

Operations at the LHC are defined in periods of data-taking and shut-down known as runs and long shutdowns respectively; the first period (Run 1) started with first collisions at the LHC in 2010 at  $\sqrt{s} = 7$  TeV [88]. Upgrades are usually carried out for detectors and accelerators during long shutdowns, raising the maximum energy threshold in preparation for the next run. An overview of the LHC runtime and corresponding center-of-mass energies are summarized in Figure 3.2. During Run 2 from 2015-2018, the ATLAS detector recorded a total of  $1.1 \times 10^{16}$   $pp$  collisions at  $\sqrt{s} = 13$  TeV, which corresponds to an integrated

luminosity of  $140 \pm 0.83\% \text{ fb}^{-1}$  that passed data quality control and are usable for analyses [89]. This is also the data set used for the analysis in this dissertation.

### 3.1.3 Physics at the LHC

The majority of physics studied at the LHC focus primarily on QCD proton-proton hard scattering processes and the resulting products. Hard scattering processes involve large momentum transfer compared to the proton mass e.g. top pair production ( $gg \rightarrow t\bar{t}$ ) and Higgs production ( $gg \rightarrow H$ ), and can be predicted using perturbative QCD [90]. Hard processes probe distance scales much lower than the proton radius and can be considered collisions between the constituent quarks and gluons i.e. partons. Soft processes involve lower momentum transfer between partons and are dominated by less well-understood non-perturbative QCD effects. The hard interaction between two partons are represented by a parton distribution function (PDF)  $f_i(x, Q^2)$ , which describes the probability of interacting with a constituent parton  $i$  that carries a fraction  $x$  of the external hadron's momentum when probed at a momentum scale of  $Q^2$  [91]. Other partons within the hadron that did not participate in the collision can still interact via lower momentum underlying-events (UE). The probability of a particular interaction occurring is defined as its cross-section  $\sigma[b]$ . Figure 3.3 gives an overview of SM processes produced within the LHC and their cross-sections.

## 3.2 The ATLAS detector

One of the four main experiments at the LHC is ATLAS [27], designed as a multi-purpose detector for the role of studying high-energy physics in  $pp$  and heavy-ion collisions. ATLAS

## Standard Model Production Cross Section Measurements

Status: October 2023

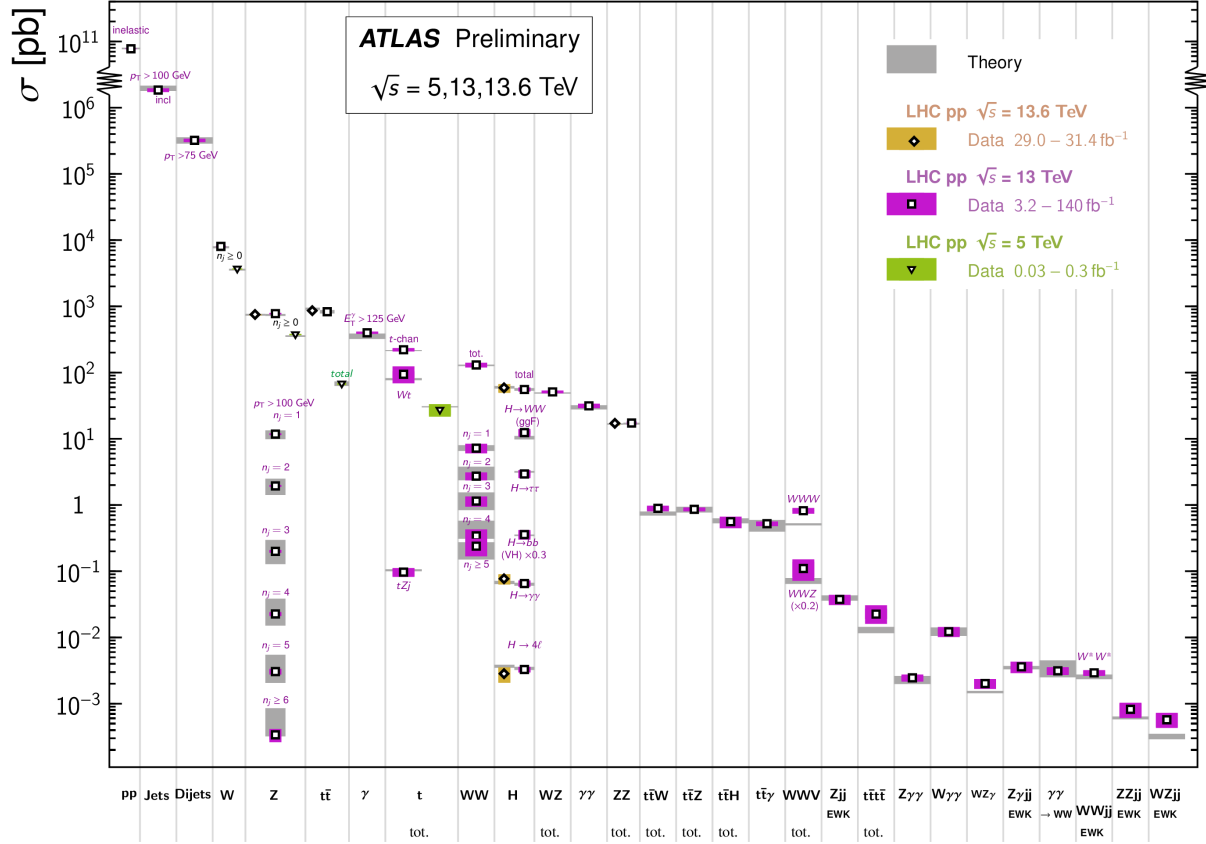


Figure 3.3: Summary of predicted and measured cross-section for SM processes at the LHC at different center-of-mass energies [92].

is a detector with symmetric cylindrical geometry with dimensions of 44 m in length and 25 m in diameter, covering a solid angle of almost  $4\pi$  around the collision point. The detector is built concentrically around the beamline with the collision point at the center to maximally capture signals produced by interactions. Figure 3.4 shows a slice of the ATLAS detector. From the inside out, the main ATLAS subdetector system consists of the inner detector (ID), calorimeter systems (electromagnetic and hadronic) and the muon spectrometer (MS).

The ATLAS detector uses a right-handed coordinate system [27] designed to align with the geometry of a collision interaction, with the origin set at the interaction point, the  $z$ -axis

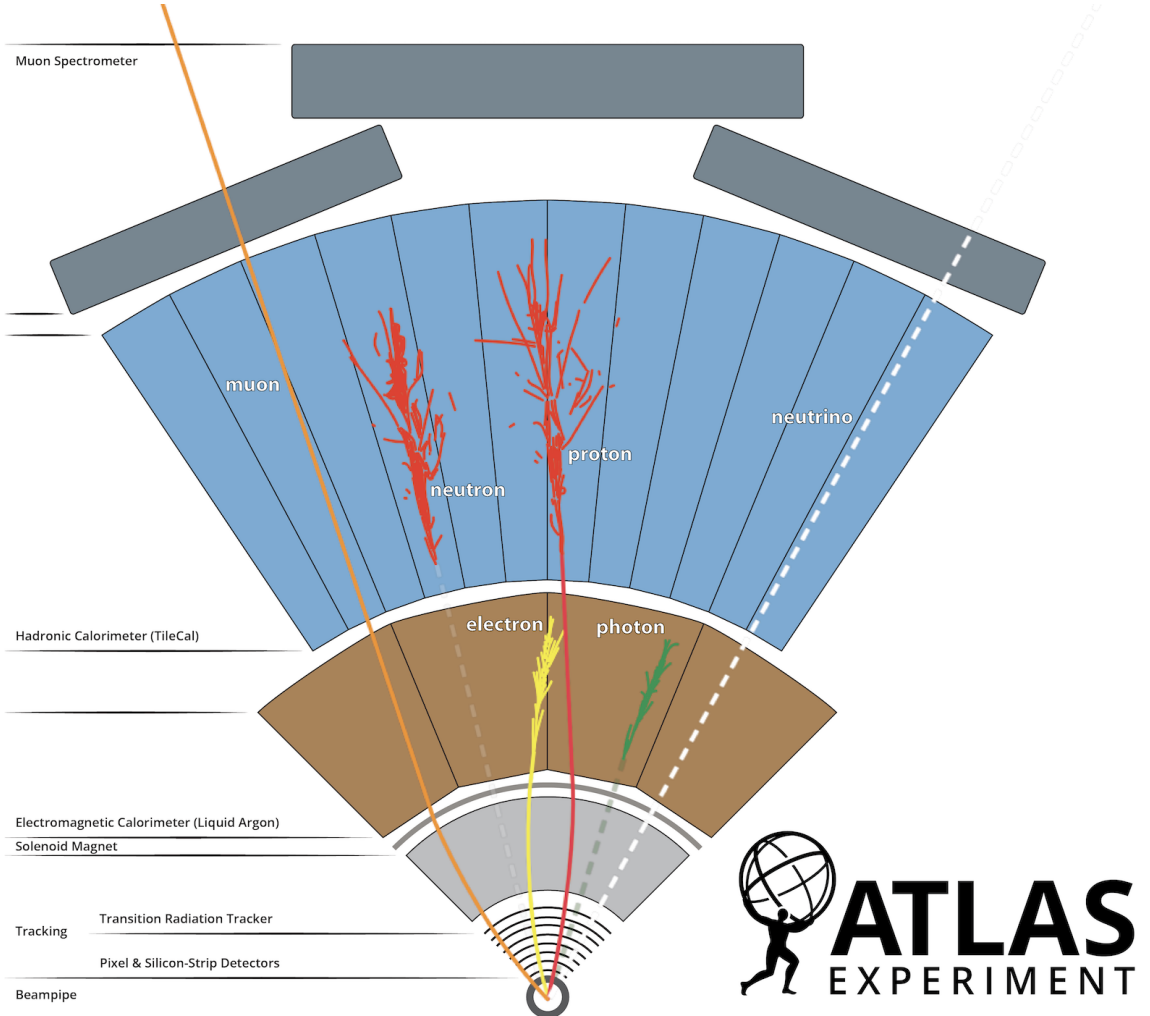


Figure 3.4: A cross section slice of the ATLAS detector showing different subsystems along with visualization of different types of particles traveling through the detector [93].

following (either of) the beamline and the  $x$ -axis pointing towards the center of the LHC ring. In cylindrical coordinates, the polar angle  $\theta$  is measured from the beam axis, and the azimuthal angle  $\phi$  is measured along the transverse plane ( $xy$ -plane) starting at the  $x$ -axis. Additional observables are defined for physics purposes: the pseudorapidity defined as  $\eta = -\ln \tan(\theta/2)$ ; angular distance within the detector defined as  $\Delta R = \sqrt{\Delta\eta^2 + \Delta\phi^2}$ ; and transverse momentum  $p_T$  (transverse energy  $E_T$ ) defined as the component of the particle's momentum (energy) projected onto the transverse plane.

### 3.2.1 Inner detector

The innermost part of ATLAS is the inner detector (ID) [27], constructed primarily for the purpose of measuring and reconstructing charged tracks within the  $|\eta| < 2.5$  region with high momentum resolution ( $\sigma_{p_T}/p_T = 0.05\% \pm 1\%$ ). Figure 3.5 shows the composition of the ID with three subsystems, the innermost being the pixel detector, then Semiconductor Tracker (SCT), and the Transition Radiation Tracker (TRT) on the outermost layer; all of which are surrounded by a solenoid magnet providing a magnetic field of 2 T.

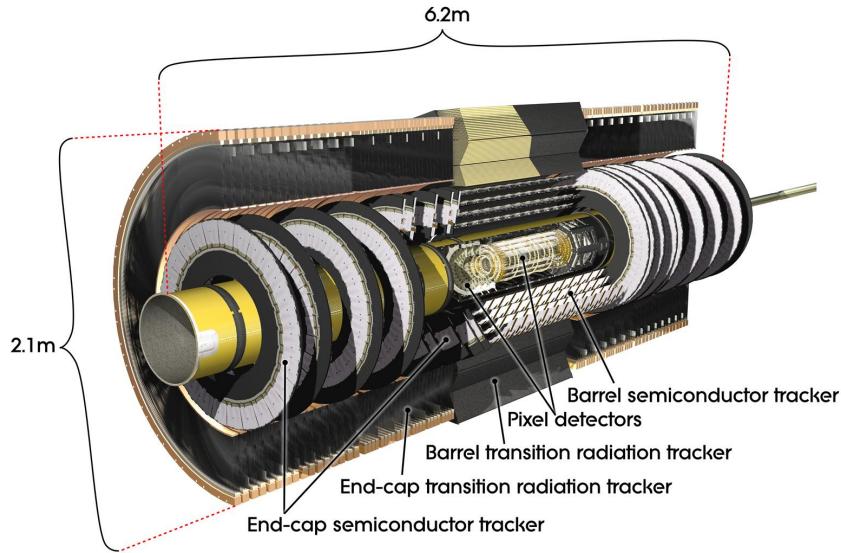


Figure 3.5: Cutaway illustration of the inner detector along with its subsystems [94].

#### Pixel detector

The pixel detector subsystem [27] consists of 250  $\mu\text{m}$  silicon semiconductor pixel layers with about 80.4 million readout channels, reaching a spatial resolution of 10  $\mu\text{m}$  in the  $R - \phi$  (transverse) plane and 115  $\mu\text{m}$  in the  $z$ -direction for charged tracks. Charged particles passing through the pixel detector ionize the silicon layers and produce electron-hole pairs;

the electrons drift towards the detector’s electrode under an applied electric field and the resulting electric signals are collected in read-out regions. The pixel detector is used primarily for impact parameter measurement, pile-up suppression, vertex finding and seeding for track reconstruction.

### Semiconductor Tracker

The Semiconductor Tracker (SCT) [27] functions similarly to the pixel detector, using silicon semiconductor microstrips totaling about 6.3 million read-out channels, reaching a per layer resolution of 17  $\mu\text{m}$  in the  $R\text{-}\phi$  plane and 580  $\mu\text{m}$  in the  $z$ -direction [27]. The SCT plays an important role in precise  $p_{\text{T}}$  measurement of charged particles as well as track reconstruction.

### Transition Radiation Tracker

The outermost layer of the ID, the Transition Radiation Tracker (TRT) [27], consists of layers of 4 mm diameter straw tubes filled with a xenon-based gas mixture and a 30  $\mu\text{m}$  gold-plated wire in the center. The TRT contains a total of about 351 thousand readout channels with a resolution of 130  $\mu\text{m}$  for each straw tube in the  $R\text{-}\phi$  plane, and provides extended track measurement, particularly estimation of track curvature under the solenoidal magnetic field. Importantly, the TRT also serves to identify electrons through absorption of emitted transition-radiation within the Xe-based gas mixture.

### 3.2.2 Calorimeter systems

Surrounding the ID is the ATLAS calorimeter system [27] with electromagnetic (EM) and hadronic calorimeters, covering a range of  $|\eta| < 4.9$ . The calorimeters are sampling calorime-

ters with alternating absorbing layers to stop incoming particles and active layers to collect read-out signals from energy deposits. Incoming particles passing through the calorimeters interact with the absorbing layers, producing EM or hadronic showers of secondary particles. The particle showers deposit energy in the corresponding layer of the calorimeters, which are collected and aggregated to identify and reconstruct the original particle's energy and direction. Figure 3.6 shows a schematic overview of the ATLAS calorimeter system.

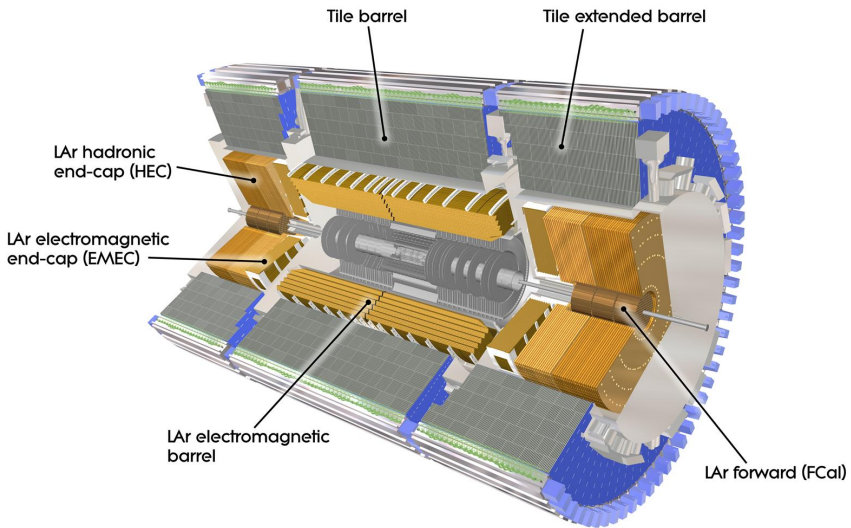


Figure 3.6: Cutaway illustration of the calorimeter system including the EM, hadronic and LAr forward calorimeters [95].

### Electromagnetic calorimeter

The EM calorimeter [27] covers the innermost part of the calorimeter system, with lead (Pb) absorbing layers and liquid argon (LAr) active layers to capture the majority of electrons and photons exiting the ID. The EM calorimeter is divided into regions depending on  $\eta$  coverage: a barrel region ( $|\eta| < 1.475$ ), two endcap regions ( $1.375 < |\eta| < 3.2$ ) and a transition region ( $1.372 < |\eta| < 1.52$ ). The endcap calorimeters are further divided into an

outer wheel region ( $1.372 < |\eta| < 2.5$ ) and an inner wheel region ( $2.5 < |\eta| < 3.2$ ) in order to provide precise coverage within the same  $\eta$  range as the ID. Overlap between the barrel and endcap regions compensates for the lower material density in the transition region.

## Hadronic calorimeter

The hadronic calorimeter [27] covers up to  $|\eta| < 4.9$  and is comprised of three parts: the tile calorimeter with a barrel region ( $|\eta| < 1.0$ ) and extended barrel regions ( $0.8 < |\eta| < 1.7$ ); the hadronic endcap calorimeter (HEC) covering  $1.5 < |\eta| < 3.2$ ; and the forward calorimeter (FCal) covering  $3.2 < |\eta| < 4.9$ . The tile calorimeter covers the EM calorimeter barrel region and uses steel as material for the absorbing layers with scintillating tiles for the active layers. Signals captured by scintillating tiles are read out from both sides using photomultiplier tubes. The HEC calorimeter covers the endcap regions of the EM calorimeter and uses a copper-LAr calorimeter layer scheme. The FCal is located close to the beamline providing coverage for particles traveling close to parallel with the beam axis. The subdetector contains three modules: one with copper absorbing layers optimized for EM measurements, and two with tungsten absorbing layers targeting hadronic cascades. All modules in the FCal use LAr as the active layer.

### 3.2.3 Muon spectrometer

Generally, the only particles that penetrate past the calorimeter layer are muons and neutrinos. The muon spectrometer (MS) [27] is situated on the outermost of the ATLAS detector and aims to track and measure muons within  $|\eta| < 2.7$ . The MS utilizes an array of toroid magnets to provide a magnetic field perpendicular to the muon trajectory, bending the track in order to measure its curvature. The magnetic field is powered by a large barrel

toroid ( $|\eta| < 1.4$ ) with strength of 0.5 T and two endcap toroid magnets ( $1.6 < |\eta| < 2.7$ ) of 1 T. Both types contribute to the magnetic field in the transition region ( $1.4 < |\eta| < 1.6$ ).

To measure the muon itself, four types of large gas-filled chambers known as muon chambers [27] are designed and constructed for two main goals: triggering on potential muon candidates entering the MS and tracking their trajectories through the detector with high precision. The tracking system include Monitored Drift Tubes (MDTs), which record muon track information over the entire MS  $\eta$  range ( $|\eta| < 2.7$ ). The MDTs are built with multiple layers of drift tubes and filled with a mixture of 93% Ar and 7% CO<sub>2</sub>. Muons passing through drift tubes in the MDT ionize the gas within each tube; signals are then recorded as freed electrons drift to read-out channels under an applied electric field. In the forward region ( $2.0 < |\eta| < 2.7$ ), Cathode Strip Chambers (CSCs) are included along with MDTs. The CSCs are multiwire proportional chambers built with higher granularity and shorter drift time than the MDTs to handle tracking in an environment with high background rates.

The MS trigger system includes Resistive Plate Chambers (RPCs) [27], which provide triggering in the barrel region ( $|\eta| < 1.05$ ) using parallel electrode plates made of resistive materials with a gas mixture inbetween. High voltage is applied to the plates, accelerating the electrons freed from ionized gas and creating a fast avalanche of charge, which is collected on external read-out strips almost instantaneously. Triggering and coarse position measurements in the endcap region ( $1.05 < |\eta| < 2.5$ ) is handled by Thin-Gap Chambers (TGCs). Similar to CSCs, TGCs are multiwire proportional chambers with a small wire gap ("thin-gap") and high applied voltage across the gap, resulting in fast response time giving TGCs the capabilities to identify muon candidates in real time.

### 3.2.4 Trigger & data acquisition

The LHC produces a colossal amount of collision data at a bunch crossing rate of 40 MHz with bunch spacing of 25 ns. The ATLAS Trigger and Data Acquisition (TDAQ) system [96] synchronously identifies and records interesting events for in-depth analysis. The ATLAS trigger system in Run 2 consists of two steps: Level-1 (L1) trigger and High-Level Trigger (HLT). Events failing any step in the trigger chain are permanently lost.

The L1 trigger hardware is divided into L1 calorimeter triggers (L1Calo) and L1 muon triggers (L1Muon) [96]. L1Calo trigger uses information from ATLAS calorimeter system to quickly identify signs of high  $p_T$  objects e.g. EM clusters, jets and missing transverse energy  $E_T^{\text{miss}}$  (section 4.4). Similarly, L1Muon uses information from the RPCs and TGCs of the MS to make quick decisions on potentially interesting muon candidates. Outputs from L1Calo and L1Muon are fed into the L1 topological trigger (L1Topo) for additional filtering based on event topology and multi-object correlation, allowing for more selective and physics-motivated triggering. Decisions from all three types of L1 triggers are provided as inputs for the Central Trigger Processor (CTP) for a final Level-1 Accept (L1A) decision. The entire L1 trigger chain results in a 2.5  $\mu\text{s}$  latency and reduces the event rate to 100 kHz.

Events passing L1 triggers are sent to HLTs before being saved to offline storage at CERN data centers. HLTs are software-based triggers used for more complex and specific selections on physics objects required by targeted analysis goals, in turn requiring more computing power with longer latency. After HLT selections, the event rate is reduced to 1 kHz on average [96]. Overall, the full trigger chain reduces the event rate for ATLAS by approximately a factor of  $4 \times 10^4$ .

# Chapter 4. Particle Reconstruction & Identification

Activity within the ATLAS detector is recorded as raw electronic signals, which can be utilized by ATLAS reconstruction software to derive physics objects for analysis. This chapter describes the reconstruction and identification of basic objects (e.g. interaction vertices, tracks, topological clusters of energy deposits) and subsequently of complex physics objects i.e. particles and particle signatures.

## 4.1 Primary reconstruction

### 4.1.1 Tracks

Charged particles traveling through the ATLAS detector deposit energy in different layers of the ID and MS. The ID track reconstruction software consists of two algorithm chains: inside-out and outside-in track reconstruction [97–99].

The inside-out algorithm is primarily used for the reconstruction of primary particles i.e. particles directly produced from  $pp$  collisions or decay products of short-lived particles. The process starts by forming space points from seeded hits in the silicon detectors within the pixel & SCT detectors. Hits further away from the interaction vertex are added to the track candidate using a combinatorial Kalman filter [100] pattern recognition algorithm. Track candidates are then fitted with a  $\chi^2$  filter [101] and loosely matched to a fixed-sized EM cluster. Successfully matched track candidates are re-fitted with a Gaussian-sum filter (GSF) [102], followed by a track scoring strategy to resolve fake tracks & hit ambiguity

between different tracks [103]. The track candidate is then extended to the TRT to form final tracks satisfying  $p_T > 400$  MeV. The outside-in algorithm handles secondary tracks mainly produced from long-lives particles or decays of primary particles by back-tracking from TRT segments, which are then extended inward to match silicon hits in the pixel and SCT detectors to form track reconstruction objects.

#### 4.1.2 Vertices

Vertices represent the point of interaction or decay for particles within the ATLAS detector. Primary vertices (PVs) are defined as the point of collision for hard-scattering  $pp$  interactions, while secondary or displaced vertices result from particle decays occurring at a distance from its production point.

Reconstruction of PVs is crucial to accurately profile the kinematic information of an event and form a basis for subsequent reconstruction procedures. Primary vertex reconstruction occurs in two stages: vertex finding and vertex fitting [104]. The vertex finding algorithm uses the spatial coordinates of reconstructed tracks to form the seed for a vertex candidate. An adaptive vertex fitting algorithm [105] then iteratively evaluates track-vertex compatibility to estimate a new best vertex position. Less compatible tracks are down-weighted in each subsequent iteration, and incompatible tracks are removed and can be used for another vertex seed; the process is repeated until no further PV can be found. All reconstructed vertices without at least two matched tracks are considered invalid and discarded.

Secondary vertex reconstruction uses the Secondary Vertex Finder (SVF) algorithm [106] which is primarily designed to reconstruct  $b$ - and  $c$ -hadrons for flavor tagging purposes. The SVF aims to reconstruct one secondary vertex per jet and only considers tracks that are

matched to a two-track vertex and contained within a  $p_T$ -dependent cone around the jet axis. The tracks are then used to reconstruct a secondary vertex candidate using an iterative process similar to the PV vertex fitting procedure.

## Pile-up

At high luminosities, multiple interactions can be associated with one bunch crossing, resulting in many PVs. The effect is called pile-up [107], and usually result from soft QCD interactions. Pile-up can be categorized into two types: in-time pile-up, stemming from additional  $pp$  collisions in the same bunch crossing that is not the hard-scatter process; out-of-time pile-up, resulting from leftover energy deposits in the calorimeters from other bunch crossings.

### 4.1.3 Topological clusters

Topological clusters (topo-clusters) [108] consist of clusters of spatially related calorimeter cell signals. Topo-clusters are primarily used to reconstruct hadron- and jet-related objects in an effort to extract signal while minimizing electronic effects and physical fluctuations, and also allow for recovery of energy lost through bremsstrahlung or photon conversions. Cells with signal-to-noise ratio  $\varsigma_{\text{cell}}^{\text{EM}}$  passing a primary seed threshold are seeded into a dynamic topological cell clustering algorithm as part of a proto-cluster. Neighboring cells satisfying a cluster growth threshold are collected into the proto-cluster. If a cell is matched to two proto-clusters, the clusters are merged. Two or more local signal maxima in a cluster satisfying  $E_{\text{cell}}^{\text{EM}} > 500 \text{ MeV}$  suggest the presence of multiple particles in close proximity, and the cluster is split accordingly to maintain good resolution of the energy flow. The process continues iteratively until all cells with  $\varsigma_{\text{cell}}^{\text{EM}}$  above a principal cell filter level have been matched to a

cluster.

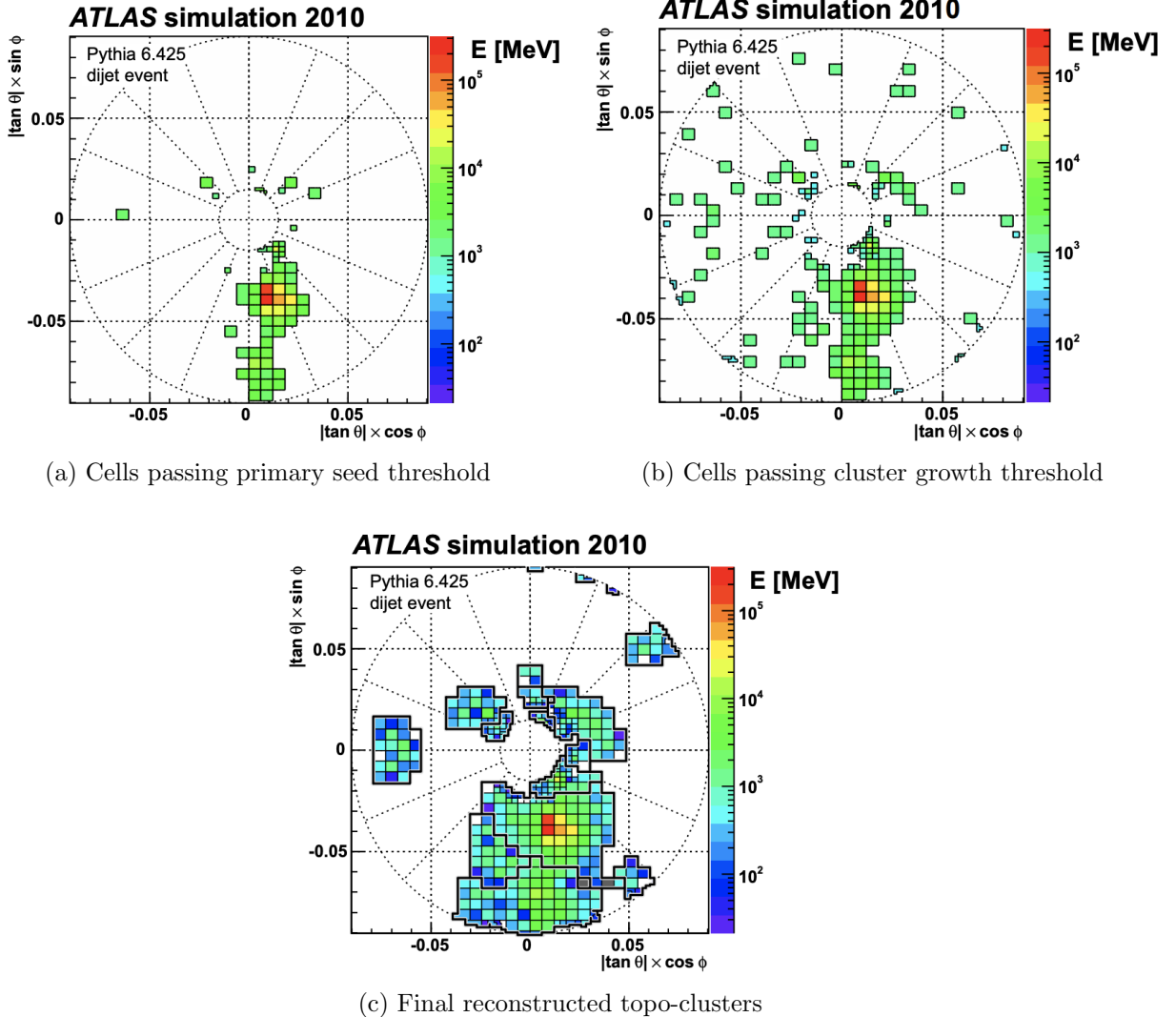


Figure 4.1: Stages of topo-cluster formation corresponding to each threshold. In (a), proto-clusters are seeded from cells with adequate signal significance  $\zeta_{\text{cell}}^{\text{EM}}$ . The clusters are further merged and split in (b) following a predefined cluster growth threshold. The process stops in (c) when all sufficiently significant signal hits have been matched to a cluster [108].

## 4.2 Jets

Quarks, gluons and other hadrons with non-neutral color charge cannot be observed individually due to QCD color confinement, which forces a non-color-neutral hadron to

almost immediately undergo hadronization, producing a collimated cone of color-neutral hadrons defined as a jet. Jet signals can be used to reconstruct and indirectly observe the quarks or gluons from which the jet originated in the original hard-scattering process.

### 4.2.1 Jet reconstruction

The ATLAS jet reconstruction pipeline is largely carried out using a particle flow (PFlow) algorithm combined with an anti- $k_t$  jet clustering algorithm. The PFlow algorithm [109] utilizes topo-clusters along with information from both the calorimeter systems and the ID in order to make use of the tracker system’s advantages in low-energy momentum resolution and angular resolution. First, the energy from charged particles is removed from the calorimeter topo-clusters; then, it is replaced by particle objects created using the remaining energy in the calorimeter and tracks matched to topo-clusters. The ensemble of ”particle flow objects” and corresponding matched tracks are used as inputs for the iterative anti- $k_t$  algorithm [110].

The main components of the anti- $k_t$  algorithm involve the distance  $d_{ij}$  between two jet candidates  $i$  and  $j$ , and the distance  $d_{iB}$  between the harder jet candidate of the two (defined as  $i$ ) and the beamline  $B$ . If  $d_{ij} < d_{iB}$ , then the two jet candidates are combined and returned to the pool of candidates; otherwise, jet candidate  $i$  is considered a jet and removed from the pool. The distance  $d_{ij}$  is inversely proportional to a predefined radius parameter  $\Delta R$  in order to control reconstruction quality for small- $R$  and large- $R$  jets. This analysis uses  $\Delta R = 0.4$  to better handle heavily collimated small- $R$  jets resulting from parton showers.

The anti- $k_t$  jets so far have only been reconstructed at the EM level and need to be calibrated to match the energy scale of jets reconstructed at particle level. This is done via a MC-based jet energy scale (JES) calibration sequence, along with further calibrations

to account for pile-up effects and energy leakage. The full JES calibration sequence is shown in Figure 4.2. All calibrations except origin correction are applied to the jet's four-momentum i.e. jet  $p_T$ , energy and mass. Afterwards, a jet energy resolution (JER) [111] calibration step is carried out in a similar manner to JES to match the resolution of jets in dijet events. To further suppress pile-up effects, a neural-network based jet vertex tagger (NNJvt) discriminant was developed based on the previous jet vertex tagger (JVT) algorithm [107] and applied to low- $p_T$  reconstructed jets.

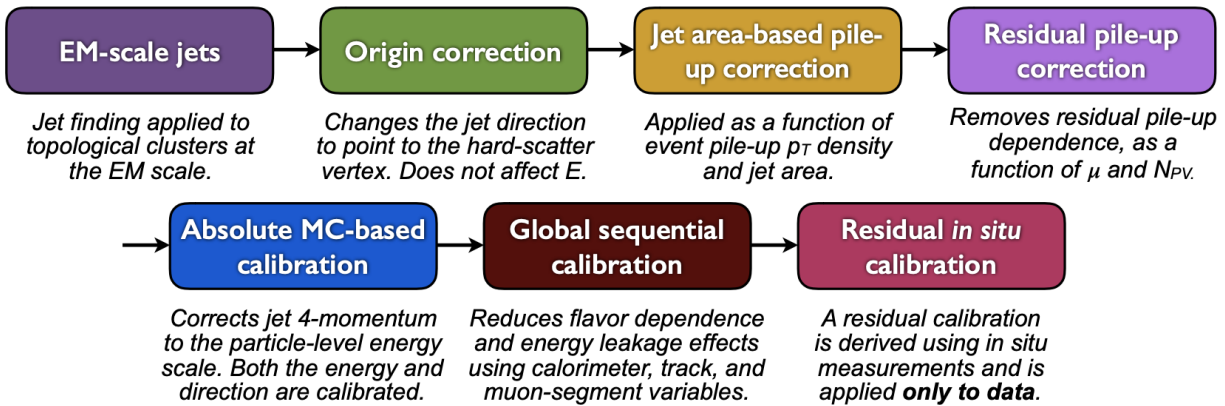


Figure 4.2: Jet energy scale calibration sequence for EM-scale jets [112].

#### 4.2.2 Flavor tagging

Identifying and classifying hadronic jets are important tasks for ATLAS physics, for example analyses involving Higgs decays  $H \rightarrow b\bar{b}$  or top quarks. Flavor tagging or  $b$ -tagging is the process of identifying jets containing  $b$ -hadrons,  $c$ -hadrons, light-hadrons ( $uds$ -hadrons) or jets from hadronically decaying  $\tau$  leptons. Distinguishing  $b$ -jets is possible due to their characteristically long lifetime ( $\tau \approx 1.5$  ps), displaced secondary decay vertex and high decay multiplicity.

Usage of  $b$ -tagging in this analysis is done via five operating points (OPs), corresponding

to 65%, 70%, 77%, 85% and 90%  $b$ -jet tagging efficiency  $\varepsilon_b$  in simulated  $t\bar{t}$  events, in order from the tightest to loosest discriminant cut point. The OPs are defined by placing selections on the tagger output to provide a predefined  $\varepsilon_b$  level; the selection cuts act as a variable trade-off between  $b$ -tagging efficiency and  $b$ -jet purity i.e.  $c$ - or light-jet rejection. For this analysis, a jet is considered  $b$ -tagged if it passes the 85% OP. The  $b$ -tagged jet is then assigned a pseudo-continuous  $b$ -tagging (PCBT) score, which quantifies a jet's ability to satisfy different OPs. The score can take integer values between 1 and 6, where a score of 6 is assigned to jets passing all OP thresholds; a score of 2 for jets that pass only the tightest OP (90%); and a score of 1 for jets that pass no OP. A value of -1 is also defined for any jet that does not satisfy  $b$ -tagging criteria. Since the targeted  $t\bar{t}t\bar{t}$  final states contain at least four  $b$ -hadrons from top and  $W$  decays, a  $b$ -tagging OP of 85% is used to maintain high purity during  $b$ -tagged jet selections in the signal region.

## **GN2 $b$ -tagging algorithm**

For this analysis,  $b$ -jets are identified and tagged with the GN2v01  $b$ -tagger [113]. The GN2 algorithm uses a Transformer-based model [114] modified to incorporate domain knowledge and additional auxiliary physics objectives: grouping tracks with a common vertex and predicting the underlying physics process for a track. The network structure is shown in Figure 4.3. The GN2  $b$ -tagger form the input vector by concatenating 2 jet variables and 19 track reconstruction variables (for up to 40 tracks), normalized to zero mean and unit variance. The output consists of a track-pairing output layer of size 2, a track origin classification layer of 7 categories, and a jet classification layer of size 4 for the probability of each jet being a  $b$ -,  $c$ -, light- or  $\tau$ -jet respectively. For  $b$ -tagging purpose, a discriminant is

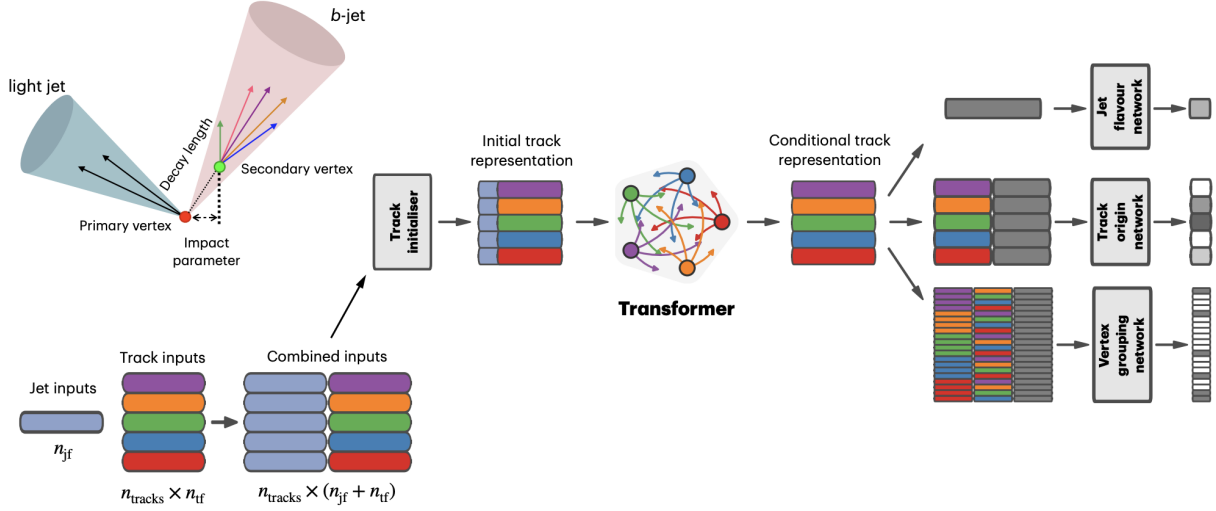


Figure 4.3: Overview of the GN2 architecture. The number of jet and track features are represented by  $n_{\text{jf}}$  and  $n_{\text{tf}}$  respectively. The global jet representation and track embeddings output by the Transformer encoder are used as inputs for three task-specific networks [113].

defined using these four outputs

$$D_b = \ln \left( \frac{p_b}{f_c p_c + f_\tau p_\tau + (1 - f_c - f_\tau)p_{\text{light}}} \right) \quad (4.1)$$

where  $p_x$  is the probability of the jet being an  $x$ -jet as predicted by GN2, and  $f_c$ ,  $f_\tau$  are tunable free parameters controlling balance between  $c$ - and light-jet rejection. Simulated SM  $t\bar{t}$  and BSM  $Z'$  events from  $pp$  collisions were used as training and evaluation samples. In order to minimize bias, both  $b$ - and light-jet samples are re-sampled to match  $c$ -jet distributions. Figure 4.4 shows the performance of GN2 compared to the previous convolutional neural network-based standard  $b$ -tagging algorithm DL1d, in terms of  $c$ -, light- and  $\tau$ -jet rejection as a function of  $b$ -tagging efficiency. The network gives a factor of 1.5-4 improvement in experimental applications compared to DL1d [113], without dependence on the choice of MC event generator or inputs from low-level flavor tagging algorithm.

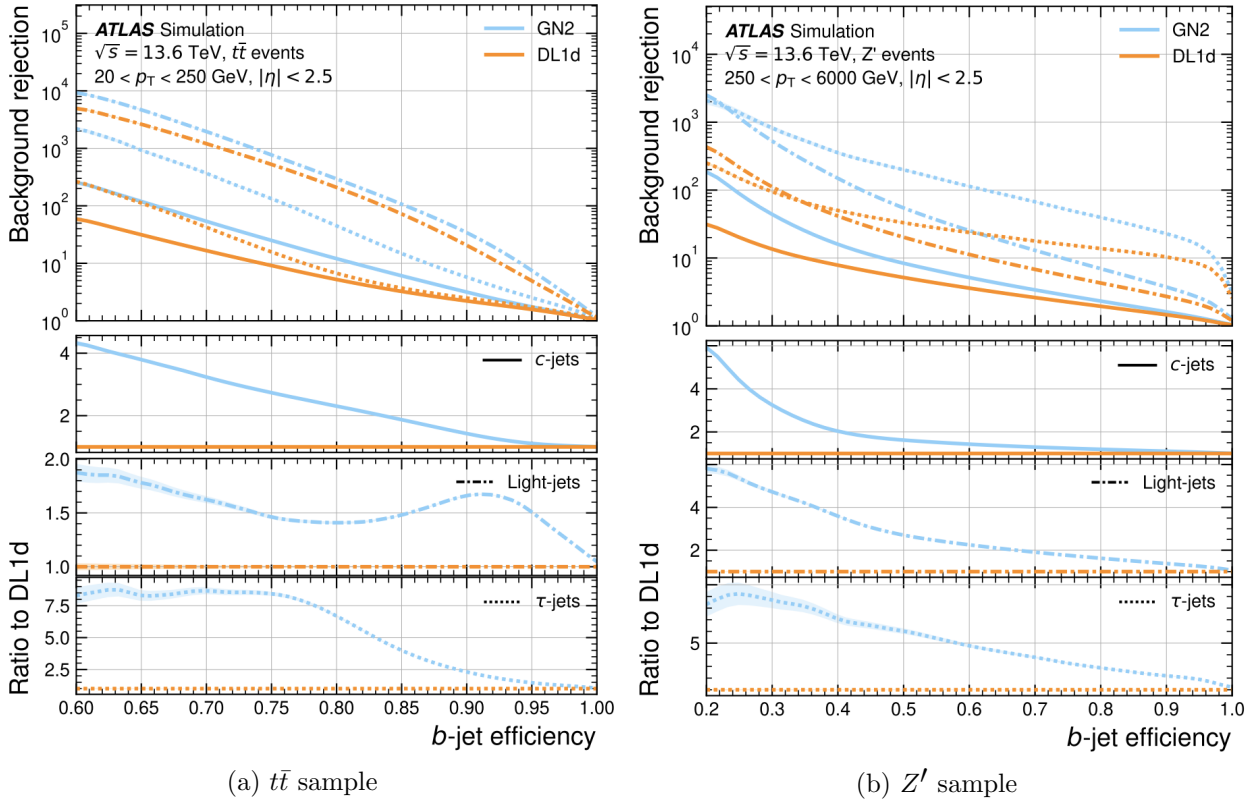


Figure 4.4: The  $c$ -, light- and  $\tau$ -jet rejection rate as a function of  $b$ -tagging efficiency for GN2 and DL1d using (a) jets in the  $t\bar{t}$  sample, and (b) jets in the  $Z'$  sample. The performance ratios of GN2 to DL1d are shown in the bottom panels [113].

## Efficiency calibration

Due to imperfect description of detector response and physics modeling effects in simulation, the  $b$ -tagging efficiency predicted by MC simulation  $\varepsilon_b^{\text{sim}}$  requires a correction factor to match the efficiency measured in collision data  $\varepsilon_b^{\text{data}}$ . The correction scale factors (SFs) are defined as  $\text{SF} = \varepsilon_b^{\text{data}} / \varepsilon_b^{\text{sim}}$  and are determined by data-to-MC calibration using samples enriched in dileptonic  $t\bar{t}$  decays [115]. The resulting SFs are applied to MC simulated jets individually.

## 4.3 Leptons

Lepton reconstruction in ATLAS involves electron and muon reconstruction since tau decays quickly, and depending on decay mode can be reconstructed using either jets or light leptons. From here on out within this dissertation, leptons will be used exclusively to refer to electrons and muons. Leptons can be classified into two categories: prompt leptons resulting from heavy particle decays and non-prompt leptons resulting from detector or reconstruction effects, or from heavy-flavor hadron decays.

### 4.3.1 Electrons

Electrons leave energy signature in the detector by interacting with the detector materials and losing energy in the form of bremsstrahlung photons. A bremsstrahlung photon can produce an electron-positron pair which can itself deposit signals in the detector, creating a cascade of particles that can leave multiple of either tracks in the ID or EM showers in the calorimeters, all of which are considered part of the same EM topo-cluster. Electron signal signature has three characteristic components: localized energy deposits in the calorimeters, multiple tracks in the ID and compatibility between the above tracks and energy clusters in the  $\eta \times \phi$  plane [116]. Electron reconstruction in ATLAS follows these steps accordingly.

Seed-cluster reconstruction and track reconstruction are performed sequentially in accordance with the iterative topo-clustering algorithm and track reconstruction method described in section 4.1. The seed-cluster and GSF-refitted track candidate not associated with a conversion vertex are matched to form an electron candidate. The cluster energy is then calibrated using multivariate techniques on data and simulation to match the original electron energy.

## Electron identification

Additional LH-based identification selections using ID and EM calorimeter information are implemented to further improve the purity of reconstructed electrons in the  $|\eta| < 2.47$  region of the detector [116]. The electron LH function is built with the signal being prompt electrons and background being objects with similar signature to prompt electrons i.e. hadronic jet deposits, photon conversions or heavy-flavor hadron decays. Three identification OPs are defined for physics analyses: *Loose*, *Medium* and *Tight*, optimized for 9 bins in  $|\eta|$  and 12 bins in  $E_T$  with each OP corresponding to a fixed efficiency requirement for each bin. For typical EW processes, the target efficiencies for *Loose*, *Medium* and *Tight* start at 93%, 88% and 80% respectively and increase with  $E_T$ . Similar to  $b$ -tagging OPs, the electron identification OPs represent a trade-off in signal efficiency and background rejection. The electron efficiency are estimated using tag-and-probe method on samples of  $J/\Psi \rightarrow ee$  and  $Z \rightarrow ee$  [116]. The *Tight* electron identification OP is used for this analysis.

## Electron isolation

A characteristic distinction between prompt electrons and electrons from background processes is the relative lack of activity in both the ID and calorimeters within an  $\Delta\eta \times \Delta\phi$  area surrounding the reconstruction candidate. Calorimeter-based and track-based electron isolation variables [116] are defined to quantify the amount of activity around the electron candidate using topo-clusters and reconstructed tracks respectively.

Calorimeter-based isolation variables  $E_T^{\text{cone}XX}$  are computed by first summing the energy of topo-clusters with barycenters falling within a cone of radius  $\Delta R = \sqrt{(\Delta\eta)^2 + (\Delta\phi)^2} = XX/100$  around the direction of the electron candidate. The final isolation variables are

obtained by subtracting from the sum the energy belonging to the candidate electron at the core of the cone, then applying corrections for pile-up effects and energy leakage outside of the core. Similar to calorimeter-based variables, track-based isolation variables  $p_T^{\text{varcone}XX}$  are calculated by summing all track  $p_T$  within a cone of radius  $\Delta R$  around the electron candidate, minus the candidate's contribution. The cone radius is variable as a function of  $p_T$  and is described as

$$\Delta R \equiv \min \left( \frac{10}{p_T}, \Delta R_{\max} \right), \quad (4.2)$$

where  $p_T$  is expressed in GeV and  $\Delta R_{\max}$  is the maximum cone size, defined to account for closer proximity of decay products to the electron in high-momentum heavy particle decays. Four isolation operating points are implemented to satisfy specific needs by physics analyses: *Loose*, *Tight*, *HighPtCaloOnly* and *Gradient* [116]. For this analysis, electrons isolation uses *Tight* requirements.

## Electron charge misidentification

Charge misidentification is a crucial irreducible background, particularly for analyses with electron charge selection criteria. Electron charge is determined by the curvature of the associated reconstructed track, and misidentification of charge can occur via either an incorrect curvature measurement or an incorrectly matched track. Inaccurate measurement is more likely for high energy electrons due to the small curvature in track trajectories at high  $p_T$ , while track matching error usually results from bremsstrahlung pair-production generating secondary tracks in close proximity [116]. Suppression of charge misidentification background in Run 2 is additionally assisted by a boosted decision tree discriminant known

as the Electron Charge ID Selector (ECIDS). For this analysis, all electrons are required to pass the ECIDS criterion.

### 4.3.2 Muons

Muons act as minimum-ionizing particles, leaving tracks in the MS or characteristics energy deposits in the calorimeter and can be reconstructed globally using information from the ID, MS and calorimeters. Five reconstruction strategies corresponding to five muon types [117] are utilized in ATLAS:

- Combined (CB): the primary ATLAS muon reconstruction method. Combined muons are first reconstructed using MS tracks then extrapolated to include ID tracks (outside-in strategy). A global combined track fit is performed on both MS and ID tracks.
- Inside-out combined (IO): complementary to CB reconstruction. IO muon tracks are extrapolated from ID to MS, then fitted with MS hits and calorimeter energy loss in a combined track fit.
- MS extrapolated (ME): ME muons are defined as muons with a MS track that cannot be matched to an ID track using CB reconstruction. ME muons allow extension of muon reconstruction acceptance to regions not covered by the ID ( $2.5 < |\eta| < 2.7$ )
- Segment-tagged (ST): ST muons are defined as a successfully matched ID track that satisfies tight angular matching criteria to at least one reconstructed MDT or CSC segment when extrapolated to the MS. MS reconstruction is used primarily when muons only crossed one layer of MS chambers.
- Calorimeter-tagged (CT): CT muons are defined as an ID track that can be matched to

energy deposits consistent with those of a minimum-ionizing particle when extrapolated through the calorimeter. CT reconstruction extends acceptance range to regions in the MS with sparse instrumentation ( $|\eta| < 0.1$ ) with a higher  $p_T$  threshold of 5 GeV, compared to the 2 GeV threshold used by other muon reconstruction algorithms due to large background contamination at the low  $p_T$  range of  $15 < p_T < 100$  GeV [118].

## Muon identification

Reconstructed muons are further filtered by identification criteria to select for high-quality prompt muons. Requirements include number of hits in the MS and ID, track fit properties and compatibility between measurements of the two systems. Three standard OPs (*Loose*, *Medium*, *Tight*) are defined to better match the needs of different physics analyses concerning prompt muon  $p_T$  resolution, identification efficiency and non-prompt muon rejection. The default identification OP for ATLAS physics and also the OP used in this analysis is *Medium*, which provides efficiency and purity suitable for a wide range of studies while minimizing systematic uncertainties [117].

## Muon isolation

Muons from heavy particle decays are often produced in an isolated manner compared to muons from semileptonic decays, and is therefore an important tool for background rejection in many physics analyses. Muon isolation strategies are similar to that of electron in section 4.3.1, with track-based and calorimeter-based isolation variables. Seven isolation OPs are defined using either or both types of isolation variables, balancing between prompt muon acceptance and non-prompt muon rejection. The full definition and description for the muon isolation OPs are detailed in Ref. [117].

## 4.4 Missing transverse momentum

Collisions at the LHC happen along the  $z$ -axis of the ATLAS coordination system between two particle beam of equal center-of-mass energy. By conservation of momentum, the sum of transverse momenta of outgoing particles should be zero. A discrepancy between measured momentum and zero would then suggest the presence of undetectable particles, which would consist of either SM neutrinos or some unknown BSM particles, making missing transverse momentum ( $E_T^{\text{miss}}$ ) an important observable to reconstruct.

Reconstructing  $E_T^{\text{miss}}$  utilizes information from fully reconstructed leptons, photons, jets and other matched track-vertex objects not associated with a prompt object (soft signals), defined with respect to the  $x(y)$ -axis as

$$E_{x(y)}^{\text{miss}} = - \sum_{i \in \{\text{hard objects}\}} p_{x(y),i} - \sum_{j \in \{\text{soft signals}\}} p_{x(y),j}, \quad (4.3)$$

where  $p_{x(y)}$  is the  $x(y)$ -component of  $p_T$  for each particle [119]. The following observables can then be defined:

$$\begin{aligned} \mathbf{E}_T^{\text{miss}} &= (E_x^{\text{miss}}, E_y^{\text{miss}}), \\ E_T^{\text{miss}} &= |\mathbf{E}_T^{\text{miss}}| = \sqrt{(E_x^{\text{miss}})^2 + (E_y^{\text{miss}})^2}, \\ \phi^{\text{miss}} &= \tan^{-1}(E_y^{\text{miss}}/E_x^{\text{miss}}), \end{aligned} \quad (4.4)$$

where  $E_T^{\text{miss}}$  represents the magnitude of the missing transverse energy vector  $\mathbf{E}_T^{\text{miss}}$ , and  $\phi^{\text{miss}}$  its direction in the transverse plane. The vectorial sum  $\mathbf{E}_T^{\text{miss}}$  can be broken down into

$$\mathbf{E}_T^{\text{miss}} = - \underbrace{\sum_{\text{selected electrons}} \mathbf{p}_T^e - \sum_{\text{selected muons}} \mathbf{p}_T^\mu - \sum_{\text{accepted photons}} \mathbf{p}_T^\gamma - \sum_{\text{accepted } \tau\text{-leptons}} \mathbf{p}_T^\tau}_{\text{hard term}} - \underbrace{\sum_{\text{accepted jets}} \mathbf{p}_T^{\text{jet}} - \sum_{\text{unused tracks}} \mathbf{p}_T^{\text{track}}}_{\text{soft term}}. \quad (4.5)$$

Two OPs are defined for  $E_T^{\text{miss}}$ , *Loose* and *Tight*, with selections on jet  $p_T$  and JVT criteria [120]. The *Tight* OP is used in this analysis; *Tight* reduces pile-up dependence of  $E_T^{\text{miss}}$  by removing the phase space region containing more pile-up than hard-scatter jets, at the expense of resolution and scale at low pile-up,

## 4.5 Overlap removal

Since different objects are reconstructed independently, it is possible for the same detector signals to be used to reconstruct multiple objects. An overlap removal strategy is implemented to resolve ambiguities; the overlap removal process for this analysis applies selections in Table 4.1 sequentially, from top to bottom.

Table 4.1: Overlap removal process for this analysis, applied sequentially from top to bottom.

Remove	Keep	Matching criteria
Electron	Electron	Shared ID track, $p_{T,1}^e < p_{T,2}^e$
Muon	Electron	Shared ID track, CT muon
Electron	Muon	Shared ID track
Jet	Electron	$\Delta R < 0.2$
Electron	Jet	$\Delta R < 0.4$
Jet	Muon	( $\Delta R < 0.2$ or ghost-associated) & $N_{\text{track}} < 3$
Muon	Jet	$\Delta R < \min(0.4, 0.04 + 10\text{GeV}/p_T^\mu)$

## 4.6 Object definition

Table 4.2 summarizes the selections on physics objects used in this analysis. Each selection comes with associated calibration scale factors (SFs) to account for discrepancies between data and MC simulation, and are applied multiplicatively to MC event weights.

Table 4.2: Summary of object selection criteria used in this analysis.  $\ell_0$  refers to the leading lepton in the event.

Selection	Electrons	Muons	Jets
$p_T$ [GeV]	$> 15$ $p_T(\ell_0) > 28$	$> 15$	$> 20$
$ \eta $	$1.52 \leq  \eta  < 2.47$ $< 1.37$	$< 2.5$	$< 2.5$
Identification	<i>TightLH</i> pass ECIDS ( $ee/e\mu$ )	<i>Medium</i>	NNJvt <i>FixedEffPt</i> ( $p_T < 60$ , $ \eta  < 2.4$ )
Isolation	<i>Tight_VarRad</i>	<i>PflowTight_VarRad</i>	
Track-vertex assoc.			
$ d_0^{\text{BL}}(\sigma) $	$< 5$	$< 3$	
$ \Delta z_0^{\text{BL}} \sin \theta $ [mm]	$< 0.5$	$< 0.5$	

# Chapter 5. Data & Simulated Samples

## 5.1 Data samples

Data samples used in this analysis were collected by the ATLAS detector during the Run 2 data-taking campaign between 2015-2018. The samples contain  $pp$  collisions at center-of-mass energy of  $\sqrt{s} = 13$  TeV with 25 ns bunch-spacing, which corresponds to an integrated luminosity of  $140 \text{ fb}^{-1}$  with an uncertainty of 0.83% [89]. The HLT trigger strategy is similar to that of previous  $t\bar{t}t\bar{t}$  observation analysis [44] and include single lepton and dilepton triggers. Calibration for di-muon and electron-muon triggers were not ready for the samples used in this analysis, and are therefore not included. Events are also required to contain at least one lepton matched to the corresponding object firing the trigger. Triggers utilized in this analysis are summarized in Table 5.1, with efficiency close to 100% when used together.

## 5.2 Monte Carlo samples

Monte Carlo simulated samples are used to estimate signal acceptance before unblinding, profile the physics background for the analysis and to study object optimizations. Simulated samples for this analysis use are generated from ATLAS generalized MC20a/d/e samples for Run 2, using full detector simulation (FS) and fast simulation (AF3) to simulate detector response. MC samples used and simulation processes are summarized in Table 5.2.

Table 5.1: Summary of all HLT triggers used in this analysis. Events are required to pass at least one trigger.

Trigger	Data period			
	2015	2016	2017	2018
Single electron triggers				
HLT_e24_lhmedium_L1EM20VH	✓	-	-	-
HLT_e60_lhmedium	✓	-	-	-
HLT_e120_lhloose	✓	-	-	-
HLT_e26_lhtight_nod0_ivarloose	-	✓	✓	✓
HLT_e60_lhmedium_nod0	-	✓	✓	✓
HLT_e140_lhloose_nod0	-	✓	✓	✓
Di-electron triggers				
HLT_2e12_lhloose_L12EM10VH	✓	-	-	-
HLT_2e17_lhvloose_nod0	-	✓	-	-
HLT_2e24_lhvloose_nod0	-	-	✓	✓
HLT_2e17_lhvloose_nod0_L12EM15VHI	-	-	-	✓
Single muon trigger				
HLT_mu20_iloose_L1MU15	✓	-	-	-
HLT_mu40	✓	-	-	-
HLT_mu26_ivarmedium	-	✓	✓	✓
HLT_mu50	-	✓	✓	✓

### 5.2.1 $t\bar{t}Z'$ signal samples

Signal  $t\bar{t}Z'$  samples were generated based on the simplified topophilic resonance model in section 2.2.1. Six  $Z'$  mass points were utilized for the generation of the signal sample: 1000, 1250, 1500, 2000, 2500 and 3000 GeV. The top- $Z'$  coupling  $c_t$  is chosen to be 1 for a narrow resonance peak, and the chirality angle  $\theta$  is chosen to be  $\pi/4$  to suppress loop production of  $Z'$ . The samples were then generated with `MADGRAPH5_AMC@NLO v.3.5.0` [121] at LO with the `NNPDF3.1LO` [122] PDF set interfaced with `PYTHIA8` [123] using A14 tune and `NNPDF2.3lo` PDF set for parton showering and hadronization. The resonance width is calculated to be 4% for  $c_t = 1$ .

Table 5.2: Summary of all Monte-Carlo samples used in this analysis.  $V$  refers to an EW ( $W^\pm/Z/\gamma^*$ ) or Higgs boson. Matrix element (ME) order refers to the order in QCD of the perturbative calculation. Tune refers to the underlying-event tune of the parton shower (PS) generator.

Process	ME Generator	ME Order	ME PDF	PS	Tune	Sim.
<b>Signals</b>						
$t\bar{t}Z'$	MADGRAPH5_AMC@NLO LO		NNPDF3.1LO		PYTHIA8 A14	FS
<b><math>t\bar{t}t\bar{t}</math> and <math>t\bar{t}\bar{t}</math></b>						
$t\bar{t}t\bar{t}$	MADGRAPH5_AMC@NLO NLO		NNPDF3.0nlo		PYTHIA8 A14	AF3
	MADGRAPH5_AMC@NLO NLO		MMHT2014 LO		HERWIG7 H7-UE-MMHT	AF3
	SHERPA	NLO	NNPDF3.0nnlo		HERWIG7 SHERPA	FS
$t\bar{t}\bar{t}$	MADGRAPH5_AMC@NLO LO		NNPDF2.3lo		PYTHIA8 A14	AF3
<b><math>t\bar{t}V</math></b>						
$t\bar{t}H$	POWHEGBOX v2	NLO	NNPDF3.0nlo		PYTHIA8 A14	FS
	POWHEGBOX v2	NLO	NNPDF3.0nlo		HERWIG7 H7.2-Default	FS
$t\bar{t}(Z/\gamma^*)$	MADGRAPH5_AMC@NLO NLO		NNPDF3.0nlo		PYTHIA8 A14	FS
	SHERPA	NLO	NNPDF3.0nnlo		SHERPA SHERPA	FS
$t\bar{t}W$	SHERPA	NLO	NNPDF3.0nnlo		SHERPA SHERPA	FS
	SHERPA	LO	NNPDF3.0nnlo		SHERPA SHERPA	FS
<b><math>t\bar{t}</math> and Single-Top</b>						
$t\bar{t}$	POWHEGBOX v2	NLO	NNPDF3.0nlo		PYTHIA8 A14	FS
$tW$	POWHEGBOX v2	NLO	NNPDF3.0nlo		PYTHIA8 A14	FS
$t(q)b$	POWHEGBOX v2	NLO	NNPDF3.0nlo (s)		PYTHIA8 A14	FS
			NNPDF3.0nlo 4f (t)			FS
$tWZ$	MADGRAPH5_AMC@NLO NLO		NNPDF3.0nlo		PYTHIA8 A14	FS
$tZ$	MADGRAPH5_AMC@NLO LO		NNPDF3.0nlo 4f		PYTHIA8 A14	FS
<b><math>t\bar{t}VV</math></b>						
$t\bar{t}WW$	MADGRAPH5_AMC@NLO LO		NNPDF3.0nlo		PYTHIA8 A14	FS
$t\bar{t}WZ$	MADGRAPH	LO	NNPDF3.0nlo		PYTHIA8 A14	AF3
$t\bar{t}HH$	MADGRAPH	LO	NNPDF3.0nlo		PYTHIA8 A14	AF3
$t\bar{t}WH$	MADGRAPH	LO	NNPDF3.0nlo		PYTHIA8 A14	AF3
$t\bar{t}ZZ$	MADGRAPH	LO	NNPDF3.0nlo		PYTHIA8 A14	AF3
<b><math>V(VV)+\text{jets}</math> and <math>VH</math></b>						
$V+\text{jets}$	SHERPA	NLO	NNPDF3.0nnlo		SHERPA SHERPA	FS
$VV+\text{jets}$	SHERPA	NLO	NNPDF3.0nnlo		SHERPA SHERPA	FS
		LO ( $gg \rightarrow VV$ )				FS
$VVV+\text{jets}$	SHERPA	NLO	NNPDF3.0nnlo		SHERPA SHERPA	FS
$VH$	POWHEGBOX v2	NLO	NNPDF3.0aznlo		PYTHIA8 A14	FS

### 5.2.2 Background samples

#### SM $t\bar{t}t\bar{t}$ background

The nominal SM  $t\bar{t}t\bar{t}$  sample was generated with `MADGRAPH5_AMC@NLO` [121] at NLO in QCD with the `NNPDF3.0nlo` [122] PDF set and interfaced with `PYTHIA8.230` [123] using A14 tune [124]. Decays for top quarks are simulated at LO with `MADSPIN` [125, 126] to preserve spin information, while decays for  $b$ - and  $c$ -hadrons are simulated with `EVTGEN v1.6.0` [127]. The renormalization and factorization scales  $\mu_R$  and  $\mu_F$  are set to  $1/4\sqrt{m^2 + p_T^2}$ , which represents the sum of transverse mass of all particles generated from the ME calculation [128]. The ATLAS detector response was simulated with AF3. Additional auxiliary  $t\bar{t}t\bar{t}$  samples are also generated to evaluate the impact of generator and PS uncertainties as shown in 5.2.

#### $t\bar{t}W$ background

Nominal  $t\bar{t}W$  sample was generated using `SHERPA v2.2.10` [129] at NLO in QCD with the `NNPDF3.0nnlo` [122] PDF with up to one extra parton at NLO and two at LO, which are matched and merged with the `SHERPA` PS based on Catani-Seymour dipole factorization [130] using the `MEPS@NLO` prescription [131–134] and a merging scale of 30 GeV. Higher-order ME corrections are provided in QCD by the `OpenLoops 2` library [135–137] and in EW from  $\mathcal{O}(\alpha^3) + \mathcal{O}(\alpha_S^2\alpha^2)$  (LO3 & NLO2) via two sets of internal event weights. An alternative sample with only EW corrections at LO from  $\mathcal{O}(\alpha_S\alpha^3)$  (NLO3) diagrams were also simulated with the same settings.

## $t\bar{t}(Z/\gamma^*)$ background

The nominal  $t\bar{t}(Z/\gamma^*)$  samples were generated separately for different ranges of dilepton invariant mass  $m_{\ell\ell}$  to account for on-shell and off-shell  $Z/\gamma^*$  production. Sample for  $m_{\ell\ell}$  between 1 and 5 GeV was produced using MADGRAPH5\_AMC@NLO [121] at NLO with the NNPDF3.0nlo [122] PDF set, interfaced with PYTHIA8.230 [123] using A14 tune [124] and NNPDF2.3l0 PDF set. Sample for  $m_{\ell\ell} < 5$  GeV was produced with SHERPA v2.2.10 [129] at NLO using NNPDF3.0nnlo PDF set. To account for generator uncertainty, an alternative  $m_{\ell\ell} > 5$  GeV sample was generated with identical settings to the low  $m_{\ell\ell}$  sample. The ATLAS detector response was simulated with full detector simulation (FS).

## $t\bar{t}H$ background

Generation of  $t\bar{t}H$  background was done using PowHEGBox [138–141] at NLO in QCD with the NNPDF3.0nlo PDF [122] set. The nominal sample is interfaced with PYTHIA8.230 [123] using the A14 tune [124] and the NNPDF2.3l0 [142] PDF set. Detector response is simulated using FS. An alternative  $t\bar{t}H$  sample generated similarly, but instead interfaced with HERWIG7.2.3 [143, 144] to study the impact of parton shower and hadronization model. Detector response for the alternative sample is simulated using AF3.

## $t\bar{t}t$ background

The  $t\bar{t}t$  sample is generated using MADGRAPH5\_AMC@NLO [121] at LO in QCD, interfaced with PYTHIA8 [123] using the A14 tune [124]. The sample is produced in the five-flavor scheme [145] to prevent LO interference with  $t\bar{t}t\bar{t}$ .

## **$t\bar{t}$ background**

The  $t\bar{t}$  sample is modeled with PowhegBox [138–141] at NLO in QCD with the NNPDF3.0nlo [122] PDF set and the  $h_{\text{damp}}$  parameter set to  $1.5m_{\text{top}}$  [146]. Events are interfaced with PYTHIA8.230 [123] using the A14 tune [124] and the NNPDF2.3lō [142] PDF set.

## **Single-top ( $tW$ & $t(q)b$ ) background**

Single-top  $tW$ -associated production is modeled using the PowhegBox generator [138–141] at NLO in QCD in the five-flavor scheme [145] with the NNPDF3.0nlo [122] PDF set. Interference with  $t\bar{t}$  production [146] is handled using the diagram removal scheme [147]. Single-top  $t(q)b$  production is modeled using the PowhegBox generator at NLO in QCD with the s-channel production modeled in the five-flavor scheme with the NNPDF3.0nlo PDF set, while the t-channel production is modeled in the four-flavor scheme with the NNPDF3.0nlo 4f [122] PDF set. The  $t\bar{t}WW$  contributions are normalized to NLO theoretical cross section. All single-top samples are interfaced with PYTHIA8.230 [123] using the A14 tune [124] and the NNPDF2.3lō [142] PDF set.

## **$tWZ$ +jets background**

The  $tWZ$  sample is generated using MADGRAPH5\_AMC@NLO [121] at NLO in QCD with the NNPDF3.0nlo [122] PDF set, interfaced with PYTHIA8.212 [123] using the A14 tune [124] and the NNPDF2.3lō [142] PDF set.

## **$tZ$ & $t\bar{t}VV$ background**

Production of  $tZ$  is modeled using MADGRAPH5\_AMC@NLO [121] at NLO in QCD with scale of  $H_T/6$  and the NNPDF3.0nlo 4f [122] PDF set. Production of  $t\bar{t}WW$  is modeled

using `MADGRAPH5_AMC@NLO` [121] at LO, while production of  $t\bar{t}WZ$ ,  $t\bar{t}HH$ ,  $t\bar{t}WH$  and  $t\bar{t}ZZ$  are modeled using `MADGRAPH` at LO. All  $t\bar{t}VV$  samples use the `NNPDF3.0nlo` [122] PDF set, and all samples in this section are interfaced with `PYTHIA8` [123] using the A14 tune [124].

### **Single boson ( $V$ ) +jets background**

Production of  $V$ +jets is modeled with `SHERPA v2.2.10` [129] using NLO ME for up to two jets and LO ME for up to four jets, with the `NNPDF3.0nlo` [122] PDF set. Matrix elements are calculated with the Comix [148] and OpenLoops libraries [135, 136] and matched with the `SHERPA` PS based on Catani-Seymour dipole factorization [130] using the MEPS@NLO prescription [131–134]. The sample is normalized to the NNLO [149] theoretical cross section.

### **Diboson ( $VV$ ) +jets background**

Diboson samples are simulated with `SHERPA v2.2.14` [129] with the `NNPDF3.0nlo` [122] PDF set. Fully leptonic and semileptonic final states are generated using NLO ME for up to one extra parton and LO ME for up to three extra parton emissions. Loop-induced processes are generated using LO ME for up to one extra parton. Matrix elements are matched and merged with the `SHERPA` PS based on Catani-Seymour dipole factorization [130] using the MEPS@NLO prescription [131–134]. Virtual QCD ME corrections are provided by the OpenLoops library [135, 136].

### **Triboson ( $VVV$ ) +jets background**

The triboson sample is modeled with `SHERPA v2.2.10` [129] using factorized gauge boson decays. Matrix elements for the inclusive process at NLO and up to two extra partons at

LO are matched and merged with the SHERPA PS based on Catani-Seymour dipole factorization [130] using the MEPS@NLO prescription [131–134]. Virtual QCD ME corrections are provided by the OpenLoops library [135, 136].

### ***VH* background**

Generation of  $WH$  and  $ZH$  samples is performed using PowhegBox [138–141] at NLO with the NNPDF3.0aznlo [122] PDF set, interfaced with PYTHIA8.230 [123] using the A14 tune [124] and the NNPDF2.3lo [142] PDF set.

# Chapter 6. Analysis Strategy

## 6.1 Event selection

Events for the analysis first are preselected following a list of criteria to optimize for event quality and background rejection. The following criteria are applied sequentially from top to bottom along with cleaning and veto cuts

1. **Good Run List (GRL)**: data events must be part of a predefined list of suitable runs and luminosity blocks [150].
2. **Primary vertex**: events must have at least one reconstructed vertex matched to 2 or more associated tracks with  $p_T > 500$  MeV.
3. **Trigger**: events must be selected by at least one trigger in Table 5.1.
4. **Kinematic selection**: events must have exactly two *Tight* leptons with the same electric charge, or at least three *Tight* leptons of any charge. The leading lepton must have  $p_T > 28$  GeV, and all leptons must satisfy  $p_T > 15$  GeV.

Events are separated into two channels based on the number of leptons: same-sign di-lepton (SS2L) for events with exactly two leptons of the same charge, or multilepton (ML) for events with three or more leptons. The channels are further separated into regions defined in section 6.2 to prepare for analysis.

Additional selections are applied based on the lepton flavors present. In the SS2L channel, if both leptons are electrons, the invariant mass  $m_{ll}$  must satisfy  $m_{ll} < 81$  GeV and  $m_{ll} > 101$  GeV to suppress background involving  $Z$ -bosons. In the ML channel, the same criteria must be satisfied for every opposite-sign same-flavor pair of leptons in an event.

### 6.1.1 Event categorization

Simulated events are categorized using truth information of leptons ( $e/\mu$ ) and their originating MC particle (mother-particle). Each lepton can be classified as either prompt or non-prompt, with non-prompt leptons further categorized for background estimation purposes. If an event contains only prompt leptons, the event is classified as its corresponding process. If the event contains one non-prompt lepton, the event is classified as the corresponding type of the non-prompt lepton. If the event contains more than one non-prompt lepton, the event is classified as other.

- **Prompt:** if the lepton originates from  $W/Z/H$  boson decays, or from a mother-particle created by a final state photon.
- **Non-prompt:**
  - **Charge-flip (e only):** if the reconstructed charge of the lepton differs from that of the first mother-particle.
  - **Material conversion (e only):** if the lepton originated from a photon conversion and the mother-particle is an isolated prompt photon, non-isolated final state photon, or heavy boson.
  - **$\gamma^*$ -conversion (e only):** if the lepton originated from a photon conversion and the mother-particle is a background electron.
  - **Heavy flavor decay:** if the lepton originated from a  $b$ - or  $c$ -hadron.
  - **Fake:** if the lepton originated from a light- or  $s$ -hadron, or if the truth type of the lepton is hadron.
  - **Other:** any lepton that does not belong to one of the above categories.

## 6.2 Analysis regions

Events are selected and categorized into analysis regions belonging to one of two types: control regions (CRs) enriched in background events, and signal regions (SRs) enriched in signal events. This allows for the examination and control of backgrounds and systematic uncertainties, as well as study of signal sensitivities. The signal is then extracted from the SRs with a profile LH fit using all regions. The full selection criteria for each region are summarized in Table 6.1. The post-fit background compositions in different CRs and SR sub-regions are shown in Figure 6.1.

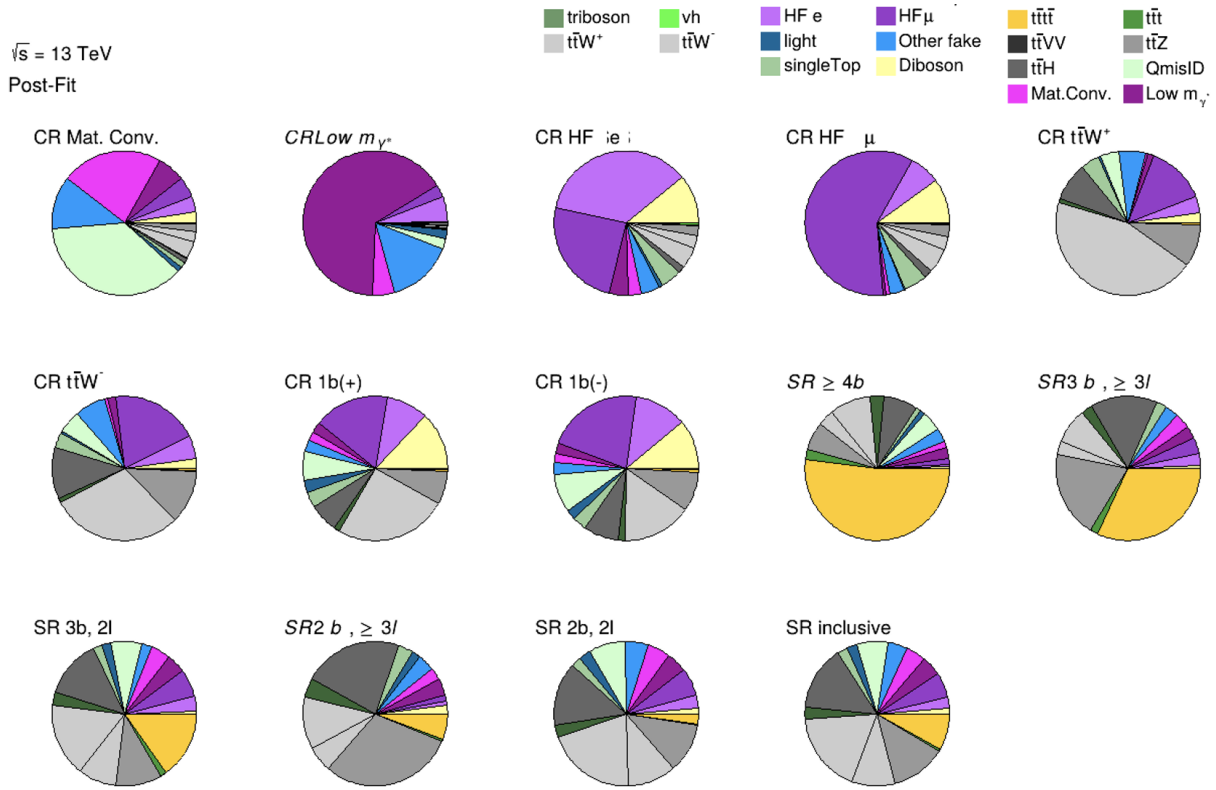


Figure 6.1: Post-fit background composition in each analysis region and sub-region. The fit was performed using ideal pseudo-datasets (Asimov data) in the SR.

Table 6.1: Definitions of signal, control and validation regions (VR) used in this analysis.  $N_{\text{jets}}$  and  $N_b$  refers to the number of jets and number of  $b$ -tagged jets respectively.  $\ell_1$  refers to the leading lepton,  $\ell_2$  refers to the subleading lepton and so on.  $H_T$  refers to the  $p_T$  scalar sum of all leptons and jets in the event.  $m_{\ell\ell}$  refers to the dilepton invariant mass, which must not coincide with the  $Z$ -boson mass range of 81-101 GeV for SS2L+3L events.

Region	Channel	$N_{\text{jets}}$	$N_b$	Other selections	Fitted variable
CR Low $m_{\gamma^*}$	SS $e\ell$	[4, 6)	$\geq 1$	$\ell_1/\ell_2$ is from virtual photon decay $\ell_1 + \ell_2$ not from material conversion	event yield
CR Mat. Conv.	SS $e\ell$	[4, 6)	$\geq 1$	$\ell_1/\ell_2$ is from material conversion $\ell_1 + \ell_2$ not conversion candidates	event yield
CR HF $\mu$	$\ell\mu\mu$	$\geq 1$	1	$100 < H_T < 300$ GeV $E_T^{\text{miss}} > 35$ GeV total charge = $\pm 1$	$p_T(\ell_3)$
CR HF $e$	$e\ell\ell$	$\geq 1$	1	$\ell_1 + \ell_2$ not conversion candidates $100 < H_T < 275$ GeV $E_T^{\text{miss}} > 35$ GeV total charge = $\pm 1$	$p_T(\ell_3)$
CR $t\bar{t}W^+$	SS $\ell\mu$	$\geq 4$	$\geq 2$	$ \eta(e)  < 1.5$ for $N_b = 2$ : $H_T < 500$ GeV or $N_{\text{jets}} < 6$ for $N_b \geq 3$ : $H_T < 500$ GeV total charge > 0	$N_{\text{jets}}$
CR $t\bar{t}W^-$	SS $\ell\mu$	$\geq 4$	$\geq 2$	$ \eta(e)  < 1.5$ for $N_b = 2$ : $H_T < 500$ GeV or $N_{\text{jets}} < 6$ for $N_b \geq 3$ : $H_T < 500$ GeV total charge < 0	$N_{\text{jets}}$
CR 1b(+)	SS2L+3L	$\geq 4$	1	$\ell_1 + \ell_2$ not from material conversion $H_T > 500$ GeV total charge > 0	$N_{\text{jets}}$
CR 1b(-)	SS2L+3L	$\geq 4$	1	$\ell_1 + \ell_2$ not from material conversion $H_T > 500$ GeV total charge < 0	$N_{\text{jets}}$
VR $t\bar{t}Z$	3L $\ell^\pm\ell^\mp$	$\geq 4$	$\geq 2$	$m_{\ell\ell} \in [81, 101]$ GeV	$N_{\text{jets}}, m_{\ell\ell}$
VR $t\bar{t}W +1b$	SS2L+3L			CR $t\bar{t}W^\pm$    CR 1b( $\pm$ )	$N_{\text{jets}}$
VR $t\bar{t}W +1b+SR$	SS2L+3L			CR $t\bar{t}W^\pm$    CR 1b( $\pm$ )    SR	$N_{\text{jets}}$
SR	SS2L+3L	$\geq 6$	$\geq 2$	$H_T > 500$ GeV $m_{\ell\ell} \notin [81, 101]$ GeV	$H_T$

### 6.2.1 Signal regions

All events selected for the SR must satisfy the following criteria:

- Contains 6 or more jets, with at least 2 jets  $b$ -tagged at the 85% OP.
- Scalar sum of the transverse momenta of all leptons and jets  $H_T > 500$  GeV.
- Dilepton invariant mass  $m_{\ell\ell}$  does not coincide with the  $Z$ -boson mass range of 81 – 101 GeV

The SR is further divided into sub-regions by the number of  $b$ -tagged jets and leptons present to study signal behavior and sensitivity with respect to the selection variables.

Table 6.2: Definitions of SR sub-regions. Events are sorted into different sub-regions based on the number of  $b$ -tagged jets and leptons present.

Sub-region	Selection criteria	
	$b$ -jets	leptons
SR 2b2l	$N_b = 2$	$N_l = 2$
SR 2b3l4l	$N_b = 2$	$N_l \geq 3$
SR 3b2l	$N_b = 3$	$N_l = 2$
SR 3b3l4l	$N_b = 3$	$N_l \geq 3$
SR 4b	$N_b \geq 4$	

### Signal extraction

Signal extraction in the SR is performed via a binned profile likelihood (LH) fit as described in section 8.1 using  $H_T$  as the discriminant observable. The discriminant observable for a LH fit serves as the set of observed data upon which the LH function is constructed. Ideally, the chosen observable shows significant separation between the functional forms of the signal and background distributions, allowing for effective separation of the two. Figure 6.2 shows several pre-fit kinematic distributions in the inclusive SR. From empirical

optimization studies,  $H_T$  possesses good discriminating power compared to other observables constructed using event-level information.

### 6.2.2 Control regions

Control regions are defined for each background to be enriched in the targeted process, in order to maximize the background’s purity and minimize contamination from other sources within the region. This helps to constrain and reduce correlation between background normalization factors in the final fit. Fit variables and selection criteria are determined via optimization studies performed on CRs that aimed to achieve the largest discriminating power possible between the target background and other event types.

#### $t\bar{t}W$ background CRs

Theoretical modeling for  $t\bar{t}W + \text{jets}$  background in the phase space of this analysis suffers from large uncertainties, especially at high jet multiplicities [151]. A data-driven method was employed in a similar manner to the SM  $t\bar{t}t\bar{t}$  observation analysis [44] to mitigate this effect and is described in further details in section 6.3.3. The method necessitates the definition of two groups of dedicated CRs to estimate the flavor composition and normalization of  $t\bar{t}W + \text{jets}$  background: CR  $t\bar{t}W + \text{jets}$  to constrain flavor composition, and CR 1b to constrain the jet multiplicity spectrum. These are further split into CR  $t\bar{t}W^\pm$  and CR 1b( $\pm$ ) to account for the pronounced asymmetry in  $t\bar{t}W$  production from  $pp$  collisions at the LHC. The cross section of  $t\bar{t}W^+$  production is approximately twice that of  $t\bar{t}W^-$  [152] due to the combination of the main  $W^+$  emission process being  $u \rightarrow dW^+$  and the ratio of two  $u$ -quarks to one  $d$ -quark in the proton.

Events in CR  $t\bar{t}W^\pm$  are required to contain at least two  $b$ -tagged jets similar to the SR

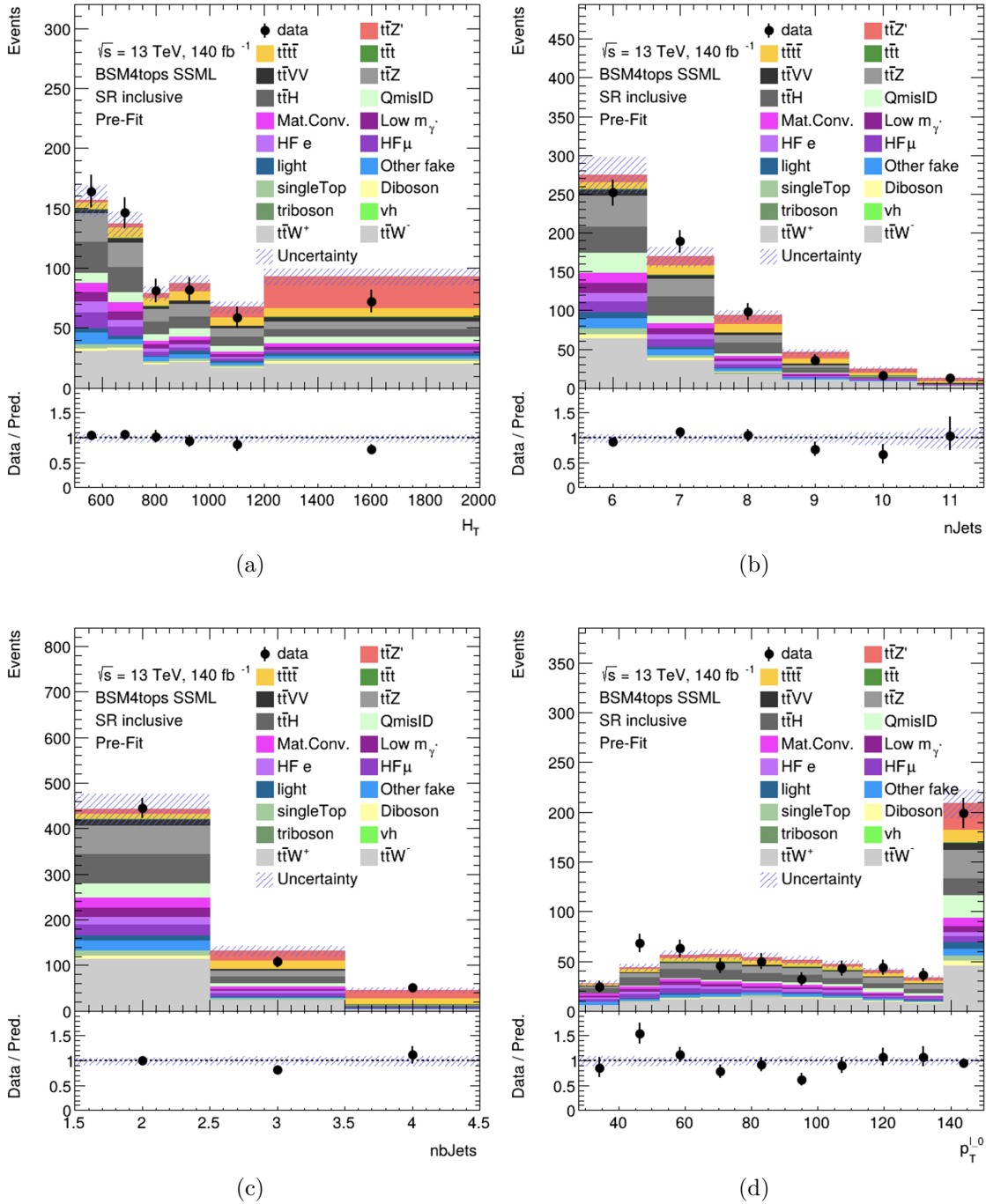


Figure 6.2: Pre-fit kinematic distributions and event compositions in the inclusive SR for (a)  $H_T$  i.e. scalar sum of  $p_T$  of all objects in the event, (b) jet multiplicity, (c)  $b$ -jet multiplicity, (d) leading lepton  $p_T$ . The shaded band represents the uncertainty in the total distribution. The first and last bins of each distribution contain underflow and overflow events respectively.

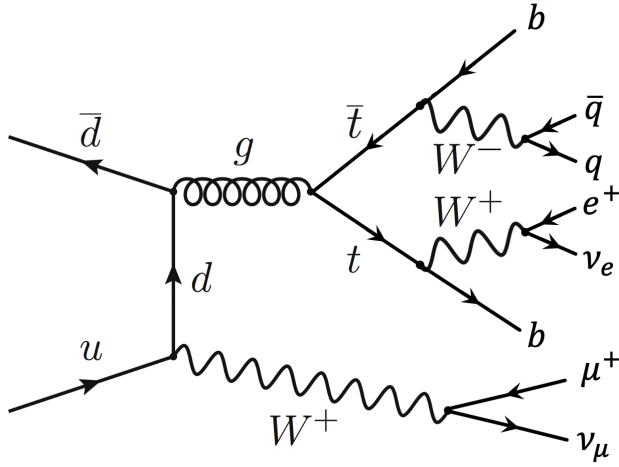


Figure 6.3: Feynman diagram for one possible  $t\bar{t}W$  decay process with similar SS2L lepton signature to the  $t\bar{t}Z'$  signal. Usually only two  $b$ -jets are present due to CKM suppression of  $b$ -quark production from  $W$ -boson decays; this is enough to allow  $t\bar{t}W$  decays to enter and contaminate the SR.

to determine the  $t\bar{t}W$  normalization within an SR-related phase space. Orthogonality with SR is ensured by requiring  $H_T < 500$  GeV or  $N_{\text{jets}} < 6$  when  $N_b = 2$ , and  $H_T < 500$  GeV when  $N_b \geq 3$ . Events in CR 1b( $\pm$ ) are required to have  $H_T > 500$  GeV and at least four jets to encompass events with high  $N_{\text{jets}}$ , which can be used to determine the  $t\bar{t}W$  jet multiplicity spectrum for fitting  $a_{0,1}$ . The selection criteria also include exactly one  $b$ -tagged jet to maintain orthogonality with the SR.

### Fake/non-prompt background CRs

Selection for fake/non-prompt CRs are determined using the `DFCommonAddAmbiguity` (`DFCAA`) variable for reconstructed leptons.

Four CRs are defined for the three main types of fake/non-prompt backgrounds in the analysis - virtual photon ( $\gamma^*$ ) conversion, photon conversion in detector material (Mat. Conv.) and heavy flavor decays (HF). The full selection criteria for fake/non-prompt CRs are shown in Table 6.1.

Table 6.3: List of possible assigned values for DFCAA.

DFCAA	Description
-1	No 2nd track found
0	2nd track found, no conversion found
1	Virtual photon conversion candidate
2	Material conversion candidate

- **Low  $m_{\gamma}^*$ :** events with an  $e^+e^-$  pair produced from a virtual photon.

Events are selected if there are two same-sign leptons with at least one electron reconstructed as an internal conversion candidate, and neither reconstructed as a material conversion candidate.

- **Mat. Conv.:** events with an electron originating from photon conversion within the detector material.

Events are selected if there are two same-sign leptons with at least one electron reconstructed as a material conversion candidate.

- **HF  $e(\mu)$ :** events with a reconstructed non-prompt lepton from semi-leptonic decays of  $b$ - and  $c$ -hadrons (heavy flavor decays).

Events are selected if there are three leptons with at least two electrons (muons), with no lepton reconstructed as a conversion candidate.

### 6.3 Background estimation

Background in this analysis consist of SM processes that can result in a signal signature similar to a  $t\bar{t}t\bar{t}$  SSML final state and can be divided into two types, reducible and irreducible. Reducible background consists of processes that do not result in a SSML final state physically, but are reconstructed as such due to detector and reconstruction effects. The main types

of reducible background considered are charge misidentification (QmisID) and fake/non-prompt leptons. Fake/non-prompt lepton backgrounds contaminate the SR when a non-prompt lepton is reconstructed as a prompt lepton in a  $t\bar{t}$ -associated process, leading to a similar final state to that of SSML  $t\bar{t}t\bar{t}$ . These backgrounds are estimated using the template fitting method described in subsection 6.3.1, where MC simulations are normalized to their theoretical SM cross section via floating normalization factors (NFs) constrained by the corresponding CRs. Lepton charge misidentification background contaminates the SR similarly when one of the two leptons in a  $t\bar{t}$ -associated process with two opposite-sign leptons is misidentified, producing a SS2L  $t\bar{t}t\bar{t}$  final state. Charge misidentification background is estimated using a data-driven method described in section 6.3.2 along with ECIDS described in section 4.3.1.

Irreducible background consists of SM processes that result in SSML final states with all leptons being prompt. The dominating background in the SR are SM  $t\bar{t}t\bar{t}$ ,  $t\bar{t}W$ ,  $t\bar{t}Z$ , and  $t\bar{t}H$  production with smaller contributions from  $VV$ ,  $VVV$ ,  $VH$  and rarer processes like  $t\bar{t}VV$ ,  $tWZ$ ,  $tZq$  and  $t\bar{t}t$ . Most irreducible backgrounds are estimated using template fitting method, with the exception of  $t\bar{t}W + \text{jets}$  background. The  $t\bar{t}W + \text{jets}$  background is instead given four dedicated CRs, and estimated using a data-driven method with a fitted function parameterized in  $N_{\text{jets}}$ . All CRs and SR are included in the final profile LH fit to data.

### 6.3.1 Template fitting for fake/non-prompt estimation

The template fitting method is a semi-data-driven approach [151] that estimates fake/non-prompt background distributions by fitting the MC kinematic profile of background processes arising from fake/non-prompt leptons to data. The four main sources of fake/non-prompt leptons are generated from  $t\bar{t} + \text{jets}$  samples and are constrained by four CRs enriched with

the corresponding backgrounds. Each of the aforementioned background is assigned a free-floating NF resulting in  $\text{NF}_{\text{HF } e}$ ,  $\text{NF}_{\text{HF } \mu}$ ,  $\text{NF}_{\text{Mat. Conv.}}$  and  $\text{NF}_{\text{Low } m_{\gamma^*}}$ . The NFs are fitted simultaneously with the signal within their constraining CRs.

### 6.3.2 Charge misidentification data-driven estimation

The  $ee$  and  $e\mu$  channels in the SS2L  $t\bar{t}t\bar{t}$  region are contaminated with opposite-sign (OS) dilepton  $t\bar{t}$ -associated events where one electron has its charge misidentified. Charge misidentification (QmisID) largely affects electrons due to muons' precise curvature information using ID and MS measurements and low bremsstrahlung rate. The charge flip rates are significant at higher  $p_T$  and varies with  $|\eta|$  which is proportional to the amount of detector material the electron interacted with.

The charge flip probability  $\epsilon$  is estimated in this analysis with a data-driven method [153] using a sample of  $Z \rightarrow e^+e^-$  events with additional constraints on the invariant mass  $m_{ee}$  to be within 10 GeV of the  $Z$ -boson mass. The  $Z$ -boson mass window is defined to be within  $4\sigma$  to include most events within the peak, and is determined by fitting the  $m_{ee}$  spectrum of the two leading electrons to a Breit-Wigner function, resulting in a range of [65.57, 113.49] for SS events and [71.81, 109.89] for OS events. Background contamination near the peak is assumed to be uniform and subtracted using a sideband method. Since the  $Z$ -boson decay products consist of a pair of opposite-sign electrons, all same-sign electron pairs are considered affected by charge misidentification.

Let  $N_{ij}^{\text{SS}}$  be the number of events with SS electrons with the leading electron in the  $i^{\text{th}}$  2D bin in  $(p_T, |\eta|)$  and the sub-leading electron in the  $j^{\text{th}}$  bin. Assuming the QmisID probabilities of electrons in an event are uncorrelated,  $N_{ij}^{\text{SS}}$  can be estimated as

$$N_{ij}^{\text{SS}} = N_{ij}^{\text{tot}} [\epsilon_i(1 - \epsilon_j) + \epsilon_j(1 - \epsilon_i)], \quad (6.1)$$

where  $N_{ij}^{\text{tot}}$  is the total number of events in the  $i^{\text{th}}$  and  $j^{\text{th}}$  bin regardless of charge, and  $\epsilon_{i(j)}$  is the QmisID rate in the  $i^{\text{th}}(j^{\text{th}})$  bin. Assuming  $N_{ij}^{\text{SS}}$  follows a Poisson distribution around the expectation value  $\bar{N}_{ij}^{\text{SS}}$ , the  $(i, n)^{\text{th}}$  rate  $\epsilon$  can be estimated by minimizing a negative-LLH function parameterized in  $p_T$  and  $|\eta|$ ,

$$\begin{aligned} -\ln(\mathcal{L}(\epsilon | N_{\text{SS}})) &= -\ln \prod_{ij} \frac{(N_{ij}^{\text{tot}})^{N_{ij}^{\text{SS}}} \cdot e^{N_{ij}^{\text{tot}}}}{N_{ij}^{\text{SS}}!} \\ &= -\sum_{ij} \left[ N_{ij}^{\text{SS}} \ln(N_{ij}^{\text{tot}}(\epsilon_i(1 - \epsilon_j) + \epsilon_j(1 - \epsilon_i))) - N_{ij}^{\text{tot}}(\epsilon_i(1 - \epsilon_j) + \epsilon_j(1 - \epsilon_i)) \right]. \end{aligned} \quad (6.2)$$

The QmisID rates are then calculated separately for SR and CRs with different electron definitions i.e. CR Low  $m_{\gamma^*}$ , CR Mat. Conv., CR  $t\bar{t}W^\pm$ , using events from data after applying region-specific lepton selections and ECIDS. The events are required to satisfy SS2L kinematic selections but contains OS electrons. The following weight is applied to OS events to correct for misidentified SS events within the region,

$$w = \frac{\epsilon_i + \epsilon_j - 2\epsilon_i\epsilon_j}{1 - \epsilon_i - \epsilon_j + 2\epsilon_i\epsilon_j}. \quad (6.3)$$

The QmisID rates calculated for SR and CR  $t\bar{t}W$  are shown in Figure 6.4

The QmisID rates obtained after applying  $w$  contain a dependency on jet multiplicity and are underestimated at higher  $N_{\text{jets}}$ . This dependency affect the SR which require events with  $\geq 6$  jets, and is corrected by applying a correction factor  $\text{SF}_{i,n} = \epsilon_{i,n}/\epsilon_{i,N}$  where  $N$  is

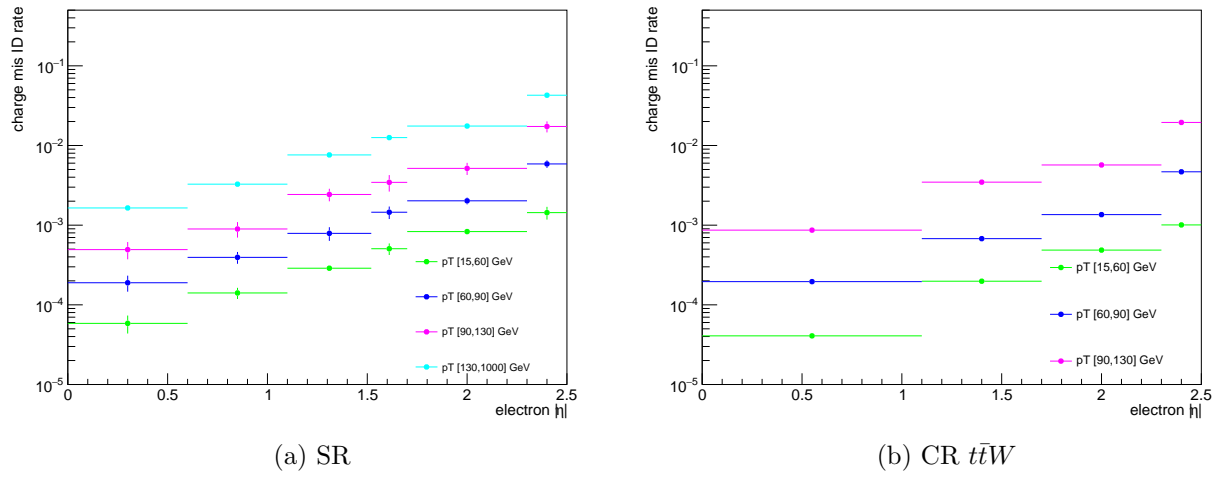


Figure 6.4: Charge flip rate calculated for SR and CR  $t\bar{t}W$  in bins of  $|\eta|$  and  $p_T$ .

the inclusive bin containing all  $N_{\text{jets}}$  and  $\epsilon_{i,n}$  is the QmisID rate obtained from Equation 6.2 in the  $(i, n)^{\text{th}}$  2D bin in  $(p_T, N_{\text{jets}})$ . Jet multiplicity and consequently the obtained SFs are assumed to be independent of  $|\eta|$ .

### 6.3.3 $t\bar{t}W$ background data-driven estimation

Previously, the  $t\bar{t}W$  background in  $t\bar{t}t\bar{t}$  final state analyses was handled by assigning large ad-hoc systematic uncertainties to  $t\bar{t}W$  events with 7 or more jets [47]. A semi-data-driven method [154] was shown to be effective in the SM  $t\bar{t}t\bar{t}$  observation analysis [44] by improving  $t\bar{t}W$  modeling, especially in the showering step and switching  $t\bar{t}W$  systematic uncertainties from predominantly modeling to statistical.

The data-driven method applies correction factors obtained from a fitted function parameterized in  $N_{\text{jets}}$  to  $t\bar{t}W$  MC kinematic distributions. The QCD scaling patterns [155] can be represented by ratio of successive exclusive jet cross-sections

$$R_{(n+1)/n} = \frac{\sigma_{n+1}}{\sigma_n} = e^{-b} + \frac{\bar{n}}{n+1} = a_0 + \frac{a_1}{1 + (j - 4)}, \quad (6.4)$$

where  $a_{0(1)}$  and  $b$  are constants,  $n$  is the number of jets in addition to the hard process,  $j$  is the inclusive number of jets, and  $\bar{n}$  is the expectation value for the Poisson distribution of exclusive jet cross-section at jet multiplicity  $n$ . The  $t\bar{t}W$  ME for SS2L events gives 4 jets in the hard process, so  $n$  is defined starting from the 5<sup>th</sup> jets and the inclusive number of jets  $j = n + 4$ . The two terms in Equation 6.4 correspond to staircase and Poisson scaling in cross section between successive jet multiplicities and are sensitive to high and low jet multiplicity events respectively [155]. The scaling pattern can then be reparameterized in  $a_0$  and  $a_1$  to obtain the  $t\bar{t}W$  yield at  $j' \equiv j + 1$  jets

$$\text{Yield}_{t\bar{t}W(j')} = \text{Yield}_{t\bar{t}W(N_{\text{jets}}=4)} \times \prod_{j=4}^{j'-1} \left( a_0 + \frac{a_1}{1 + (j - 4)} \right) \quad (6.5)$$

with  $j \geq 4$ . The  $t\bar{t}W$  yield in the 4-jet bin can be represented by a NF applied to  $t\bar{t}W$  MC simulation

$$\text{Yield}_{t\bar{t}W(N_{\text{jets}}=4)} = \text{NF}_{t\bar{t}W(N_{\text{jets}}=4)} \times \text{MC}_{t\bar{t}W(N_{\text{jets}}=4)}. \quad (6.6)$$

To account for the asymmetry in  $t\bar{t}W^+$  and  $t\bar{t}W^-$  cross-sections,  $\text{NF}_{t\bar{t}W(N_{\text{jets}}=4)}$  is further split into  $\text{NF}_{t\bar{t}W^\pm(N_{\text{jets}}=4)}$  assuming the scaling is the same for both processes. Both NFs are left free-floating to constrain  $t\bar{t}W$  yields in the 4-jet bin within CR 1b(+) and CR 1b(-). The final  $N_{\text{jets}}$ -parameterized function can then be represented by  $\text{NF}_{t\bar{t}W(j')}$  as

$$\text{NF}_{t\bar{t}W(j')} = \left( \text{NF}_{t\bar{t}W^+(N_{\text{jets}}=4)} + \text{NF}_{t\bar{t}W^-(N_{\text{jets}}=4)} \right) \times \prod_{j=4}^{j'-1} \left( a_0 + \frac{a_1}{1 + (j - 4)} \right). \quad (6.7)$$

The normalization is calculated and applied separately for each sub-sample of  $t\bar{t}W^+$  and  $t\bar{t}W^-$  in a  $N_{\text{jets}}$  bin for  $4 \leq N_{\text{jets}} < 10$ . Due to small contributions in the CRs, events

with  $N_{\text{jets}} < 4$  and  $N_{\text{jets}} \geq 10$  are not normalized with this scheme. Instead,  $N_{\text{jets}} < 4$  events are fitted by propagating the normalization in the 4-jet bin without additional shape correction. The correction factor for  $t\bar{t}W$  events with  $N_{\text{jets}} \geq 10$  is obtained by summing up the overflow from  $N_{\text{jets}} = 10$  to  $N_{\text{jets}} = 12$ , described as  $\sum_{j'=10}^{12} \prod_{j=4}^{j'-1} \left( a_0 + \frac{a_1}{1+(j-4)} \right)$ . Events with  $N_{\text{jets}} \geq 13$  are negligible and are not included in the sum.

The four regions, CR  $t\bar{t}W^\pm$  and CR 1b( $\pm$ ), are constructed to fit  $\text{NF}_{t\bar{t}W^\pm(N_{\text{jets}}=4)}$  and the scaling parameters  $a_{0(1)}$ , as well as validating the parameterization. Assuming the  $N_{\text{jets}}$  distribution of  $t\bar{t}W$  is similar across bins of  $N_b$ -jets, a fitted  $N_{\text{jets}}$  distribution in CR 1b( $\pm$ ) can be used to describe the  $t\bar{t}W$  parameterization at higher  $N_{\text{jets}}$ .

# Chapter 7. Systematic Uncertainties

Physics analysis inherently incurs uncertainties in the form of statistical and systematic uncertainties, depending on the source. Statistical uncertainties occur in this analysis from sample size of collected data and simulated MC samples, and from the maximizing of the LH function. Systematic uncertainties depend on identifiable sources in the analysis i.e. from detector and reconstruction effects (experimental uncertainties) or theoretical modeling (theoretical uncertainties). Systematic uncertainties are represented as nuisance parameters (NPx) in the profile LH fit. During the fit, systematic uncertainties with negligible impact on the final results can be pruned to simplify the statistical model and reduce computational complexity. This section outlines all uncertainties considered in this analysis.

## 7.1 Experimental uncertainties

### 7.1.1 Luminosity & pile-up reweighting

The uncertainty on the integrated luminosity of the 2015-2018 Run 2 data set is 0.83% [89], obtained by the LUCID-2 detector [156] for the primary luminosity measurements and complemented by the ID and calorimeters. Pile-up was modeled in MC and calibrated to data through pile-up reweighting, resulting in a set of calibration SFs and associated uncertainties.

### 7.1.2 Leptons

In general, calibrating MC simulations to match performance in data incurs uncertainties associated obtaining the MC-to-data calibration SFs, which are in turn propagated to observ-

ables in the analysis. The data-to-MC calibration of trigger, reconstruction, identification and isolation efficiencies for electrons and muons incur associated uncertainties, with separate systematic and statistical components for those related to muons. Similarly, electron energy scale, muon momentum scale and resolution are also subjected to calibration uncertainties estimated by re-simulating the events while varying the energy/momentun scale and resolution. Electron has an additional uncertainty related to ECIDS efficiency. Muon has additional uncertainties for charge-independent and charge-dependent momentum scale, as well as detector-specific track resolution. Systematic uncertainties for electron reconstruction, identification, isolation, ECIDS efficiencies and muon ID/MS energy resolution were not ready for the sample version used in this analysis, and are therefore not included.

### 7.1.3 Jets

Experimental uncertainties for jets are dominated by flavor tagging-related uncertainties, with subleading contributions from uncertainties related to JES [112], JER [111] and JVT [157] calibrations.

#### Jet energy scale

Uncertainties associated with JES are determined using data from LHC collisions along with MC simulated samples [112], decomposed into uncorrelated components:

- **Effective NPs:** 15 total  $p_T$ -dependent uncertainty components measured in situ, grouped based on their origin (2 detector-related, 4 modeling-related, 3 mixed, 6 statistical-related)
- $\eta$  **intercalibration:** 6 total components (1 modeling-related, 4 non-closure and 1

statistical-related) associated with the correction of the forward jets' ( $0.8 \leq |\eta| < 4.5$ ) energy scale to that of the central jets ( $|\eta| < 0.8$ ).

- **Flavor composition & response:** 2 components for relative quark-gluon flavor compositions in background and signal samples, and 2 components for responses to gluon-initiated versus quark-initiated jets.
- **Pile-up subtraction:** 4 components, 2 for  $\mu$  (`OffsetMu`) and  $N_{\text{PV}}$  (`OffsetNPV`) modeling, 1 for residual  $p_{\text{T}}$ -dependency (`PtTerm`) and 1 for topology dependence on the per-event  $p_{\text{T}}$  density modeling (`RhoTopology`).
- **Punch-through effect treatment:** 2 terms for GSC punch-through jet response deviation between data and MC, one for each detector response simulation method (AF3 and FS).
- **Non-closure:** 1 term applied to AF3 sample to account for the difference between AF3 and FS simulation.
- **High- $p_{\text{T}}$  single-particle response:** 1 term for the response to high- $p_{\text{T}}$  jets from single-particle and test-beam measurements.
- **$b$ -jets response:** 1 term for the difference between  $b$ -jets and light-jets response.

## Jet energy resolution

Measurements of JER were performed in bins of  $p_{\text{T}}$  and  $\eta$ , separately in data using in-situ techniques and in MC simulation using dijet events [111]. This analysis uses the full correlation JER uncertainty scheme provided for Run 2 analysis with 14 total components:

12 for effective NPs and 2 for difference between data and MC, separately for AF3 and FS [111].

### Jet vertex tagging

The uncertainty associated with JVT is obtained by varying the JVT efficiency SFs within their uncertainty range [157]. This uncertainty accounts for remaining contamination from pile-up jets after applying pile-up suppression and MC generator choice.

### Flavor tagging

Calibration SFs for  $b$ -tagging efficiencies and  $c$ -/light-jets mistagging rates are derived as a function of  $p_T$  for  $b$ -,  $c$ -, light-jets and PCBT score. The full set of flavor tagging-related uncertainties was reduced in dimensions by diagonalizing the uncertainty covariance matrix via eigendecomposition [115], resulting in a compact set of orthogonal NPs for this analysis: 85 for  $b$ -jets, 56 for  $c$ -jets and 42 for light-jets.

#### 7.1.4 Missing transverse energy

Uncertainties on  $E_T^{\text{miss}}$  arise from possible mis-calibration of the soft-track component and are estimated using data-to-MC comparison of the  $p_T$  scale and resolution between the hard and soft  $E_T^{\text{miss}}$  components [119]. These uncertainties are represented by three independent terms: 1 for scale uncertainty and 2 for resolution uncertainty of the parallel and perpendicular components.

## 7.2 Modeling uncertainties

### 7.2.1 Signal and irreducible background uncertainties

The signal and background samples used are modeled using MC simulation. Most uncertainties on simulation parameters (e.g. generator choice, PS model) are estimated by varying the relevant parameters and comparing them with the nominal sample. Uncertainties involving PDF in particular for most processes in the analysis are set to a flat 1% uncertainty. Cross-section uncertainties were considered for all irreducible background except  $t\bar{t}W$ , which is normalized in dedicated CRs following section 6.3.3. Extra uncertainties for the production of four or more  $b$ -jets (additional  $b$ -jets) in association with  $t\bar{t}X$  and HF jets were also considered due to a lack of theoretical predictions or dedicated measurements, rendering MC modeling challenging. Uncertainties from missing higher-order QCD corrections in MC simulation are estimated by varying the renormalization scale  $\mu_R$  and factorization scale  $\mu_F$  within seven different combinations

$$(\mu_R, \mu_F) = \{(0.5, 0.5), (0.5, 1), (1, 0.5), (1, 1), (1, 2), (2, 1), (2, 2)\}.$$

Process-specific uncertainty treatments are detailed below.

#### SM $t\bar{t}t\bar{t}$ background

The generator uncertainty for the SM  $t\bar{t}t\bar{t}$  background was evaluated between a nominal sample of MADGRAPH5\_AMC@NLO and SHERPA. The parton shower uncertainty was evaluated between PYTHIA8 and HERWIG. The cross-section uncertainty was estimated to

be 20% computed from a prediction at NLO in QCD+EW [128].

### **$t\bar{t}t$ background**

The cross-section uncertainty for  $t\bar{t}t$  was estimated to be 30% computed from a prediction at NLO in QCD+EW [128]. Events with additional  $b$ -jets also incur a 50% uncertainty.

### **$t\bar{t}W$ , $t\bar{t}Z$ , $t\bar{t}H$ backgrounds**

For  $t\bar{t}W$ ,  $t\bar{t}Z$  and  $t\bar{t}H$  backgrounds, an uncertainty of 50% is assigned to events with one additional truth  $b$ -jets that did not originate from a top quark decay, and an added 50% uncertainty is assigned to events with two or more [158] additional  $b$ -jets. The generator uncertainty was estimated for  $t\bar{t}Z$  using a MADGRAPH5\_AMC@NLO nominal sample and a SHERPA sample, and for  $t\bar{t}H$  using POWHEGBOX samples interfaced with PYTHIA8 (nominal) and HERWIG7. Cross-section uncertainties of 12% and 10% were applied to  $t\bar{t}Z$  and  $t\bar{t}H$  respectively [159]. No  $t\bar{t}W$  cross-section or PDF uncertainty was considered since the normalizations and jet multiplicity spectrum for  $t\bar{t}W$  are estimated using the data-driven method described in section 6.3.3.

### **Other backgrounds**

Other backgrounds include processes with small overall contribution in the SR. The cross-section uncertainty for  $tZ$  and  $tWH$  is considered to be 30% [160, 161]. A conservative cross-section uncertainty of 50% is applied to  $t\bar{t}VV$ ,  $VVV$  and  $VH$ . For  $VV$ , the cross-section uncertainty is dependent on jet multiplicity and is considered to be 20%/50%/60% for events with  $\leq 3/4 \geq 5$  jets [162]. For  $VV$ ,  $t\bar{t}VV$ ,  $VVV$  and  $VH$  events with additional truth  $b$ -jets, an uncertainty of 50% is applied.

### 7.2.2 Reducible background uncertainties

Reducible backgrounds consist of  $t\bar{t}/V + \text{HF}$  jets and single top events. Reducible background has small contamination within the SR, thus uncertainties related to reducible background have minor impact. Treatment for reducible background in this analysis largely follows Ref. [44], except for QmisID.

#### Charge misidentification

Uncertainties on the QmisID background originate from the charge flip rates obtained using the data-driven method described in section 6.3.2. Four sources of uncertainty were considered: statistical uncertainty from the maximum LLH estimation using Equation 6.2; uncertainty from choice of the  $Z$ -mass window and sidebands; non-closure uncertainty defined as the relative difference between the number of SS and OS events; and statistical uncertainty from the  $N_{\text{jets}}$  dependency correction SFs. The combined uncertainties from all four sources are calculated separately for each region involved in section 6.3.2, and are treated as correlated across all regions. Figure 7.1 shows the uncertainty calculated for SR.

#### Internal (low $\gamma^*$ ) and material conversion

The normalization for internal and material conversion backgrounds are free parameters in the fit, as a result the only uncertainties evaluated are from the shape of the distributions used in the template fit method (see section 6.3.1). The uncertainties on internal (material) conversion are estimated based on the difference between data and MC prediction in a region enriched in  $Z + \gamma \rightarrow \mu^+\mu^- + e^+e^-$  events.

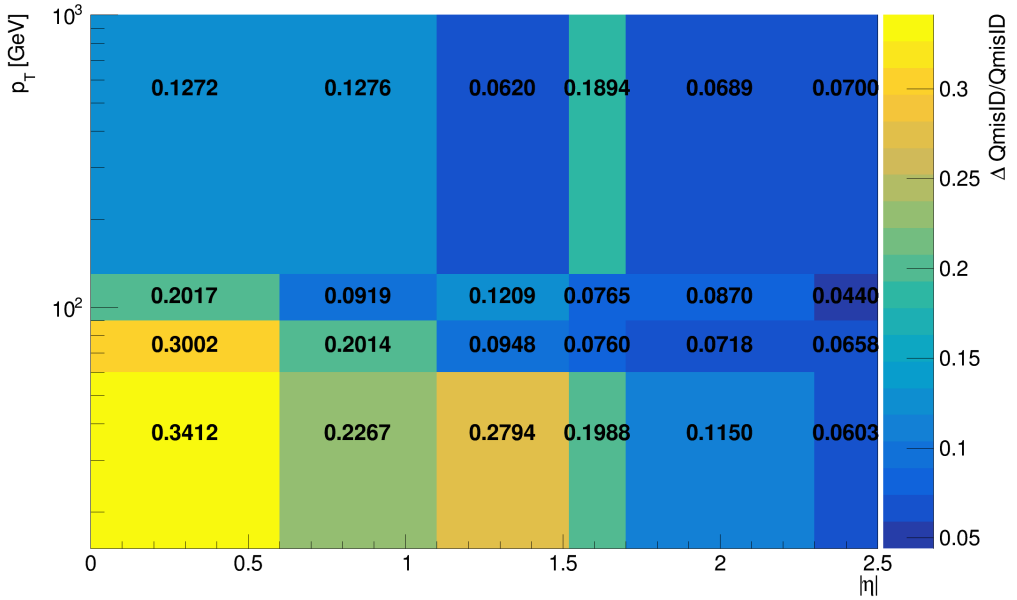


Figure 7.1: Combined QmisID uncertainty rate for SR in bins of  $|\eta|$  and  $p_T$ .

### Heavy-flavor non-prompt lepton

Similar to the conversion backgrounds, the uncertainties on non-prompt HF decays come from the shape of the distributions, and are estimated by comparing data and MC prediction between all regions in the analysis on a per bin basis. The events used are required to contain at least one *Loose* reconstructed lepton used in the region selection criteria detailed in Table 6.1 to maintain orthogonality with the SR.

### Light-flavor decays and other fake/non-prompt backgrounds

A conservative normalization uncertainty of 100% is assigned for light-flavor non-prompt lepton background [151], and an ad-hoc normalization uncertainty of 30% is applied to all other fake and non-prompt backgrounds. The shape uncertainties for these backgrounds are negligible.

# Chapter 8. Results

## 8.1 Statistical interpretation

This section provides an overview of the statistical methods needed to interpret the collected and simulated data to estimate unknown physics parameters and determine compatibility between data and the analysis hypothesis. For the BSM resonance search, the null hypothesis  $H_0$  assumes only SM background contributions and none from any new BSM resonance in the data.

### 8.1.1 Profile likelihood fit

Given a set of observed data points  $\mathbf{x} = [x_1, x_2, \dots]$  and unknown parameters  $\boldsymbol{\theta} = [\theta_1, \theta_2, \dots, \theta_n]$ , the maximum likelihood method aims to find an estimate  $\hat{\boldsymbol{\theta}}$  that maximizes the joint probability function  $f(\mathbf{x}, \boldsymbol{\theta})$ , or in other words the set of parameters that gives the highest probability of observing the collected data points for a particular model. The function to be maximized for this purpose is the log-likelihood (LLH) function  $\ln \mathcal{L}(\mathbf{x}, \boldsymbol{\theta})$  where  $\mathcal{L}(\mathbf{x}, \boldsymbol{\theta}) \equiv \prod_i f(x_i, \boldsymbol{\theta})$  is defined as the likelihood (LH) function. The LLH is maximized when  $\partial/\partial\theta_i (\ln \mathcal{L}) = 0$  for each parameter  $\theta_i$ .

For an usual binned physics analysis, the above variables for the LH function  $\mathcal{L}$  can be expressed as nuisance parameters (NP)  $\boldsymbol{\theta}$  and number of events for a model  $N_i(\mu)$  for the  $i^{\text{th}}$  bin, where  $\mu$  is the targeted parameter of interest (POI). In this analysis,  $N_i$  is assumed to follow a Poisson distribution and depends on the following quantities: the signal strength  $\mu$  defined as the ratio of observed to expected cross sections  $\sigma_{\text{obs}}/\sigma_{\text{exp}}$ ; nuisance parameters  $\boldsymbol{\theta}$  which represents the effects of systematic uncertainties, implemented in the

LH function as Gaussian constraints; and normalization factors (NFs)  $\boldsymbol{\lambda}$  that control the normalization of background components that do not have a well-known cross section. The Poisson probability of observing exactly  $N_i$  events for an expected number of event  $n_i$  is

$$\mathcal{P}(N_i|n_i(\mu, \boldsymbol{\lambda})) = \frac{n_i^{N_i} e^{-n_i}}{N_i!}. \quad (8.1)$$

The expected Poisson event number in a bin  $i$  can be parameterized as

$$n_i = \mu s_i(\boldsymbol{\theta}) + \sum_j \lambda_j b_{ij}(\boldsymbol{\theta}), \quad (8.2)$$

where  $s_i$  is the number of signal events in bin  $i$  of every region, and  $b_{ij}$  is the number of events for a certain background source index  $j$  in bin  $i$ . The LH function in this analysis can be written as

$$\mathcal{L}(\mathbf{N}|\mu, \boldsymbol{\theta}, \boldsymbol{\lambda}) = \left( \prod_i \mathcal{P}(N_i|n_i) \right) \cdot \prod_k \mathcal{G}(\theta_k), \quad (8.3)$$

where  $\mathcal{G}(\theta_k)$  is the Gaussian constraint for a NP  $k$ . The signal significance  $\mu$  and NFs  $\boldsymbol{\lambda}$  are left unconstrained and are fitted simultaneously in the profile LH fit. Define the profile LH ratio [163] as

$$\lambda(\mu) = \frac{\mathcal{L}(\mu, \hat{\boldsymbol{\theta}}_\mu, \hat{\boldsymbol{\lambda}}_\mu)}{\mathcal{L}(\hat{\mu}, \hat{\boldsymbol{\theta}}, \hat{\boldsymbol{\lambda}})}, \quad (8.4)$$

where  $\hat{\mu}$ ,  $\hat{\boldsymbol{\theta}}$  and  $\hat{\boldsymbol{\lambda}}$  are parameter values that optimally maximizes the LH function, and  $\hat{\boldsymbol{\theta}}_\mu$ ,  $\hat{\boldsymbol{\lambda}}_\mu$  are NP and NF values respectively that maximize the LH function for a given signal strength  $\mu$ . Using Neyman-Pearson lemma [164], the optimal test statistic for hypothesis testing is

$$q_\mu \equiv -2 \ln \lambda(\mu), \quad (8.5)$$

where  $q_\mu = 0$  or  $\lambda(\mu) = 1$  corresponds to perfect agreement between the optimal parameter  $\hat{\mu}$  obtained from data and the hypothesized value  $\mu$ . From Wilks' theorem [165], the test statistic  $q_\mu$  approaches a  $\chi^2$  distribution and can be evaluated as  $q_\mu = (\mu - \hat{\mu})^2 / \sigma_\mu^2$ .

When evaluating against the background-only hypothesis ( $\mu = 0$ ), it can be assumed that the number of events observed under the signal hypothesis is higher than that of the background-only hypothesis, or  $\mu \geq 0$  according to Equation 8.2. This leads to a corresponding lower bound on the test statistic

$$q_0 = \begin{cases} -2 \ln \lambda(0), & \text{if } \hat{\mu} \geq 0, \\ 0, & \text{if } \hat{\mu} < 0. \end{cases} \quad (8.6)$$

### **p-value**

To quantify the incompatibility between the observed data and the background-only hypothesis, the *p*-value is defined as  $p = P(q_\mu \geq q_{\mu, \text{obs}} | H_0)$  or in other words, the probability of observing data with a test statistic  $q_\mu$  under the null hypothesis  $H_0$  that is less compatible with  $H_0$  than the actual observed data with test statistic  $q_{\mu, \text{obs}}$ . The *p*-value can be expressed in terms of  $q_\mu$  as

$$p_\mu = \int_{q_{\mu, \text{obs}}}^{\infty} f(q_\mu | \mu) dq_\mu, \quad (8.7)$$

where  $f(q_\mu | \mu) dq_\mu$  is the conditional probability density function of  $q_\mu$  given  $\mu$ .

In some cases, it is more convenient to evaluate compatibility using the *Z*-value, defined as the number of standard deviations between the observed data and the mean in a Gaussian

distribution. The  $p$ -value can be converted to  $Z$ -value via the relation

$$Z = \Phi^{-1}(1 - p), \quad (8.8)$$

where  $\Phi$  is the quantile of the standard Gaussian. Rejecting the signal hypothesis usually requires a 95% confidence level (CL) which corresponds to a  $p$ -value of 0.05 or a  $Z$ -value of 1.64, while rejecting the background-only hypothesis generally requires a  $Z$ -value of 5 or a  $p$ -value of  $2.84 \times 10^{-7}$ .

### 8.1.2 Exclusion limit

If the signal hypothesis is rejected, the exclusion upper limits can still be computed at a certain CL (usually 95%) to establish the maximum value of  $\mu$  that is not excluded by or in conflict with the observed data. The exclusion limits are calculated based on the CL<sub>s</sub> method [166, 167] under which the test statistic is defined as  $q_\mu = -2 \ln \frac{\mathcal{L}_{s+b}}{\mathcal{L}_b}$  with  $\mathcal{L}_{s+b}$  being the LH function for the signal and background hypothesis ( $\mu > 0$ ) and  $\mathcal{L}_b$  being the LH function for the background-only hypothesis ( $\mu = 0$ ). The  $p$ -value for both hypotheses can then be expressed as

$$\begin{aligned} p_{s+b} &= P(q \geq q_{\text{obs}} | s + b) = \int_{q_{\text{obs}}}^{\infty} f(q | s + b) dq \\ p_b &= P(q \geq q_{\text{obs}} | b) = \int_{-\infty}^{q_{\text{obs}}} f(q | b) dq. \end{aligned} \quad (8.9)$$

The signal hypothesis is excluded for a CL  $\alpha$  when the following condition is satisfied

$$\text{CL}_s \equiv \frac{p_{s+b}}{p_b} \geq 1 - \alpha. \quad (8.10)$$

The value of  $\mu$  such that the signal hypothesis leads to  $CL_s = 1 - \alpha = 0.05$  is then the exclusion upper limit at a 95% CL. Exclusion limits are usually reported in terms of expected and observed limits. The expected limits show the exclusion limits obtained under the background-only hypothesis and represent the analysis' sensitivity, while the observed limits represent exclusion limits derived from observed data.

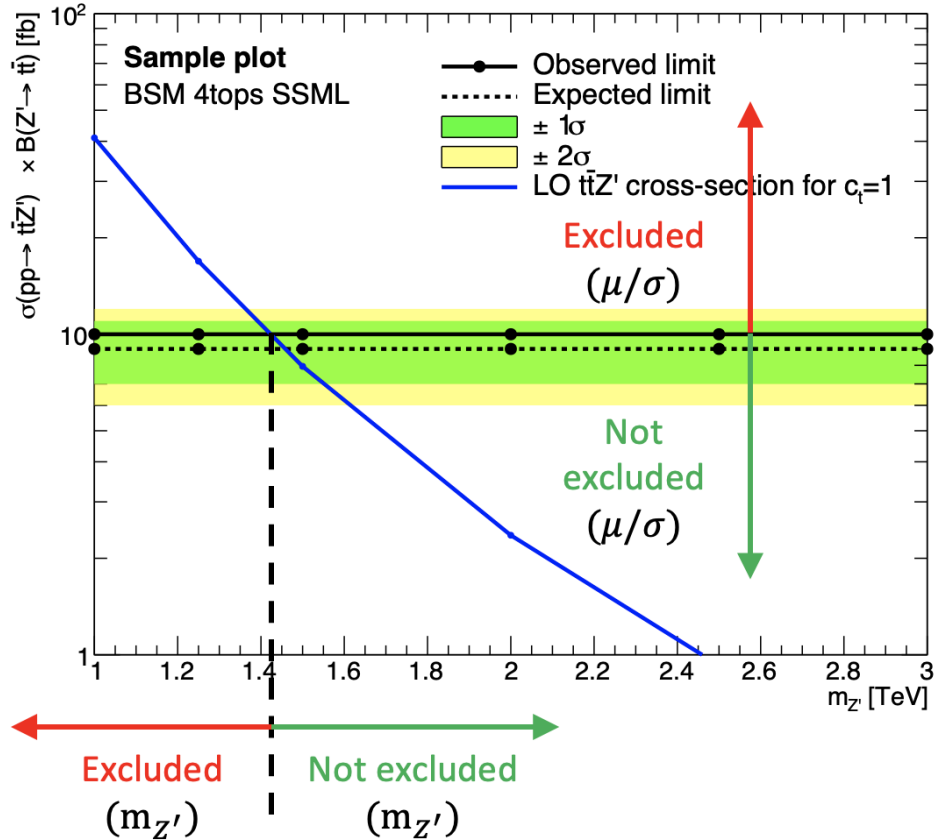


Figure 8.1: Example of an exclusion limit graph. The solid (dotted) line represents the observed (expected) upper limits as a function of the  $Z'$  mass at 95% CL on the cross-section of  $pp \rightarrow t\bar{t}Z'$  production times the  $Z' \rightarrow t\bar{t}$  branching ratio. The solid blue line represents the theoretical signal cross-section with  $c_t = 1$  at LO in QCD [74]. The green and yellow bands represent the 68% ( $\pm 1\sigma$ ) and 95% ( $\pm 2\sigma$ ) confidence intervals for the expected upper limits. Cross section of  $t\bar{t}Z'$  within the region above the observed limit is excluded under the current model. Masses below the  $m_{Z'}$  value at which the observed limit intersect the theoretical cross section are excluded.

In a search for an exotic particle of unknown mass, a lower bound on the mass can

be determined using the theoretical cross section for the particle and the obtained observed limits. Figure 8.1 shows a sample exclusion limit graph of the  $t\bar{t}Z'$  cross section as a function of the  $Z'$  mass. Values of the signal strength  $\mu$  (and by proxy the cross section  $\sigma$  via  $\mu = \sigma/\sigma_{\text{theory}}$ ) above the observed limits are incompatible with the analysis model. Consequently, mass points with a smaller observed cross section than the theoretical cross section are excluded from the model; the cross section for the particle predicted by the analysis model lies in the exclusion region obtained using observed data. Such masses are eliminated as a possibility for the model.

## 8.2 Fit results

The signal strength  $\mu$ , background NFs,  $t\bar{t}W$  scaling factors and uncertainty NPs are simultaneously fitted using a binned profile LLH fit under the background-only hypothesis to the  $H_T$  distribution in the SR and to corresponding distributions shown in Table 6.1 for CRs.

Before fitting to real data (unblinded fit), the fit was first performed in both the SR and CRs using Asimov pseudo-datasets, in which the simulated data match exactly to MC prediction with nominal  $\mu$  set to 0. This is done for the purpose of optimizing object selection criteria and region definition, refining background estimation techniques and testing the statistical interpretation model for signal extraction described in section 8.1. The fit is then performed with Asimov data in the SR and real data in CRs to validate background modeling, estimate sensitivity and assess the influence of statistical effects on fitted parameters. Finally, the fully unblinded fit is performed with real data in all regions.

The unblinded fit results are presented below. No significant variation is observed in fit

output behavior using  $t\bar{t}Z'$  samples of different  $m_{Z'}$ ; results fitted using  $m_{Z'} = 2$  TeV are shown without substantial loss of generality. The background modeling is evaluated under the background-only hypothesis. The fitted background NFs are shown in Table 8.1 and are consistent with their nominal values within one standard deviation, or two standard deviations in the case of  $\text{NF}_{\text{HF } e}$  and  $\text{NF}_{t\bar{t}W^+(4j)}$ . Figure 8.2 shows good agreement between data and post-fit background distributions in non-prompt background CRs and  $t\bar{t}W$  CRs.

The pre-fit and post-fit background yields are shown in Table 8.2. Except for HF  $e$  background, post-fit yields for various backgrounds e.g.  $t\bar{t}t\bar{t}$ ,  $t\bar{t}H$ , other fake, etc. are increased; the pre-fit to post-fit variations are consistent within  $\pm\sigma$ . Post-fit yield for HF  $e$  background is lowered compared to pre-fit yield within  $2\sigma$  which can be related to the fitted value of  $\text{NF}_{\text{HF } e}$  in Table 8.1; however, this difference in pre- and post-fit yields of HF  $e$  background has negligible impact on the  $\mu$  as seen in Table 8.3. Post-fit yields for signal are consistent with zero within  $\pm 2\sigma$ . Data and total post-fit yields are consistent within  $\pm 1\sigma$ .

Table 8.3 outlines the impact on the signal strength  $\mu$  of various sources of uncertainty grouped by their corresponding category. The background sources of uncertainty with the largest impact is  $t\bar{t}t\bar{t}$  modeling, in particular  $t\bar{t}t\bar{t}$  generator choice and cross-section uncertainties, followed by  $t\bar{t}W$  modeling due to their significant contributions in the SR observed in Figure 6.1, especially in the more sensitive regions requiring three or more  $b$ -tagged jets. The most significant impact on  $\mu$  within the set of instrumental uncertainties are uncertainties on jet  $b$ -tagging attributable to the high jet and  $b$ -jet multiplicities in the BSM  $t\bar{t}t\bar{t}$  signal signature.

Figure 8.4 shows the post-fit pull from the nominal pre-fit value for each nuisance parameter. Pull for all NPs are consistent within one standard deviation from the nominal pre-fit value. Overall, modeling uncertainties suffer from more significant pull compared to experi-

mental uncertainties. Uncertainty sources with the largest pull are SM  $t\bar{t}t\bar{t}$  cross section and generator choice, along with  $t\bar{t}Z$  generator choice and diboson cross section. Additionally, no significant constraints are placed on NPs by the fit to data, with the exception of moderate constraint on the diboson cross section.

No significant excess over SM predictions is observed, and the fitted signal strength  $\mu$  is compatible with zero for all  $Z'$  mass points. Figure 8.5 shows the observed and expected upper limits at 95% confidence level on the cross-section of  $pp \rightarrow t\bar{t}Z'$  production times the branching ratio of  $Z' \rightarrow t\bar{t}$  as a function of the  $Z'$  resonance mass. The  $\pm 1\sigma$  and  $\pm 2\sigma$  confidence intervals around the expected exclusion limits are also shown. The observed exclusion limits range from 7.9 fb to 9.44 fb depending on  $m_{Z'}$ . The distribution of limits across  $m_{Z'}$  is flat and show little correlation to signal kinematics and phase space modeling. The observed limits exclude  $Z'$  masses below  $\approx 15$  TeV.

Table 8.1: Normalization factors for backgrounds with dedicated CRs, obtained from a simultaneous fit in all CRs and SR under the background-only hypothesis. The nominal pre-fit value is 1 for all NFs and 0 for the scaling factors  $a_0$  and  $a_1$ . Uncertainties shown include both statistical and systematic uncertainties.

Parameter	$NF_{HF\ e}$	$NF_{HF\ \mu}$	$NF_{Mat.\ Conv.}$	$NF_{Low\ m_{\gamma^*}}$	$a_0$	$a_1$	$NF_{t\bar{t}W^+(4j)}$	$NF_{t\bar{t}W^-(4j)}$
Fit value	$0.68^{+0.23}_{-0.22}$	$0.97^{+0.17}_{-0.16}$	$0.97^{+0.31}_{-0.28}$	$0.97^{+0.23}_{-0.20}$	$0.39^{+0.11}_{-0.11}$	$0.42^{+0.25}_{-0.24}$	$1.21^{+0.18}_{-0.18}$	$1.10^{+0.26}_{-0.26}$

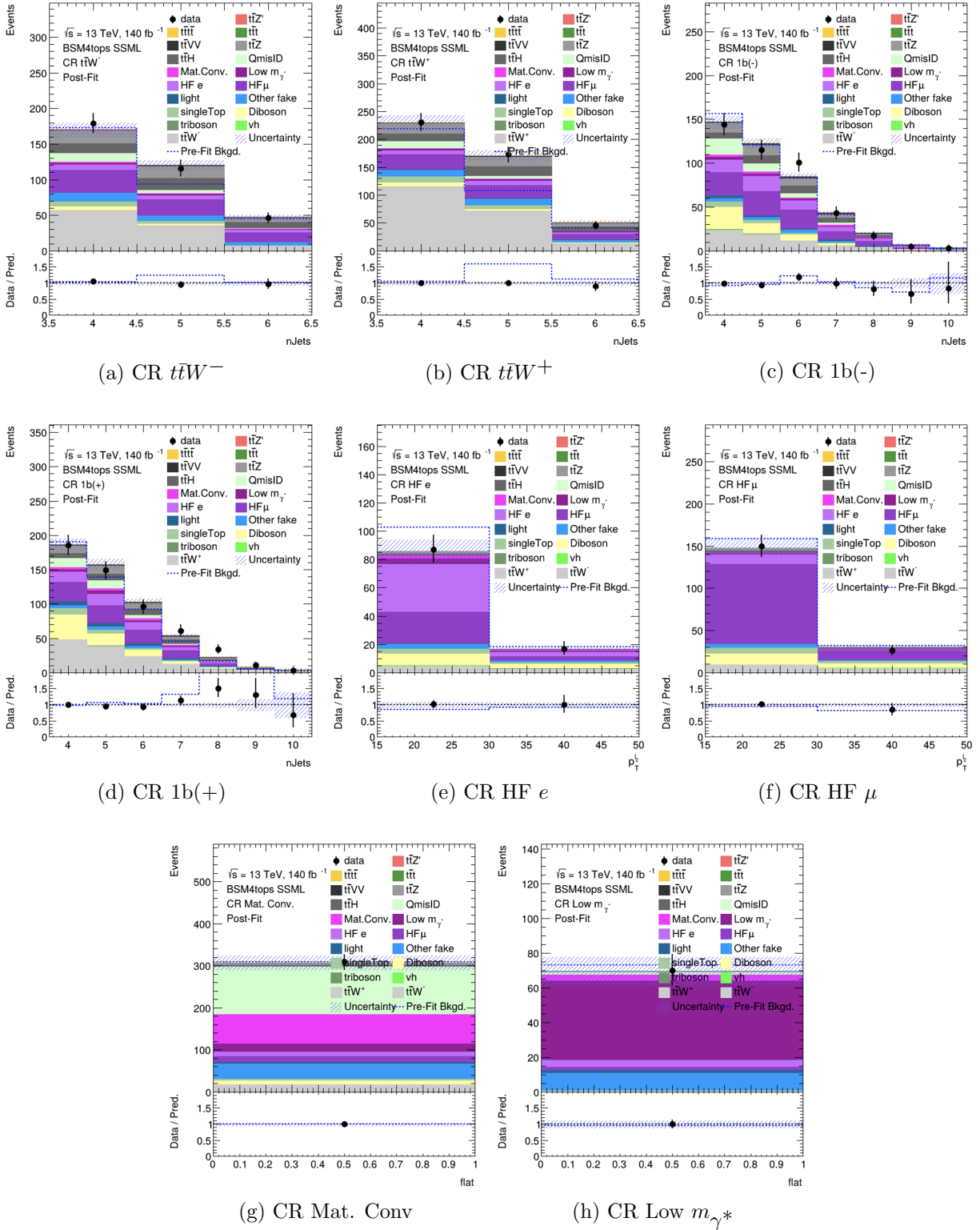
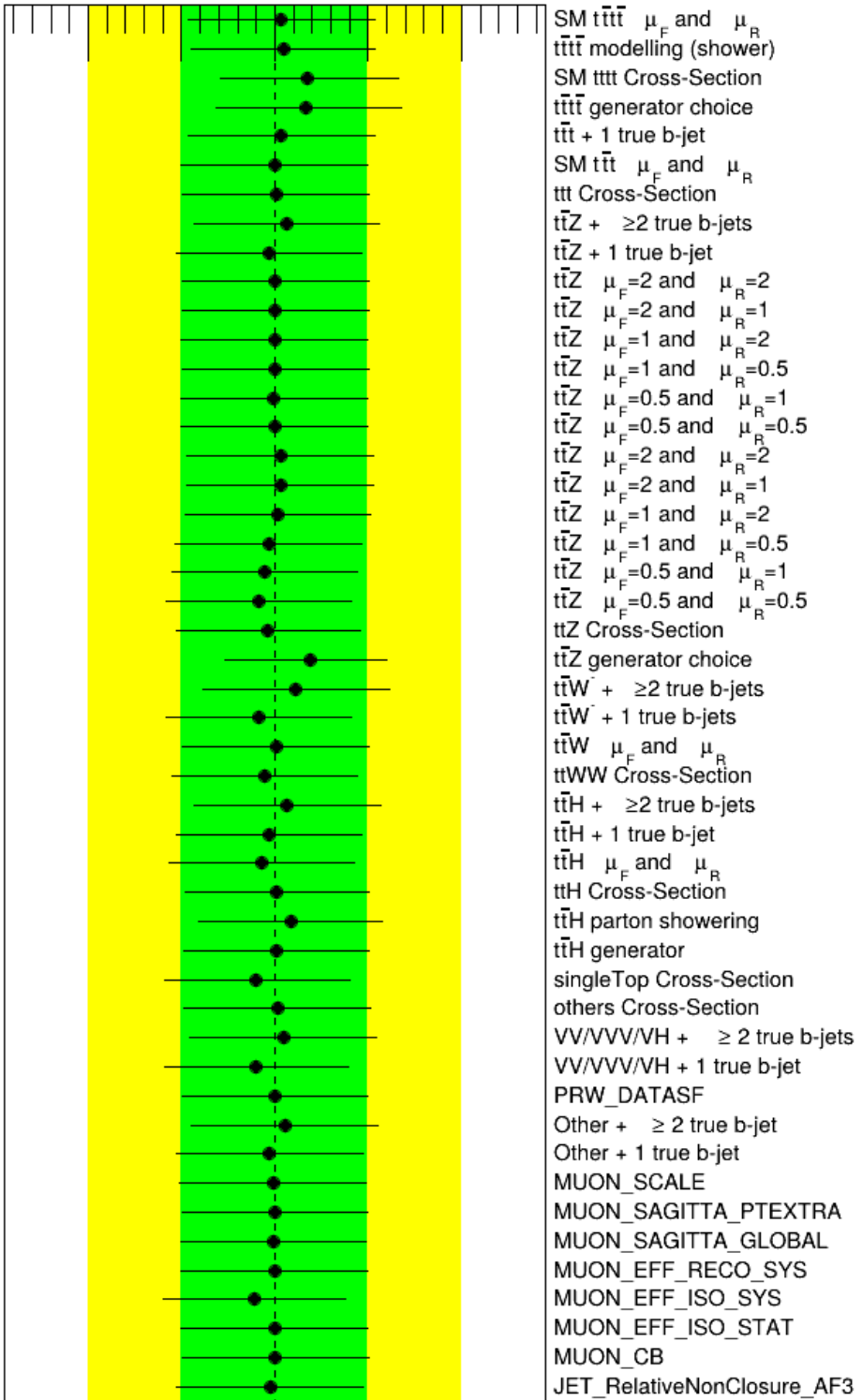
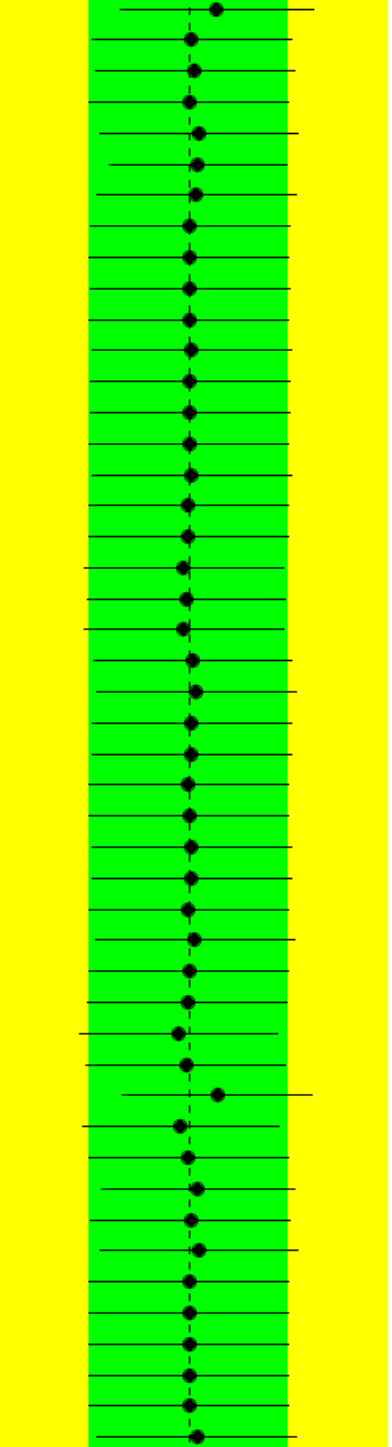


Figure 8.2: Comparison between data and post-fit prediction for the discriminant observable in each CR. Distributions shown are obtained from the fit using the  $t\bar{t}Z'$  signal sample with  $m_{Z'} = 2$  TeV. The lower panel shows the ratio between data and post-fit predictions. The shaded band represents the total uncertainty on the fit. The dashed line represents the pre-fit distribution.



	
	<p>JET_Pileup_RhoTopology  JET_Pileup_PtTerm  JET_Pileup_OffsetNPV  JET_Pileup_OffsetMu  JET_NNJvtEfficiency  JET_JESUnc_VertexingAlg_PreRec  JET_JESUnc_Noise_PreRec  JET_JER_EffectiveNP_9_PseudoData  JET_JER_EffectiveNP_9  JET_JER_EffectiveNP_8_PseudoData  JET_JER_EffectiveNP_8  JET_JER_EffectiveNP_7_PseudoData  JET_JER_EffectiveNP_7  JET_JER_EffectiveNP_6_PseudoData  JET_JER_EffectiveNP_6  JET_JER_EffectiveNP_5_PseudoData  JET_JER_EffectiveNP_5  JET_JER_EffectiveNP_4_PseudoData  JET_JER_EffectiveNP_4  JET_JER_EffectiveNP_3_PseudoData  JET_JER_EffectiveNP_3  JET_JER_EffectiveNP_2_PseudoData  JET_JER_EffectiveNP_2  JET_JER_EffectiveNP_1_PseudoData  JET_JER_EffectiveNP_12restTerm_PseudoData  JET_JER_EffectiveNP_12restTerm  JET_JER_EffectiveNP_11_PseudoData  JET_JER_EffectiveNP_11  JET_JER_EffectiveNP_10_PseudoData  JET_JER_EffectiveNP_10  JET_JER_EffectiveNP_1  JET_JER_DataVsMC_MC16_PseudoData  JET_JER_DataVsMC_MC16  JET_JERUnc_Noise_PreRec_PseudoData  JET_JERUnc_Noise_PreRec  JET_InSitu_NonClosure_PreRec  JET_Flavor_Response  JET_Flavor_Composition_Sig  JET_Flavor_Composition_Bkg  JET_EtaIntercalibration_TotalStat  JET_EtaIntercalibration_NonClosure_PreRec  JET_EtaIntercalibration_Modelling  JET_EffectiveNP_Statistical5  JET_EffectiveNP_Statistical2  JET_EffectiveNP_Modelling3  JET_EffectiveNP_Modelling2  JET_EffectiveNP_Modelling1</p>

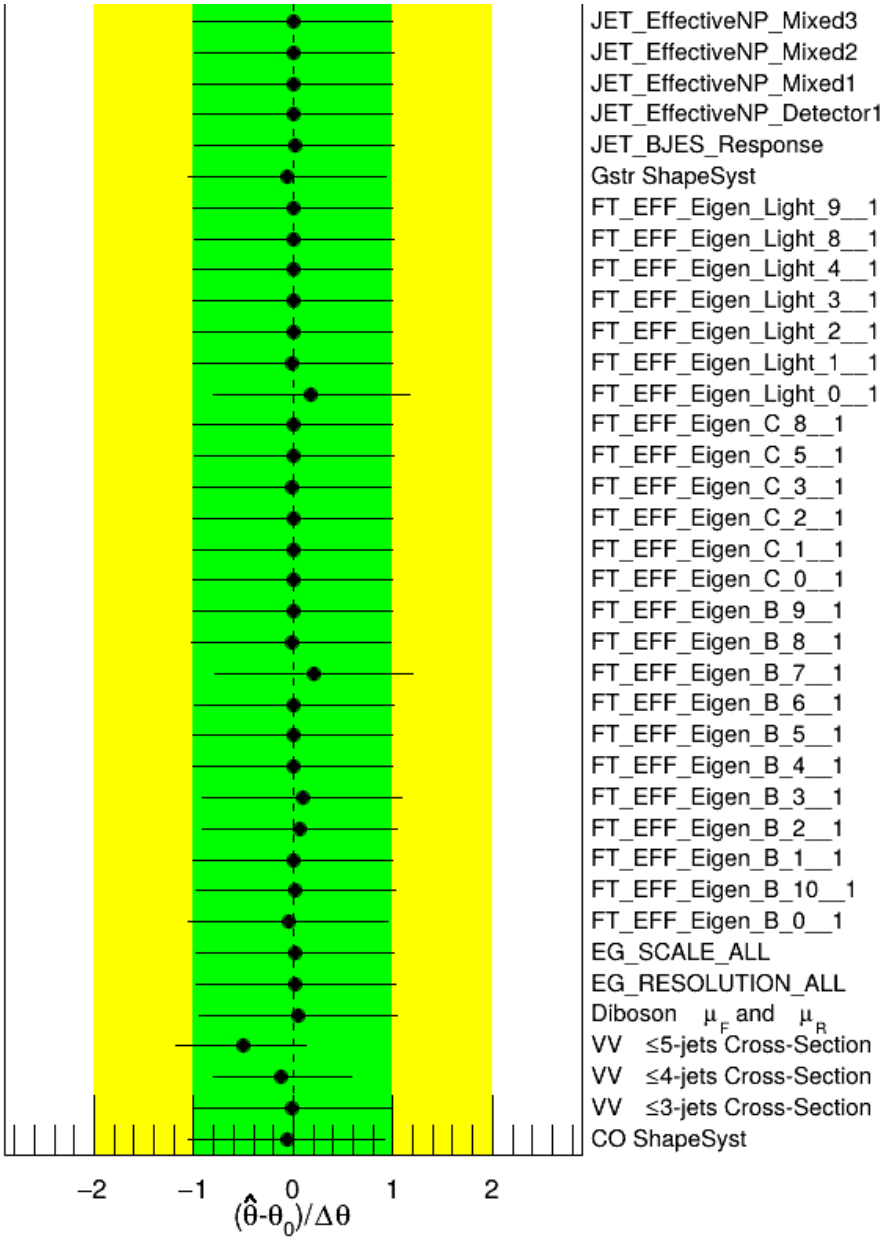


Figure 8.4: Post-fit pull from nominal values for nuisance parameters representing systematic uncertainties. Systematics pruned during the fit are not shown. The dashed line represents the nominal pre-fit values. The green and yellow bands represent the 68% ( $\pm 1\sigma$ ) and 95% ( $\pm 2\sigma$ ) confidence intervals for the nominal fit value.

Table 8.2: Pre-fit and post-fit background yields in the inclusive SR. The number of data events and pre-fit estimate signal yields are also shown. Background yields shown are obtained using the  $t\bar{t}Z'$  signal sample with  $m_{Z'} = 2$  TeV. Total yield uncertainty differs from the quadrature sum of constituent uncertainties due to (anti-)correlation effects.

Process	Pre-fit	Post-fit
<b>Background</b>		
$t\bar{t}t\bar{t}$	$42.35 \pm 9.57$	$46.80 \pm 9.75$
$t\bar{t}W^+$	$97.38 \pm 0.71$	$104.36 \pm 19.44$
$t\bar{t}W^-$	$56.92 \pm 0.42$	$55.36 \pm 13.88$
$t\bar{t}Z$	$78.02 \pm 19.24$	$71.51 \pm 15.29$
$t\bar{t}H$	$81.00 \pm 9.91$	$83.16 \pm 9.76$
$t\bar{t}t$	$3.33 \pm 1.03$	$3.36 \pm 1.04$
Single-top ( $tq$ , $tZq$ , $tWZ$ , etc.)	$13.38 \pm 4.08$	$12.70 \pm 4.01$
$t\bar{t}VV/t\bar{t}VH/t\bar{t}HH$	$17.07 \pm 6.75$	$16.42 \pm 6.66$
Charge misidentification	$40.31 \pm 0.32$	$40.31 \pm 0.00$
$VV/VVV/VH$	$10.01 \pm 6.27$	$6.72 \pm 3.62$
Mat. Conv.	$26.20 \pm 0.95$	$25.72 \pm 7.88$
Low $m_{\gamma^*}$	$26.14 \pm 0.74$	$25.51 \pm 5.61$
HF $e$	$21.99 \pm 2.02$	$15.37 \pm 5.01$
HF $\mu$	$31.33 \pm 3.96$	$31.41 \pm 6.07$
Light-flavor decays	$13.47 \pm 0.55$	$13.51 \pm 0.53$
Other fake & non-prompt	$24.90 \pm 2.73$	$26.01 \pm 2.35$
Total background	$583.77 \pm 32.02$	$578.23 \pm 27.11$
<b>Signal <math>t\bar{t}Z' \rightarrow t\bar{t}t\bar{t}</math></b>		
$m_{Z'} = 1$ TeV	$52.83 \pm 2.75$	$26.96 \pm 16.31$
$m_{Z'} = 1.25$ TeV	$52.94 \pm 2.72$	$25.02 \pm 15.45$
$m_{Z'} = 1.5$ TeV	$53.07 \pm 2.78$	$24.55 \pm 15.07$
$m_{Z'} = 2$ TeV	$52.49 \pm 2.76$	$24.52 \pm 14.91$
$m_{Z'} = 2.5$ TeV	$53.07 \pm 2.78$	$25.35 \pm 15.20$
$m_{Z'} = 3$ TeV	$52.45 \pm 2.80$	$25.64 \pm 15.26$
<b>Data</b>	604	

Table 8.3: Post-fit impact of uncertainty sources on the signal strength  $\mu$ , grouped by categories. Values shown are obtained from the fit using the  $t\bar{t}Z'$  signal sample with  $m_{Z'} = 2$  TeV. Impact on  $\mu$  is evaluated for each uncertainty category by re-fitting with the corresponding set of NPs fixed to their best-fit values. Total uncertainty differs from the quadrature sum of constituent uncertainties due to correlation between NPs in the fit.

Uncertainty source	$\Delta\mu$	
<b>Signal modeling</b>		
$t\bar{t}Z'$	+0.00	-0.00
<b>Background modeling</b>		
$t\bar{t}\bar{t}$	+0.15	-0.13
$t\bar{t}W$	+0.04	-0.03
$t\bar{t}Z$	+0.02	-0.02
$t\bar{t}H$	+0.02	-0.02
Non-prompt leptons	+0.00	-0.00
Other backgrounds	+0.02	-0.02
<b>Instrumental</b>		
Luminosity	+0.00	-0.00
Jet uncertainties	+0.04	-0.04
Jet flavor tagging ( $b$ -jets)	+0.04	-0.04
Jet flavor tagging ( $c$ -jets)	+0.01	-0.01
Jet flavor tagging (light-jets)	+0.02	-0.01
MC simulation sample size	+0.01	-0.01
Other experimental uncertainties	+0.01	-0.01
Total systematic uncertainty	+0.15	-0.17
<b>Statistical</b>		
$t\bar{t}W$ NFs and scaling factors	+0.01	-0.01
Non-prompt lepton NFs (HF, Mat. Conv., Low $m_{\gamma^*}$ )	+0.00	-0.00
Total statistical uncertainty	+0.25	-0.23
<b>Total uncertainty</b>	+0.29	-0.29

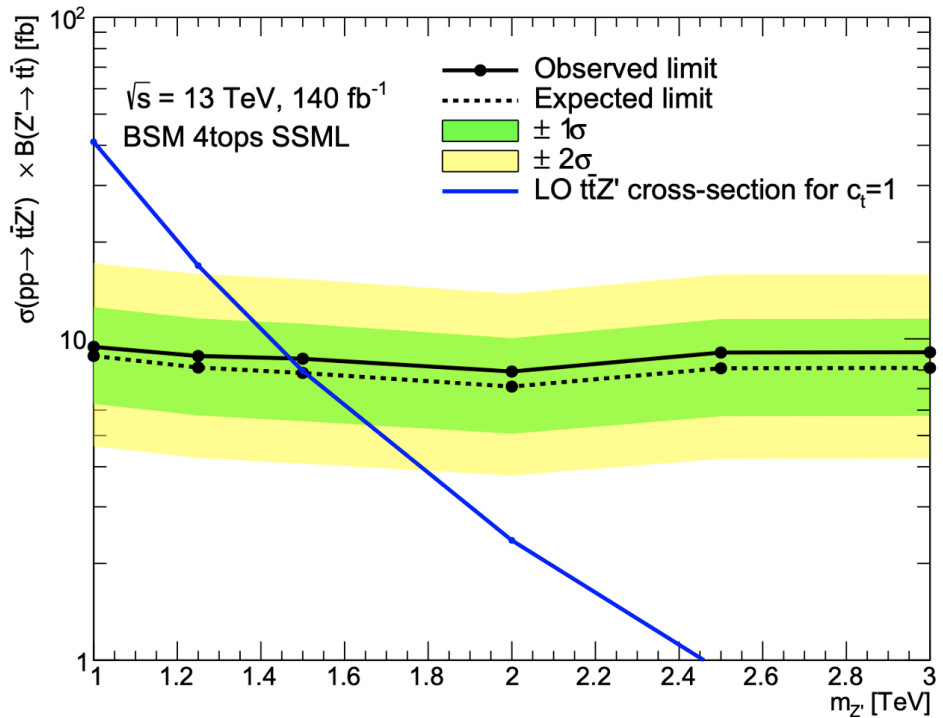


Figure 8.5: Observed (solid line) and expected (dotted line) upper limits as a function of the  $Z'$  mass at 95% CL on the cross-section of  $pp \rightarrow t\bar{t}Z'$  production times the  $Z' \rightarrow t\bar{t}$  branching ratio. The region above the observed limit is excluded. The solid blue line represents the theoretical signal cross-section with  $c_t = 1$  at LO in QCD [74]. The green and yellow bands represent the 68% ( $\pm 1\sigma$ ) and 95% ( $\pm 2\sigma$ ) confidence intervals for the expected upper limits.

# Chapter 9. Summary

This dissertation presents a search for BSM top-philic heavy vector resonance based on a simplified top-philic color singlet  $Z'(\rightarrow t\bar{t})$  model in the top-quark pair associated production channel ( $t\bar{t}Z'$ ). The search is performed in the same-sign dilepton and multilepton channel of the  $t\bar{t}t\bar{t}$  final states, using the full Run 2 data set collected between 2015 and 2018 by the ATLAS detector at the LHC, corresponding to an integrated luminosity of  $140 \text{ fb}^{-1}$  of  $pp$  collisions at center-of-mass energy  $\sqrt{s} = 13 \text{ TeV}$ .

New data-driven estimation methods for  $t\bar{t}W$  and charge misidentification background are employed to improve background modeling and signal sensitivity compared to previous analysis [28]. No significant excess over Standard Model predictions is observed. Observed exclusion limits at 95% confidence level as a function of the  $Z'$  mass are set on the production cross section of  $pp \rightarrow t\bar{t}Z'$  times the  $Z' \rightarrow t\bar{t}$  branching ratio, ranging from  $7.9 \text{ fb}$  (at  $m_{Z'} = 2 \text{ TeV}$ ) to  $9.4 \text{ fb}$  (at  $m_{Z'} = 1 \text{ TeV}$ ) depending on the  $Z'$  mass. This represent a significant improvement in the exclusion limit for  $t\bar{t}Z'$  [28], and are currently the most stringent upper limits to date. The analysis probes a  $Z'$  mass range from  $1 \text{ TeV}$  to  $3 \text{ TeV}$  under the assumption of a top- $Z'$  coupling strength of  $c_t = 1$  and chirality angle  $\theta = \pi/4$ .

Further improvements in analysis strategies, including multivariate techniques for signal discrimination, are expected to increase discovery potential in future searches. Looking forward, the upcoming Run 3 data at  $\sqrt{s} = 13.6 \text{ TeV}$  will increase the total integrated luminosity by about a factor of 2 [169] and the  $pp \rightarrow t\bar{t}t\bar{t}$  cross section by at least 19% [168], which will help to improve modeling for the SM  $t\bar{t}t\bar{t}$  background. Run 3 improvements along with prospects of the High-Luminosity LHC will enhance sensitivity to BSM physics and offer more opportunities to explore top-philic resonances and other exciting new phenomena.

# References

- [1] J. Schwinger. *On Quantum-Electrodynamics and the Magnetic Moment of the Electron.* Phys. Rev. 73 (4 1948), pp. 416–417 (cit. on p. 1).
- [2] R. P. Feynman. *Space-Time Approach to Quantum Electrodynamics.* Phys. Rev. 76 (6 1949), pp. 769–789 (cit. on p. 1).
- [3] S. Tomonaga. *On a relativistically invariant formulation of the quantum theory of wave fields.* Prog. Theor. Phys. 1 (1946), pp. 27–42 (cit. on p. 1).
- [4] E. Fermi. *An attempt of a theory of beta radiation. I.* Nuclear Physics B 4 (1967). Translated from the original 1934 German article by C. P. Enz and C. H. Beck, pp. 1–27 (cit. on p. 1).
- [5] D. J. Griffiths. *Introduction to Elementary Particles.* 2nd. Weinheim: Wiley-VCH, 2008. ISBN: 978-3-527-40601-2 (cit. on p. 1).
- [6] C. Yang and R. Mills. *Conservation of Isotopic Spin and Isotopic Gauge Invariance.* Phys. Rev. 96 (1 1954), pp. 191–195 (cit. on pp. 1, 10).
- [7] A. Milsted and T. J. Osborne. *Quantum Yang-Mills theory: An overview of a program.* Phys. Rev. D 98 (1 2018), p. 014505 (cit. on pp. 1, 10).

- [8] S. L. Glashow. *Partial-symmetries of weak interactions*. Nuclear Physics 22.4 (1961), pp. 579–588. ISSN: 0029-5582 (cit. on p. 1).
- [9] D. J. Gross and F. Wilczek. *Ultraviolet Behavior of Non-Abelian Gauge Theories*. Phys. Rev. Lett. 30 (26 1973), pp. 1343–1346 (cit. on p. 1).
- [10] H. D. Politzer. *Reliable Perturbative Results for Strong Interactions?* Phys. Rev. Lett. 30 (26 1973), pp. 1346–1349 (cit. on p. 1).
- [11] P. Higgs. *Broken symmetries and the masses of gauge bosons*. Phys. Rev. Lett. 13 (16 1964), pp. 508–509 (cit. on pp. 1, 14).
- [12] P. Higgs. *Broken symmetries, massless particles and gauge fields*. Physics Letters 12.2 (1964), pp. 132–133. ISSN: 0031-9163 (cit. on pp. 1, 14).
- [13] F. Englert and R. Brout. *Broken Symmetry and the Mass of Gauge Vector Mesons*. Phys. Rev. Lett. 13 (9 1964), pp. 321–323 (cit. on pp. 1, 14).
- [14] S. Weinberg. *The making of the Standard Model*. The European Physical Journal C 34.1 (May 2004), 513. ISSN: 1434-6052. arXiv: hep-ph/0401010 [hep-ph] (cit. on p. 2).
- [15] D. P. Barber et al. *Discovery of Three-Jet Events and a Test of Quantum Chromodynamics at PETRA*. Phys. Rev. Lett. 43 (12 1979), pp. 830–833 (cit. on p. 2).
- [16] G. Arnison et al. *Experimental Observation of Isolated Large Transverse Energy Electrons with Associated Missing Energy at  $\sqrt{s} = 540 \text{ GeV}$* . Phys. Lett. B 122 (1983), pp. 103–116 (cit. on p. 2).

- [17] G. Arnison and others. *Experimental Observation of Lepton Pairs of Invariant Mass Around 95 GeV/c<sup>2</sup> at the CERN SPS Collider*. *Phys. Lett. B* **126** (1983), pp. 398–410 (cit. on p. 2).
- [18] CDF Collaboration. *Observation of Top Quark Production in  $\bar{p}p$  Collisions with the Collider Detector at Fermilab*. *Phys. Rev. Lett.* **74** (14 1995), pp. 2626–2631 (cit. on p. 2).
- [19] DØ Collaboration. *Observation of the Top Quark*. *Phys. Rev. Lett.* **74** (14 1995), pp. 2632–2637 (cit. on p. 2).
- [20] ATLAS Collaboration. *Observation of a new particle in the search for the Standard Model Higgs boson with the ATLAS detector at the LHC*. *Phys. Lett. B* **716** (2012), p. 1. arXiv: 1207.7214 [hep-ex] (cit. on pp. 2, 14).
- [21] CMS Collaboration. *Observation of a new boson at a mass of 125 GeV with the CMS experiment at the LHC*. *Phys. Lett. B* **716** (2012), p. 30. arXiv: 1207.7235 [hep-ex] (cit. on pp. 2, 14).
- [22] S. Navas et al. *Review of particle physics*. *Phys. Rev. D* **110**.3 (2024), p. 030001 (cit. on pp. 2, 7, 8).
- [23] Y. Fukuda et al. *Evidence for Oscillation of Atmospheric Neutrinos*. *Phys. Rev. Lett.* **81** (8 1998), pp. 1562–1567 (cit. on p. 2).
- [24] M. Cristinziani and M. Mulders. *Top-quark physics at the Large Hadron Collider*. *Journal of Physics G: Nuclear and Particle Physics* **44**.6 (2017), p. 063001. arXiv: 1606.00327 [hep-ex] (cit. on pp. 2, 8).

- [25] ATLAS and CMS Collaborations. *Combination of inclusive top-quark pair production cross-section measurements using ATLAS and CMS data at  $\sqrt{s} = 7$  and 8 TeV*. JHEP 07 (2023), p. 213. arXiv: 2205.13830 [hep-ex] (cit. on p. 3).
- [26] C. Degrande, J.-M. Grard, C. Grojean, F. Maltoni, and G. Servant. *Non-resonant new physics in top pair production at hadron colliders*. Journal of High Energy Physics 2011.3 (Mar. 2011). ISSN: 1029-8479. arXiv: 1010.6304 [hep-ph] (cit. on p. 3).
- [27] ATLAS Collaboration. *The ATLAS Experiment at the CERN Large Hadron Collider*. JINST 3 (2008), S08003 (cit. on pp. 3, 22, 25, 26, 28–32).
- [28] ATLAS Collaboration. *Search for topophilic heavy resonances in pp collisions at  $\sqrt{s} = 13$  TeV with the ATLAS detector*. Eur. Phys. J. C 84 (2024), p. 157. arXiv: 2304.01678 [hep-ex] (cit. on pp. 3, 4, 18, 97).
- [29] H. P. Nilles. *Supersymmetry, Supergravity and Particle Physics*. Phys. Rept. 110 (1984), pp. 1–162 (cit. on p. 3).
- [30] G. R. Farrar and P. Fayet. *Phenomenology of the Production, Decay, and Detection of New Hadronic States Associated with Supersymmetry*. Phys. Lett. B 76 (1978), pp. 575–579 (cit. on p. 3).
- [31] T. Plehn and T. M. P. Tait. *Seeking sgluons*. Journal of Physics G: Nuclear and Particle Physics 36.7 (2009), p. 075001. arXiv: 0810.3919 [hep-ph] (cit. on p. 3).
- [32] S. Calvet, B. Fuks, P. Gris, and L. Valry. *Searching for sgluons in multitop events at a center-of-mass energy of 8 TeV*. Journal of High Energy Physics 2013.4 (Apr. 2013). ISSN: 1029-8479. arXiv: 1212.3360 [hep-ph] (cit. on p. 3).

- [33] A. Pomarol and J. Serra. *Top quark compositeness: Feasibility and implications*. *Physical Review D* **78**.7 (Oct. 2008). ISSN: 1550-2368. arXiv: [0806.3247 \[hep-ph\]](#) (cit. on p. 3).
- [34] K. Kumar, T. M. Tait, and R. Vega-Morales. *Manifestations of top compositeness at colliders*. *Journal of High Energy Physics* **2009**.05 (May 2009), 022022. ISSN: 1029-8479. arXiv: [0901.3808 \[hep-ph\]](#) (cit. on p. 3).
- [35] G. Banelli, E. Salvioni, J. Serra, T. Theil, and A. Weiler. *The present and future of four top operators*. *Journal of High Energy Physics* **2021**.2 (Feb. 2021). ISSN: 1029-8479. arXiv: [2010.05915 \[hep-ph\]](#) (cit. on p. 3).
- [36] R. Aoude, H. El Faham, F. Maltoni, and E. Vryonidou. *Complete SMEFT predictions for four top quark production at hadron colliders*. *Journal of High Energy Physics* **2022**.10 (Oct. 2022). ISSN: 1029-8479. arXiv: [2208.04962 \[hep-ph\]](#) (cit. on p. 3).
- [37] C. Zhang. *Constraining qqtt operators from four-top production: a case for enhanced EFT sensitivity*. *Chinese Physics C* **42**.2 (Feb. 2018), p. 023104. ISSN: 1674-1137. arXiv: [1708.05928 \[hep-ph\]](#) (cit. on p. 3).
- [38] L. Darmé, B. Fuks, and F. Maltoni. *Topophilic heavy resonances in four-top final states and their EFT interpretation*. *Journal of High Energy Physics* **2021**.9 (Sept. 2021). ISSN: 1029-8479. arXiv: [2104.09512 \[hep-ph\]](#) (cit. on pp. 3, 17).
- [39] N. Craig, F. D'Eramo, P. Draper, S. Thomas, and H. Zhang. *The Hunt for the Rest of the Higgs Bosons*. *JHEP* **06** (2015), p. 137. arXiv: [1504.04630 \[hep-ph\]](#) (cit. on pp. 3, 17).

- [40] N. Craig, J. Hajer, Y.-Y. Li, T. Liu, and H. Zhang. *Heavy Higgs bosons at low  $\tan \beta$ : from the LHC to 100 TeV*. *Journal of High Energy Physics* 2017.1 (Jan. 2017). ISSN: 1029-8479. arXiv: [1605.08744 \[hep-ph\]](#) (cit. on pp. 3, 17).
- [41] G. C. Branco et al. *Theory and phenomenology of two-Higgs-doublet models*. *Phys. Rept.* 516 (2012), pp. 1–102. arXiv: [1106.0034 \[hep-ph\]](#) (cit. on pp. 3, 17).
- [42] S. Gori, I.-W. Kim, N. R. Shah, and K. M. Zurek. *Closing the wedge: Search strategies for extended Higgs sectors with heavy flavor final states*. *Phys. Rev. D* 93 (7 2016), p. [075038](#) (cit. on pp. 3, 17).
- [43] P. S. B. Dev and A. Pilaftsis. *Maximally symmetric two Higgs doublet model with natural Standard Model alignment*. *Journal of High Energy Physics* 2014.12 (Dec. 2014), p. [024](#). arXiv: [1408.3405 \[hep-ph\]](#) (cit. on pp. 3, 17).
- [44] ATLAS Collaboration. *Observation of four-top-quark production in the multilepton final state with the ATLAS detector*. *Eur. Phys. J. C* 83 (2023), p. [496](#). arXiv: [2303.15061 \[hep-ex\]](#) (cit. on pp. 3, 4, 18, 51, 64, 71, 80).
- [45] N. Greiner, K. Kong, J.-C. Park, S. C. Park, and J.-C. Winter. *Model-independent production of a topophilic resonance at the LHC*. *Journal of High Energy Physics* 2015.4 (2015), p. [29](#). ISSN: 1029-8479. arXiv: [1410.6099 \[hep-ph\]](#) (cit. on pp. 3, 18–20).
- [46] ATLAS Collaboration. *Search for  $t\bar{t}H/A \rightarrow t\bar{t}t\bar{t}$  production in the multilepton final state in proton–proton collisions at  $\sqrt{s} = 13$  TeV with the ATLAS detector*. *JHEP* 07 (2023), p. [203](#). arXiv: [2211.01136 \[hep-ex\]](#) (cit. on p. 4).

- [47] ATLAS Collaboration. *Evidence for  $t\bar{t}t\bar{t}$  production in the multilepton final state in proton–proton collisions at  $\sqrt{s} = 13\text{TeV}$  with the ATLAS detector*. *Eur. Phys. J. C* **80** (2020), p. 1085. arXiv: [2007.14858 \[hep-ex\]](#) (cit. on pp. 4, 71).
- [48] D. H. Perkins. *Introduction to High Energy Physics*. 4th. Cambridge, UK: Cambridge University Press, Apr. 2000. ISBN: 9780521621960 (cit. on p. 5).
- [49] C. Burgard and D. Galbraith. *Standard Model of Physics*. URL: <https://texample.net/model-physics/> (visited on 06/02/2025) (cit. on p. 6).
- [50] H. Georgi. *Lie Algebras in Particle Physics: from Isospin to Unified Theories*. 2nd. CRC Press, 2000. ISBN: 9780429499210 (cit. on pp. 7, 10).
- [51] ATLAS and CMS Collaborations. *Combination of Measurements of the Top Quark Mass from Data Collected by the ATLAS and CMS Experiments at  $\sqrt{s} = 7$  and 8 TeV*. *Phys. Rev. Lett.* **132** (2023), p. 261902. arXiv: [2402.08713 \[hep-ex\]](#) (cit. on p. 8).
- [52] H. de la Torre and T. Farooque. *Looking beyond the Standard Model with Third Generation Quarks at the LHC*. *Symmetry* **14.3** (2022), p. 444 (cit. on p. 8).
- [53] Q.-H. Cao, J.-N. Fu, Y. Liu, X.-H. Wang, and R. Zhang. *Probing Top-philic New Physics via Four-Top-Quark Production*. *Chinese Physics C* **45.9** (2021), p. 093107. arXiv: [2105.03372 \[hep-ph\]](#) (cit. on p. 8).
- [54] H. Beauchesne et al. *A case study about BSM vector resonances with direct couplings to the third quark generation*. *European Physical Journal C* **80.5** (2020), p. 485. arXiv: [1908.11619 \[hep-ph\]](#) (cit. on p. 8).
- [55] F. Maltoni, D. Pagani, and S. Tentori. *Top-quark pair production as a probe of light top-philic scalars and anomalous Higgs interactions*. *Journal of High Energy Physics* **2024.9** (Sept. 2024), p. 098. arXiv: [2406.06694 \[hep-ph\]](#) (cit. on p. 8).

- [56] CMS Collaboration. *Search for  $t\bar{t}H$  production in the  $H \rightarrow b\bar{b}$  decay channel with leptonic  $t\bar{t}$  decays in proton–proton collisions at  $\sqrt{s} = 13$  TeV*. *JHEP* **03** (2019), p. 026. arXiv: 1804.03682 [hep-ex] (cit. on p. 8).
- [57] Y. Grossman and Y. Nir. *The Standard Model: From Fundamental Symmetries to Experimental Tests*. See Chapter 8.2. Cambridge University Press, 2023. ISBN: 9781009320378 (cit. on p. 9).
- [58] M. E. Peskin and D. V. Schroeder. *An Introduction to Quantum Field Theory*. 1st. Reading, MA, USA: AddisonWesley, 1995. ISBN: 978-0-201-50397-5 (cit. on p. 9).
- [59] D. J. Gross. *The role of symmetry in fundamental physics*. *Proceedings of the National Academy of Sciences of the United States of America* **93**.25 (Dec. 1996), pp. 14256–14259 (cit. on p. 9).
- [60] M. Bañados and I. Reyes. *A short review on Noethers theorems, gauge symmetries and boundary terms*. *International Journal of Modern Physics D* **25**.10 (Aug. 2016), p. 1630021. ISSN: 1793-6594. arXiv: 1601.03616 [hep-th] (cit. on p. 9).
- [61] A. Pich. *The Standard Model of electroweak interactions*. *2004 European School of High-Energy Physics*. Feb. 2005, pp. 1–48. arXiv: hep-ph/0502010 [hep-ex] (cit. on pp. 11–13).
- [62] P. Dev and A. Pilaftsis. *High-temperature electroweak symmetry non-restoration from new fermions and implications for baryogenesis*. *Journal of High Energy Physics* **2020**.9 (Sept. 2020), p. 012. arXiv: 2002.05174 [hep-ph] (cit. on p. 13).
- [63] J. Riebesell. *Higgs Potential*. URL: <https://tikz.net/higgs-potential/> (visited on 07/07/2025) (cit. on p. 15).

- [64] J. Goldstone, A. Salam, and S. Weinberg. *Broken Symmetries*. Phys. Rev. 127 (3 1962), pp. 965–970 (cit. on p. 15).
- [65] J. Ellis. *Higgs Physics. 2013 European School of High-Energy Physics*. 2015, pp. 117–168. arXiv: 1312.5672 [hep-ph] (cit. on pp. 15, 16).
- [66] G. Ferretti and D. Karateev. *Fermionic UV completions of composite Higgs models*. Journal of High Energy Physics 2014.3 (Mar. 2014). ISSN: 1029-8479 (cit. on p. 17).
- [67] L. Vecchi. *A dangerous irrelevant UV-completion of the composite Higgs*. JHEP 02 (2017), p. 094. arXiv: 1506.00623 [hep-ph] (cit. on p. 17).
- [68] CDF Collaboration. *Search for New Physics in High-Mass Electron-Positron Events in  $p\bar{p}$  Collisions at  $\sqrt{s} = 1.96$  TeV*. Phys. Rev. Lett. 99 (17 2007), p. 171802. arXiv: 0707.2524 [hep-ex] (cit. on p. 17).
- [69] M. Battaglia and G. Servant. *Four-top production and  $t\bar{t}$ +missing energy events at multi TeV  $e^+e^-$  colliders*. Nuovo Cim. C 033N2 (2010), pp. 203–208. arXiv: 1005.4632 [hep-ex] (cit. on p. 17).
- [70] N. Arkani-Hamed, A. G. Cohen, and H. Georgi. *Electroweak symmetry breaking from dimensional deconstruction*. Physics Letters B 513.1-2 (July 2001), pp. 232–240. arXiv: hep-ph/0105239 [hep-ph] (cit. on p. 17).
- [71] T. Han, H. E. Logan, B. McElrath, and L.-T. Wang. *Phenomenology of the little Higgs model*. Phys. Rev. D 67 (9 2003), p. 095004. arXiv: hep-ph/0301040 [hep-ph] (cit. on p. 17).
- [72] P. Langacker and M. Plümacher. *Flavor changing effects in theories with a heavy  $Z'$  boson with family nonuniversal couplings*. Phys. Rev. D 62 (1 2000), p. 013006. arXiv: hep-ph/0001204 [hep-ph].

- [73] P. Langacker. *The Physics of Heavy  $Z'$  Gauge Bosons*. *Rev. Mod. Phys.* **81** (2009), pp. 1199–1228. arXiv: [0801.1345 \[hep-ph\]](#) (cit. on p. 17).
- [74] J. H. Kim, K. Kong, S. J. Lee, and G. Mohlabeng. *Probing TeV scale top-philic resonances with boosted top-tagging at the high luminosity LHC*. *Phys. Rev. D* **94** (3 2016), p. 035023. arXiv: [1604.07421 \[hep-ph\]](#) (cit. on pp. xi, 17, 18, 20, 86, 96).
- [75] P. J. Fox, I. Low, and Y. Zhang. *Top-philic  $Z'$  forces at the LHC*. *Journal of High Energy Physics* **2018.3** (Mar. 2018). ISSN: 1029-8479. arXiv: [1801.03505 \[hep-ph\]](#) (cit. on p. 17).
- [76] CMS Collaboration. *Observation of four top quark production in proton-proton collisions at  $\sqrt{s} = 13\text{TeV}$* . *Physics Letters B* **847** (2023), p. 138290. arXiv: [2305.13439 \[hep-ex\]](#) (cit. on p. 18).
- [77] G. Brooijmans et al. *New Physics at the LHC. A Les Houches Report: Physics at TeV Colliders 2009 - New Physics Working Group. 6th Les Houches Workshop on Physics at TeV Colliders*. See Chapter 12. May 2010, pp. 191–380. arXiv: [1005.1229 \[hep-ph\]](#) (cit. on p. 20).
- [78] P. Sabatini. *Evidence for four-top-quarks production with the ATLAS detector at the Large Hadron Collider*. Tech. rep. Geneva: CERN, 2021. URL: <https://cds.cern.ch/record/2784150> (cit. on p. 21).
- [79] L. Evans and P. Bryant. *LHC Machine*. *JINST* **3** (2008), S08001 (cit. on p. 22).
- [80] CMS Collaboration. *The CMS Experiment at the CERN LHC*. *JINST* **3** (2008), S08004 (cit. on p. 22).
- [81] The ALICE Collaboration. *The ALICE experiment at the CERN LHC*. *JINST* **3** (2008), S08002 (cit. on p. 22).

- [82] The LHCb Collaboration. *The LHCb Detector at the LHC*. *JINST* **3** (2008), S08005 (cit. on p. 22).
- [83] E. e. a. Gschwendtner. *AWAKE, The Advanced Proton Driven Plasma Wakefield Acceleration Experiment at CERN*. Nuclear Instruments and Methods in Physics Research Section A **829** (2016), pp. 76–82. arXiv: 1512.05498 [physics.acc-ph] (cit. on p. 23).
- [84] J. L. Feng, I. Galon, F. Kling, and S. Trojanowski. *ForwArd Search ExpeRiment at the LHC*. *Phys. Rev. D* **97** (3 2018), p. 035001. arXiv: 1708.09389 [hep-ph] (cit. on p. 23).
- [85] The KATRIN collaboration. *The design, construction, and commissioning of the KATRIN experiment*. *Journal of Instrumentation* **16.08** (2021), T08015. arXiv: 2103.04755 [physics.ins-det] (cit. on p. 23).
- [86] E. Lopienska. *The CERN accelerator complex, layout in 2022*. General Photo. 2022. URL: <https://cds.cern.ch/record/2800984> (visited on 07/08/2025) (cit. on p. 23).
- [87] High Luminosity LHC Project Organization. *The HL-LHC project*. 2025. URL: <https://hilumilhc.web.cern.ch/content/hl-lhc-project> (visited on 06/11/2025) (cit. on p. 24).
- [88] ATLAS Collaboration. *Performance of the ATLAS detector using first collision data*. *JHEP* **09** (2010), p. 056. arXiv: 1005.5254 [hep-ex] (cit. on p. 24).
- [89] ATLAS Collaboration. *Luminosity determination in pp collisions at  $\sqrt{s} = 13 \text{ TeV}$  using the ATLAS detector at the LHC*. *Eur. Phys. J. C* **83** (2023), p. 982. arXiv: 2212.09379 [hep-ex] (cit. on pp. 25, 51, 74).

- [90] J. M. Butterworth, G. Dissertori, and G. P. Salam. *Hard Processes in Proton-Proton Collisions at the Large Hadron Collider*. *Annu. Rev. Nucl. Part. Sci.* **62** (2012), pp. 387–405. arXiv: 1202.0583 [hep-ex] (cit. on p. 25).
- [91] J. Campbell, J. Huston, and W. J. Stirling. *Hard interactions of quarks and gluons: a primer for LHC physics*. *Reports on Progress in Physics* **70**.1 (2006), p. 89. arXiv: hep-ph/0611148 [hep-ex] (cit. on p. 25).
- [92] ATLAS Collaboration. *Standard Model Summary Plots October 2023*. ATL-PHYS-PUB-2023-039. 2023. URL: <https://cds.cern.ch/record/2882448> (cit. on p. 26).
- [93] J. Pequenao and P. Schaffner. *How ATLAS detects particles: diagram of particle paths in the detector*. 2013. URL: <https://cds.cern.ch/record/1505342> (visited on 07/08/2025) (cit. on p. 27).
- [94] J. Pequenao. *Computer generated image of the ATLAS inner detector*. 2008. URL: <https://cds.cern.ch/record/1095926> (visited on 07/08/2025) (cit. on p. 28).
- [95] J. Pequenao. *Computer Generated image of the ATLAS calorimeter*. 2008. URL: <https://cds.cern.ch/record/1095927> (visited on 07/08/2025) (cit. on p. 30).
- [96] ATLAS Collaboration. *Operation of the ATLAS trigger system in Run 2*. *JINST* **15** (2020), P10004. arXiv: 2007.12539 [physics.ins-det] (cit. on p. 33).
- [97] ATLAS Collaboration. *Performance of the ATLAS track reconstruction algorithms in dense environments in LHC Run 2*. *Eur. Phys. J. C* **77** (2017), p. 673. arXiv: 1704.07983 [hep-ex] (cit. on p. 34).
- [98] T. Cornelissen et al. *Concepts, design and implementation of the ATLAS New Tracking (NEWT)*. Tech. rep. Geneva: CERN, 2007. URL: <https://cds.cern.ch/record/1020106> (cit. on p. 34).

- [99] A. Salzburger. *Optimisation of the ATLAS Track Reconstruction Software for Run-2*. Journal of Physics: Conference Series 664.7 (2015), p. 072042 (cit. on p. 34).
- [100] R. Frühwirth. *Application of Kalman filtering to track and vertex fitting*. Nucl. Instrum. Methods Phys. Res. A 262.2 (1987), pp. 444–450. ISSN: 0168-9002 (cit. on p. 34).
- [101] T. Cornelissen et al. *The global  $\chi^2$  track fitter in ATLAS*. Journal of Physics: Conference Series 119.3 (2008), p. 032013 (cit. on p. 34).
- [102] ATLAS Collaboration. *Improved electron reconstruction in ATLAS using the Gaussian Sum Filter-based model for bremsstrahlung*. ATLAS-CONF-2012-047. 2012. URL: <https://cds.cern.ch/record/1449796> (cit. on p. 34).
- [103] D. Wicke. *A new algorithm for solving tracking ambiguities*. Tech. rep. Oct. 1998. URL: <https://cds.cern.ch/record/2625731> (cit. on p. 35).
- [104] ATLAS Collaboration. *Reconstruction of primary vertices at the ATLAS experiment in Run 1 proton–proton collisions at the LHC*. Eur. Phys. J. C 77 (2017), p. 332. arXiv: 1611.10235 [physics.ins-det] (cit. on p. 35).
- [105] W. Waltenberger, R. Frühwirth, and P. Vanlaer. *Adaptive vertex fitting*. Journal of Physics G: Nuclear and Particle Physics 34.12 (2007), N343 (cit. on p. 35).
- [106] ATLAS Collaboration. *Secondary vertex finding for jet flavour identification with the ATLAS detector*. ATL-PHYS-PUB-2017-011. 2017. URL: <https://cds.cern.ch/record/2270366> (cit. on p. 35).
- [107] ATLAS Collaboration. *Performance of pile-up mitigation techniques for jets in pp collisions at  $\sqrt{s} = 8 \text{ TeV}$  using the ATLAS detector*. Eur. Phys. J. C 76 (2016), p. 581. arXiv: 1510.03823 [hep-ex] (cit. on pp. 36, 39).

- [108] ATLAS Collaboration. *Topological cell clustering in the ATLAS calorimeters and its performance in LHC Run 1*. *Eur. Phys. J. C* **77** (2017), p. 490. arXiv: [1603.02934 \[hep-ex\]](#) (cit. on pp. 36, 37).
- [109] ATLAS Collaboration. *Jet reconstruction and performance using particle flow with the ATLAS Detector*. *Eur. Phys. J. C* **77** (2017), p. 466. arXiv: [1703.10485 \[hep-ex\]](#) (cit. on p. 38).
- [110] M. Cacciari, G. P. Salam, and G. Soyez. *The anti- $k_t$  jet clustering algorithm*. *JHEP* **04** (2008), p. 063. arXiv: [0802.1189 \[hep-ph\]](#) (cit. on p. 38).
- [111] ATLAS Collaboration. *Jet energy scale and resolution measured in proton–proton collisions at  $\sqrt{s} = 13\text{ TeV}$  with the ATLAS detector*. *Eur. Phys. J. C* **81** (2021), p. 689. arXiv: [2007.02645 \[hep-ex\]](#) (cit. on pp. 39, 75–77).
- [112] ATLAS Collaboration. *Jet energy scale measurements and their systematic uncertainties in proton–proton collisions at  $\sqrt{s} = 13\text{ TeV}$  with the ATLAS detector*. *Phys. Rev. D* **96** (2017), p. 072002. arXiv: [1703.09665 \[hep-ex\]](#) (cit. on pp. 39, 75).
- [113] ATLAS Collaboration. *Transforming jet flavour tagging at ATLAS*. Tech. rep. Submitted to: Nature Communications. Geneva: CERN, 2025. arXiv: [2505.19689](#) (cit. on pp. 40–42).
- [114] A. Vaswani et al. *Attention Is All You Need*. 2023. arXiv: [1706.03762 \[cs.CL\]](#) (cit. on p. 40).
- [115] ATLAS Collaboration. *Measurements of  $b$ -jet tagging efficiency with the ATLAS detector using  $t\bar{t}$  events at  $\sqrt{s} = 13\text{ TeV}$* . *JHEP* **08** (2018), p. 089. arXiv: [1805.01845 \[hep-ex\]](#) (cit. on pp. 42, 77).

- [116] ATLAS Collaboration. *Electron reconstruction and identification in the ATLAS experiment using the 2015 and 2016 LHC proton–proton collision data at  $\sqrt{s} = 13$  TeV*. Eur. Phys. J. C 79 (2019), p. 639. arXiv: 1902.04655 [physics.ins-det] (cit. on pp. 43–45).
- [117] ATLAS Collaboration. *Muon reconstruction and identification efficiency in ATLAS using the full Run 2 pp collision data set at  $\sqrt{s} = 13$  TeV*. Eur. Phys. J. C 81 (2021), p. 578. arXiv: 2012.00578 [hep-ex] (cit. on pp. 46, 47).
- [118] ATLAS Collaboration. *Muon reconstruction performance of the ATLAS detector in proton–proton collision data at  $\sqrt{s} = 13$  TeV*. Eur. Phys. J. C 76 (2016), p. 292. arXiv: 1603.05598 [hep-ex] (cit. on p. 47).
- [119] ATLAS Collaboration. *Performance of missing transverse momentum reconstruction with the ATLAS detector using proton–proton collisions at  $\sqrt{s} = 13$  TeV*. Eur. Phys. J. C 78 (2018), p. 903. arXiv: 1802.08168 [hep-ex] (cit. on pp. 48, 77).
- [120] ATLAS Collaboration.  *$E_T^{\text{miss}}$  performance in the ATLAS detector using 2015–2016 LHC pp collisions*. ATLAS-CONF-2018-023. 2018. URL: <https://cds.cern.ch/record/2625233> (cit. on p. 49).
- [121] J. Alwall et al. *The automated computation of tree-level and next-to-leading order differential cross sections, and their matching to parton shower simulations*. JHEP 07 (2014), p. 079. arXiv: 1405.0301 [hep-ph] (cit. on pp. 52, 54–57).
- [122] NNPDF Collaboration, R. D. Ball, et al. *Parton distributions for the LHC run II*. JHEP 04 (2015), p. 040. arXiv: 1410.8849 [hep-ph] (cit. on pp. 52, 54–58).
- [123] T. Sjöstrand et al. *An introduction to PYTHIA 8.2*. Comput. Phys. Commun. 191 (2015), p. 159. arXiv: 1410.3012 [hep-ph] (cit. on pp. 52, 54–58).

- [124] ATLAS Collaboration. *ATLAS Pythia 8 tunes to 7 TeV data*. ATL-PHYS-PUB-2014-021. 2014. URL: <https://cds.cern.ch/record/1966419> (cit. on pp. 54–58).
- [125] S. Frixione, E. Laenen, P. Motylinski, and B. R. Webber. *Angular correlations of lepton pairs from vector boson and top quark decays in Monte Carlo simulations*. JHEP 04 (2007), p. 081. arXiv: [hep-ph/0702198](https://arxiv.org/abs/hep-ph/0702198) (cit. on p. 54).
- [126] P. Artoisenet, R. Frederix, O. Mattelaer, and R. Rietkerk. *Automatic spin-entangled decays of heavy resonances in Monte Carlo simulations*. JHEP 03 (2013), p. 015. arXiv: [1212.3460 \[hep-ph\]](https://arxiv.org/abs/1212.3460) (cit. on p. 54).
- [127] D. J. Lange. *The EvtGen particle decay simulation package*. Nucl. Instrum. Meth. A 462 (2001), p. 152 (cit. on p. 54).
- [128] R. Frederix, D. Pagani, and M. Zaro. *Large NLO corrections in  $t\bar{t}W^\pm$  and  $t\bar{t}t\bar{t}$  hadroproduction from supposedly subleading EW contributions*. JHEP 02 (2018), p. 031. arXiv: [1711.02116 \[hep-ph\]](https://arxiv.org/abs/1711.02116) (cit. on pp. 54, 79).
- [129] E. Bothmann et al. *Event generation with Sherpa 2.2*. SciPost Phys. 7.3 (2019), p. 034. arXiv: [1905.09127 \[hep-ph\]](https://arxiv.org/abs/1905.09127) (cit. on pp. 54, 55, 57).
- [130] S. Schumann and F. Krauss. *A parton shower algorithm based on Catani–Seymour dipole factorisation*. JHEP 03 (2008), p. 038. arXiv: [0709.1027 \[hep-ph\]](https://arxiv.org/abs/0709.1027) (cit. on pp. 54, 57, 58).
- [131] S. Höche, F. Krauss, M. Schönherr, and F. Siegert. *A critical appraisal of NLO+PS matching methods*. JHEP 09 (2012), p. 049. arXiv: [1111.1220 \[hep-ph\]](https://arxiv.org/abs/1111.1220) (cit. on pp. 54, 57, 58).

- [132] S. Höche, F. Krauss, M. Schönherr, and F. Siegert. *QCD matrix elements + parton showers. The NLO case.* JHEP 04 (2013), p. 027. arXiv: [1207.5030 \[hep-ph\]](#) (cit. on pp. 54, 57, 58).
- [133] S. Catani, F. Krauss, B. R. Webber, and R. Kuhn. *QCD Matrix Elements + Parton Showers.* JHEP 11 (2001), p. 063. arXiv: [hep-ph/0109231](#) (cit. on pp. 54, 57, 58).
- [134] S. Höche, F. Krauss, S. Schumann, and F. Siegert. *QCD matrix elements and truncated showers.* JHEP 05 (2009), p. 053. arXiv: [0903.1219 \[hep-ph\]](#) (cit. on pp. 54, 57, 58).
- [135] F. Cascioli, P. Maierhöfer, and S. Pozzorini. *Scattering Amplitudes with Open Loops.* Phys. Rev. Lett. 108 (2012), p. 111601. arXiv: [1111.5206 \[hep-ph\]](#) (cit. on pp. 54, 57, 58).
- [136] A. Denner, S. Dittmaier, and L. Hofer. *COLLIER: A fortran-based complex one-loop library in extended regularizations.* Comput. Phys. Commun. 212 (2017), pp. 220–238. arXiv: [1604.06792 \[hep-ph\]](#) (cit. on pp. 54, 57, 58).
- [137] F. Buccioni et al. *OpenLoops 2.* Eur. Phys. J. C 79.10 (2019), p. 866. arXiv: [1907.13071 \[hep-ph\]](#) (cit. on p. 54).
- [138] S. Frixione, G. Ridolfi, and P. Nason. *A positive-weight next-to-leading-order Monte Carlo for heavy flavour hadroproduction.* JHEP 09 (2007), p. 126. arXiv: [0707.3088 \[hep-ph\]](#) (cit. on pp. 55, 56, 58).
- [139] P. Nason. *A new method for combining NLO QCD with shower Monte Carlo algorithms.* JHEP 11 (2004), p. 040. arXiv: [hep-ph/0409146](#) (cit. on pp. 55, 56, 58).
- [140] S. Frixione, P. Nason, and C. Oleari. *Matching NLO QCD computations with parton shower simulations: the POWHEG method.* JHEP 11 (2007), p. 070. arXiv: [0709.2092 \[hep-ph\]](#) (cit. on pp. 55, 56, 58).

- [141] S. Alioli, P. Nason, C. Oleari, and E. Re. *A general framework for implementing NLO calculations in shower Monte Carlo programs: the POWHEG BOX*. *JHEP* 06 (2010), p. 043. arXiv: 1002.2581 [hep-ph] (cit. on pp. 55, 56, 58).
- [142] NNPDF Collaboration, R. D. Ball, et al. *Parton distributions with LHC data*. *Nucl. Phys. B* 867 (2013), p. 244. arXiv: 1207.1303 [hep-ph] (cit. on pp. 55, 56, 58).
- [143] M. Bähr et al. *Herwig++ physics and manual*. *Eur. Phys. J. C* 58 (2008), p. 639. arXiv: 0803.0883 [hep-ph] (cit. on p. 55).
- [144] J. Bellm et al. *Herwig 7.0/Herwig++ 3.0 release note*. *Eur. Phys. J. C* 76.4 (2016), p. 196. arXiv: 1512.01178 [hep-ph] (cit. on p. 55).
- [145] S. Alekhin, J. Blümlein, S. Klein, and S. Moch. *The 3-, 4-, and 5-flavor NNLO parton distribution functions from deep-inelastic-scattering data at hadron colliders*. *Physical Review D* 81.1 (Jan. 2010). ISSN: 1550-2368. arXiv: 0908.2766 [hep-ph] (cit. on pp. 55, 56).
- [146] ATLAS Collaboration. *Studies on top-quark Monte Carlo modelling for Top2016*. ATL-PHYS-PUB-2016-020. 2016. URL: <https://cds.cern.ch/record/2216168> (cit. on p. 56).
- [147] S. Frixione, E. Laenen, P. Motylinski, C. White, and B. R. Webber. *Single-top hadroproduction in association with a W boson*. *JHEP* 07 (2008), p. 029. arXiv: 0805.3067 [hep-ph] (cit. on p. 56).
- [148] T. Gleisberg and S. Höche. *Comix, a new matrix element generator*. *JHEP* 12 (2008), p. 039. arXiv: 0808.3674 [hep-ph] (cit. on p. 57).

- [149] C. Anastasiou, L. Dixon, K. Melnikov, and F. Petriello. *High-precision QCD at hadron colliders: Electroweak gauge boson rapidity distributions at next-to-next-to leading order*. Phys. Rev. D 69 (2004), p. 094008. arXiv: [hep-ph/0312266](#) (cit. on p. 57).
- [150] ATLAS Collaboration. *ATLAS data quality operations and performance for 2015–2018 data-taking*. JINST 15 (2020), P04003. arXiv: [1911.04632 \[physics.ins-det\]](#) (cit. on p. 59).
- [151] ATLAS Collaboration. *Analysis of  $t\bar{t}H$  and  $t\bar{t}W$  production in multilepton final states with the ATLAS detector*. ATLAS-CONF-2019-045. 2019. URL: <https://cds.cern.ch/record/2693930> (cit. on pp. 64, 68, 81).
- [152] ATLAS Collaboration. *Measurement of the total and differential cross-sections of  $t\bar{t}W$  production in  $pp$  collisions at  $\sqrt{s} = 13$  TeV with the ATLAS detector*. JHEP 05 (2024), p. 131. arXiv: [2401.05299 \[hep-ex\]](#) (cit. on p. 64).
- [153] ATLAS Collaboration. *Search for new phenomena in events with same-charge leptons and  $b$ -jets in  $pp$  collisions at  $\sqrt{s} = 13$  TeV with the ATLAS detector*. JHEP 12 (2018), p. 039. arXiv: [1807.11883 \[hep-ex\]](#) (cit. on p. 69).
- [154] ATLAS Collaboration. *Search for  $R$ -parity-violating supersymmetry in a final state containing leptons and many jets with the ATLAS experiment using  $\sqrt{s} = 13$  TeV proton–proton collision data*. Eur. Phys. J. C 81 (2021), p. 1023. arXiv: [2106.09609 \[hep-ex\]](#) (cit. on p. 71).
- [155] E. Gerwick, T. Plehn, S. Schumann, and P. Schichtel. *Scaling Patterns for QCD Jets*. JHEP 10 (2012), p. 162. arXiv: [1208.3676 \[hep-ph\]](#) (cit. on pp. 71, 72).
- [156] G. Avoni et al. *The new LUCID-2 detector for luminosity measurement and monitoring in ATLAS*. JINST 13.07 (2018), P07017 (cit. on p. 74).

- [157] ATLAS Collaboration. *Tagging and suppression of pileup jets*. ATL-PHYS-PUB-2014-001. 2014. URL: <https://cds.cern.ch/record/1643929> (cit. on pp. 75, 77).
- [158] ATLAS Collaboration. *Measurements of inclusive and differential fiducial cross-sections of  $t\bar{t}$  production with additional heavy-flavour jets in proton–proton collisions at  $\sqrt{s} = 13 \text{ TeV}$  with the ATLAS detector*. JHEP 04 (2019), p. 046. arXiv: 1811.12113 [hep-ex] (cit. on p. 79).
- [159] D. de Florian et al. *Handbook of LHC Higgs Cross Sections: 4. Deciphering the Nature of the Higgs Sector*. CERN Yellow Rep. Monogr. 2 (2017), pp. 1–869. arXiv: 1610.07922 [hep-ph] (cit. on p. 79).
- [160] ATLAS Collaboration. *Measurement of the production cross-section of a single top quark in association with a Z boson in proton–proton collisions at 13 TeV with the ATLAS detector*. ATLAS-CONF-2017-052. 2017. URL: <https://cds.cern.ch/record/2273868> (cit. on p. 79).
- [161] F. Demartin, B. Maier, F. Maltoni, K. Mawatari, and M. Zaro. *tWH associated production at the LHC*. EPJC 77.1 (2017). arXiv: 1607.05862 [hep-ph]. URL: <https://doi.org/10.1140/epjc/s10052-017-4601-7> (cit. on p. 79).
- [162] ATLAS Collaboration. *Measurement of  $W^\pm Z$  production cross sections and gauge boson polarisation in  $pp$  collisions at  $\sqrt{s} = 13 \text{ TeV}$  with the ATLAS detector*. Eur. Phys. J. C 79 (2019), p. 535. arXiv: 1902.05759 [hep-ex] (cit. on p. 79).
- [163] G. Cowan, K. Cranmer, E. Gross, and O. Vitells. *Asymptotic formulae for likelihood-based tests of new physics*. The European Physical Journal C 71.2 (Feb. 2011). ISSN: 1434-6052. arXiv: 1007.1727 [physics.data-an]. URL: <http://dx.doi.org/10.1140/epjc/s10052-011-1554-0> (cit. on p. 83).

- [164] J. Neyman and E. S. Pearson. *IX. On the problem of the most efficient tests of statistical hypotheses.* Philosophical Transactions of the Royal Society of London. Series A, Containing Papers of a Mathematical or Physical Character 231.694-706 (1933), pp. 289–337 (cit. on p. 83).
- [165] S. S. Wilks. *The large-sample distribution of the likelihood ratio for testing composite hypotheses.* Annals of Mathematical Statistics 9.1 (1938), pp. 60–62 (cit. on p. 84).
- [166] T. Junk. *Confidence level computation for combining searches with small statistics.* Nuclear Instruments and Methods in Physics Research Section A: Accelerators, Spectrometers, Detectors and Associated Equipment 434.23 (Sept. 1999), 435443. ISSN: 0168-9002. arXiv: [hep-ex/9902006 \[hep-ex\]](#) (cit. on p. 85).
- [167] A. L. Read. *Modified frequentist analysis of search results: The CL<sub>s</sub> method.* Tech. rep. CERN-OPEN-2000-205. Presented at Workshop on Confidence Limits, Geneva, Switzerland. CERN, 2000. URL: <https://cds.cern.ch/record/451614> (cit. on p. 85).
- [168] M. van Beekveld, A. Kulesza, and L. Moreno Valero. *Threshold Resummation for the Production of Four Top Quarks at the LHC.* Phys. Rev. Lett. 131 (21 2023), p. 211901 (cit. on p. 97).
- [169] ATLAS Collaboration. *Preliminary analysis of the luminosity calibration of the ATLAS 13.6 TeV data recorded in 2022.* ATL-DAPR-PUB-2023-001. 2023. URL: <https://cds.cern.ch/record/2853525> (cit. on p. 97).